REPORT DOCUMENTATION PAGE	Form Approved OMB NO. 0704-0188

1. REPORT DATE (DD-MM-YYYY) 21-08-2015	2. REPORT TYPE Ph.D. Dissertation	3. DATES COVERED (From - To) -

4. TITLE AND SUBTITLE a Graph-Based Approach to Nonlinear Model Predictive Control with Application to Combustion Control and Flow Control	5a. CONTRACT NUMBER W911NF-13-1-0122
	5b. GRANT NUMBER
	5c. PROGRAM ELEMENT NUMBER 206022
6. AUTHORS Brandon M. Reese	5d. PROJECT NUMBER
	5e. TASK NUMBER
	5f. WORK UNIT NUMBER
7. PERFORMING ORGANIZATION NAMES AND ADDRESSES Florida A&M University 400 Foote Hillyer Administation Center Tallahassee, FL 32307 -3200	8. PERFORMING ORGANIZATION REPORT NUMBER
9. SPONSORING/MONITORING AGENCY NAME(S) AND ADDRESS (ES) U.S. Army Research Office P.O. Box 12211 Research Triangle Park, NC 27709-2211	10. SPONSOR/MONITOR'S ACRONYM(S) ARO 11. SPONSOR/MONITOR'S REPORT NUMBER(S) 62820-EG-REP.5

12. DISTRIBUTION AVAILIBILITY STATEMENT

Approved for public release; distribution is unlimited.

13. SUPPLEMENTARY NOTES

The views, opinions and/or findings contained in this report are those of the author(s) and should not contrued as an official Department of the Army position, policy or decision, unless so designated by other documentation.

14. ABSTRACT

Systems with a priori unknown, and time-varying dynamic behavior pose a signi?cant challenge in the ?eld of Nonlinear Model Predictive Control (NMPC). When both the identi?cation of the nonlinear system and the optimization of control inputs are done robustly and ef?ciently, NMPC may be applied to control such systems. This dissertation presents a novel method for adaptive NMPC, called Adaptive Sampling Based Model Predictive Control (SBMPC), that combines a radial basis function neural network identi?cation algorithm with a nonlinear

15. SUBJECT TERMS

Adaptive Control, Nonlinear Control, A* Algorithm, Input Sampling, Model Predicitve Control, Combustion Control, Flow Control

16. SECURITY CLASSIFICATION OF:			17. LIMITATION OF ABSTRACT	15. NUMBER OF PAGES	19a. NAME OF RESPONSIBLE PERSON
a. REPORT	b. ABSTRACT	c. THIS PAGE			Emmanuel Collins
UU	UU	UU	UU		19b. TELEPHONE NUMBER 850-410-6367

Standard Form 298 (Rev 8/98)
Prescribed by ANSI Std. Z39.18

Report Title

a Graph-Based Approach to Nonlinear Model Predictive Control with Application to Combustion Control and Flow Control

ABSTRACT

Systems with a priori unknown, and time-varying dynamic behavior pose a signi?cant challenge in the ?eld of Nonlinear Model Predictive Control (NMPC). When both the identi?cation of the nonlinear system and the optimization of control inputs are done robustly and ef?ciently, NMPC may be applied to control such systems. This dissertation presents a novel method for adaptive NMPC, called Adaptive Sampling Based Model Predictive Control (SBMPC), that combines a radial basis function neural network identi?cation algorithm with a nonlinear optimization method based on graph search. Unlike other NMPC methods, it does not rely on linearizing the system or gradient based optimization. Instead, it discretizes the input space to the model via pseudo-random sampling and feeds the sampled inputs through the nonlinear model, producing a searchable graph. An optimal path is found using an ef?cient graph search method. Adaptive SBMPC is used in simulation to identify and control a simple plant with clearly visualized nonlinear dynamics. In these simulations, both ?xed and time-varying dynamic systems are considered. Next, a power plant combustion simulation demonstrates successful control of a more realistic Multiple-Input Multiple-Output system. The simulated results are compared with an adaptive version of Neural GPC, an existing NMPC algorithm based on Netwon-Raphson optimization and a back propagation neural network model. When the cost function exhibits many local minima, Adaptive SBMPC is successful in ?nding a globally optimal solution while Neural GPC converges to a solution that is only locally optimal. Finally, an application to ?ow separation control is presented with experimental wind tunnel results. These results demonstrate real time feasibility, as the control updates are computed at 100 Hz, and highlight the robustness of Adaptive SBMPC to plant changes and the ability to adapt online. The experiments demonstrate separation control for a NACA 0025 airfoil with Reynolds Numbers ranging from 90,000 to 150,000 for both ?xed and pitching (.33 deg/s) angles of attack.

FLORIDA STATE UNIVERSITY

COLLEGE OF ENGINEERING

A GRAPH BASED APPROACH TO NONLINEAR MODEL PREDICTIVE CONTROL WITH APPLICATION TO COMBUSTION CONTROL AND FLOW CONTROL

By

BRANDON M. REESE

A Dissertation submitted to the
Department of Mechanical Engineering
in partial fulfillment of the
requirements for the degree of
Doctor of Philosophy

Degree Awarded:
Spring Semester, 2015

Brandon M. Reese defended this dissertation on April 2, 2015.
The members of the supervisory committee were:

Emmanuel G. Collins
Professor Co-Directing Dissertation

Farrukh S. Alvi
Professor Co-Directing Dissertation

Simon Y. Foo
University Representative

Louis N. Cattafesta
Committee Member

William S. Oates
Committee Member

The Graduate School has verified and approved the above-named committee members, and certifies that the dissertation has been approved in accordance with university requirements.

ACKNOWLEDGMENTS

I would like to acknowledge my family and friends, my CISCOR and FCAAP Colleagues, the McKnight Doctoral Fellowship Program, the GEM Consortium Fellowship, the Army Research Office, the National Science Foundation, and the Army Research Laboratory. Without the support, funding, opportunities, and encouragement offered to me from each of these, I would not have been able to complete this dissertation and degree.

TABLE OF CONTENTS

List of Tables vi

List of Figures vii

List of Symbols xiii

Abstract xv

1 Research Objective **1**

1.1 Motivation 1

1.2 Problem Statement 2

1.3 Dissertation Contributions 3

2 Background and Literature Review **4**

2.1 Nonlinear Model Predictive Control 4

2.2 Predictive Optimization 4

2.3 Neural Network Identification 5

2.4 Power Plant Combustion 7

2.5 Flow Separation 8

2.5.1 Nonlinear POD Methods 8

2.5.2 Recent Advances in Active Flow Control 9

2.5.3 Actuation for Flow Control 10

2.5.4 The Need for an Improved Performance Function 10

3 Adaptive SBMPC **12**

3.1 Methodology 12

3.1.1 The MRAN Identification Network 12

3.1.2 Sampling Based Model Predictive Optimization 16

3.2 Simulation and Results 20

3.2.1 Identification Comparison 22

3.2.2 Control Comparison 23

3.2.3 Run Time Statistics and Real Time Feasibility 24

3.3 Summary 25

4 Application to Combustion Control **28**

4.1 Introduction 28

4.2 Combustion Plant and Neural Network Identification 29

4.2.1 Description of the Plant 29

4.2.2 Neural Network Identification 31

4.2.3 Neural Network Tuning 32

4.3 Control Results 33

4.3.1 Case 1: Time-Invariant SISO Problem 34

4.3.2 Case 2: Introducing a Carbon Penalty Cost 34

4.3.3 Case 3: Control System Adaptation Under Changing Dynamics . . . 40
4.3.4 Run Time Statistics and Real Time Feasibility . . . 44
4.3.5 Tuning the Control Algorithms . . . 45
4.4 Summary . . . 45

5 Application to Flow Separation Control 47
5.1 Introduction . . . 47
5.1.1 Control Objective . . . 48
5.2 Control Method . . . 49
5.2.1 Sampling the Input Domain . . . 50
5.2.2 The Graph Search . . . 50
5.2.3 Nonlinear Modelling . . . 51
5.3 Formulation of Lift Based Performance Function . . . 53
5.3.1 Lift Based Performance Function Validation Results . . . 57
5.4 Experiments and Results . . . 63
5.4.1 Flow Control Experimental Setup . . . 65
5.4.2 Particle Image Velocimetry . . . 66
5.4.3 Open-Loop Characterization . . . 67
5.4.4 Closed-Loop Control . . . 75
5.5 Summary . . . 82

6 Concluding Remarks 86
6.1 Summary of Completed Research . . . 86
6.2 Future Work . . . 87
6.2.1 Learning of Heuristics . . . 87
6.2.2 Parallel Implementation . . . 87
6.2.3 Additional Applications . . . 87
6.2.4 Future Flow Control Research . . . 88

Appendices

A SBMPO Algorithm Pseudocode 90

B SBMPO Soundness and Completeness Proof 92

C Lists of Simulation and Experiment Parameters 94

D List of Tuning Parameter Choices 96

E Lift Based Performance Function Plots 100

Bibliography . . . 106

Biographical Sketch . . . 112

LIST OF TABLES

3.1 Adaptive SBMPC Run Time Statistics: Case 1 24

4.1 Time Variation of Simulation Plant Dynamics 40

4.2 Adaptive SBMPC Run Time Statistics 44

5.1 Chord Locations of Microjet exits and Transducers. 66

C.1 Simulation Parameters: Combustion 94

C.2 Experiment Parameters: Flow Control 95

D.1 MRAN Parameter Choices: Combustion Control 96

D.2 BPN Parameter Choices 97

D.3 SBMPC Parameter Choices: Combustion Control 97

D.4 GPC Parameter Choices: Combustion Control 98

D.5 MRAN Parameter Choices: Flow Control 98

D.6 SBMPC Parameter Choices: Flow Control 99

LIST OF FIGURES

2.1 The layout of a sample RBF network consists of a hidden layer containing one hidden neuron for each distinct state pattern that the algorithm encounters. Collectively these pattern state vectors make up a basis with which all system dynamics are modelled. With enough of these hidden neurons the network is able to match arbitrarily complex nonlinear behavior. 6

3.1 Block Diagram of Adaptive SBMPC. The control task is to provide inputs u to the plant such that outputs y match a reference trajectory r. The neural network model is identified online, and as candidate input trajectories u^* are provided by SBMPO to the neural network, their corresponding predicted outputs $\hat{y}^*$ are returned. 13

3.2 Minimal Resource Allocation Network Flowchart. The MRAN algorithm learns the number of hidden units needed to represent the system and continually refines the parameters of each hidden unit. 14

3.3 Sampling Based Model Predictive Optimization Summary. The algorithm discretizes the input space and makes model-based state predictions, $\hat{x}_{k+j}$, in order to minimize a cost function. 17

3.4 SBMPO Search Graph. The graph is built by expanding the most promising node to generate B child nodes. Each child node is assigned an input sample, which is propagated forward through the model to predict a state for that node. The potential cost of reaching that state is used to prioritize the nodes and select the most promising candidate for the next iteration of expansion. 19

3.5 Benchmarking Plant Visualization. Plot (a) is for $\beta = 1.0$, and plot (b) has $\beta = 0.2$. By modifying β, the number of occurances of local minima in the state space may be greatly increased. In both plots, the prediction horizon $N = 1$. 21

3.6 Training Phase Prediction Errors. Though the BPN algorithm is able to execute each iteration more quickly, completing 25 times more iterations than the RBF learning algorithm, the latter converges much faster and produces lower prediction errors throughout the 30-second learning phase. 22

3.7 Case 1 Results—$\beta = 1.0$ step tracking. After a 30-second training phase, the reference was tracked using GPC (a) and SBMPC (b). Both converge rapidly to the desired set point and achieve steady state estimation and control errors of zero. In the error plot (c), tracking error is the absolute percent difference between desired and actual outputs, while prediction error is the absolute percent difference between predicted and actual outputs. 23

3.8 Case 2 Results—$\beta = 0.2$ step tracking. After a 90-second training phase, the reference was tracked using GPC (a) and SBMPC (b). Both converge more slowly than in the previous case. However Neural GPC convergence takes 100 simulation steps while the Adaptive SBMPC method converges within 20 steps. The GPC suboptimal convergence state is due to finding a local minimum. The error plot (c) indicates a difference of 2.5 orders of magnitude between globally optimal convergence of SBMPC and the locally optimal convergence of GPC. 26

3.9 Case 3 Results—Variable β step tracking. After a 30-second training phase, the reference was tracked using GPC (a) and SBMPC (b). Both converge rapidly to the desired set point and achieve low errors, maintaining good performance as the plant dynamics undergo abrupt changes at time steps 50 and 100. The error plot (c) indicates that Adaptive SBMPC converges more quickly than Neural GPC in response to these changes. 27

4.1 Single Output Neural Network ID comparison. Each neural network is trained with sequential input and output data during the training phase. Prediction error is based only on prediction of x_{O2}. 31

4.2 Multiple Output Neural Network ID comparison. Identification error is computed based on predictions for the three outputs, x_{O2}, x_{CO}, x_{CO2}. For this case, the BPN adaptation converges more slowly, but two identification methods eventually attain comparable prediction error. . . 32

4.3 Case 1 Results—Step Tracking.The reference input was tracked using Neural GPC (a), SBMPC$_{RBF}$ (b), and SBMPC$_{BPN}$ (c). The neural network type affects overshoot due to larger BPN prediction errors. SBMPC convergence, however, is still more rapid than that of GPC regardless of neural network choice. 35

4.4 Neural GPC Case 2 Results. Penalties on CO and CO$_2$ are introduced and plots of inputs dampler angle (a) and fuel rate (b), and outputs oxygen concentration (c) and carbon dioxide concentration (d) are given. The shaded upper and lower regions on the input plots are infeasible regions beyond the input constraints. The value $u_{2,SAT}$ is input to the plant when the fuel rate constraint violation occurs. 37

4.5 SBMPC$_{RBF}$ Case 2 Results. The performance of Adaptive SBMPC is shown. Plots of inputs dampler angle (a) and fuel rate (b), and outputs oxygen concentration (c) and carbon dioxide concentration (d) are given. The shaded upper and lower regions on the input plots are infeasible regions beyond the input constraints. 38

4.6 SBMPC$_{BPN}$ Case 2 Results. The performance of SBMPC using BPN identification is shown. Plots of inputs dampler angle (a) and fuel rate (b), and outputs oxygen concentration (c) and carbon dioxide concentration (d) are given. The shaded upper and lower regions on the input plots are infeasible regions beyond the input constraints. 39

4.7 Neural GPC Case 3 Results. With plant changes occuring every 500 seconds, the model adapts and control inputs are updated simultaneously. Plots of inputs dampler angle (a) and fuel rate (b), and outputs oxygen concentration (c) and carbon dioxide concentration (d) are given. The shaded upper and lower regions on the input plots are infeasible regions beyond the input constraints. The value $u_{2,SAT}$ is input to the plant when the fuel rate constraint violation occurs. 41

4.8 SBMPC$_{RBF}$ Case 3 Results. SBMPC$_{RBF}$ adapts to the plant changes at 500 second intervals. Plots of inputs dampler angle (a) and fuel rate (b), and outputs oxygen concentration (c) and carbon dioxide concentration (d) are given. The shaded upper and lower regions on the input plots are infeasible regions beyond the input constraints. 42

4.9 SBMPC$_{BPN}$ Case 3 Results. SBMPC$_{BPN}$ adapts to the plant changes at 500 second intervals. Plots of inputs dampler angle (a) and fuel rate (b), and outputs oxygen concentration (c) and carbon dioxide concentration (d) are given. The shaded upper and lower regions on the input plots are infeasible regions beyond the input constraints. 43

5.1 Sampling Based Model Predictive Control Summary. The algorithm discretizes the input space and makes model-based state predictions, $\hat{x}_{k+j}$, in order to minimize a cost function. . . 49

5.2 SBMPC Search Graph. The graph is built by expanding the most promising node to generate B child nodes. Each child node is assigned an input sample, which is propagated forward through the model to predict a state for that node. The potential cost of reaching that state is used to prioritize the nodes and select the most promising candidate for the next iteration of expansion. 50

5.3 The layout of a sample RBF network consists of a hidden layer containing one hidden neuron for each distinct state pattern that the algorithm encounters. Collectively these pattern state vectors make up a basis with which all system dynamics are modeled. With enough of these hidden neurons the network is able to match arbitrarily complex nonlinear behavior. 52

5.4 XFOIL Simulation of NACA 0025, 6 degrees, Re = 100,000. 54

5.5 Airfoil Microjet Array and Pressure Transducer Schematic. 55

5.6 Percent errors when angle approximation $\alpha = \alpha_{sep}$ is used. 57

5.7 V_{lift} for lower Reynolds numbers, evaluated from simualated pressures. 58

5.8 V_{lift} for transitional Reynolds numbers, evaluated from simualated pressures. 59

5.9 V_{lift} for higher Reynolds numbers, evaluated from simualated pressures. 60

5.10 Lift Coefficient and L/D for $Re = 90000$ (a) and $Re = 100000$ (b). 61

5.11 Assembled Airfoil CAD with Pressure Transducers 62

5.12 Z_{lift} evaluated with measured pressures compared to measured lift for Re=95,000. 63

5.13 Measured lift and negative p_{rms} evaluated with a single measured pressure signal for Re=95,000. 64

5.14 Airfoil Schematic. This diagram includes the locations of microjet array M1 and M2 and pressure transducers P1 though P4. 65

5.15 Buffer Circuit Diagram . The buffer circuit amplifies an input voltage signal so that the output voltage has sufficient current to drive the solenoid valves. 66

5.16 PIV Experiment Photograph. The PIV setup takes snapshot images of illuminated smoke particles. Processing the images yields velocity field measurements. The laser and optical hardware are configured to illuminate only the smoke particles in the desired plane. 67

5.17 Time Domain Channel Pressures during Pulsed Actuation. The phase-averaged response of the actuator to a 12 Hz square wave is plotted. The width and delay computations are calculated at half of the maximum height of the waveform. 68

5.18 Frequency Domain Channel Pressures during Pulsed Actuation. The response of the actuator to frequency inputs is plotted.This plot displays the response measured at the microjet channel for several different source pressures P_0. 69

5.19 Exit Pressures during Pulsed Actuation. The pressures measured at the microjet exit display a similar trend to those measured within the channel; however, because of the low signal-to-noise ratio, the data for a 10 PSI source pressure is plotted. 70

5.20 Z_{lift} Response to Frequency Actuation at AOA = 19.8°. For various flow conditions, the majority of the lift improvement occurs from 0 to 80 Hz. This is consistent with findings from bandwidth tests, which indicated that 80 Hz was the highest frequency to which the valves are capable of responding. 71

5.21 Z_{lift} response to frequency actuation at AOA = 22.0°. Open loop results at a different angle of attack indicate a clearly nonlinear relationship between input frequency and Z_{lift}. 72

5.22 Measured c_p Values at Pressure Transducer Locations. The pressure transducers are positioned to resolve the suction peak, which grows in each case due to frequency actuation. Larger suction peaks generally correspond to increased overall lift. 74

5.23 Closed Loop Case 1. The Reynolds number is 125,000, and the angle of attack is 20°. This closed loop case illustrates ability to follow a step reference signal subsequent to the activation of the SBMPC controller. 77

5.24 Closed Loop Case 2. The Reynolds number is 125,000, and the angle of attack is 20°. This closed loop case illustrates the ability to command intermediate vales of Z_{lift}. 78

5.25 Closed Loop Case 3. The Reynolds number is 125,000, and the angle of attack is 20°. This closed loop case illustrates the saturation behavior of the controller: from time 0 to 5 seconds, Z_{lift} is simply maximized when the specified reference is above the attainable actuation range. Tracking resumes when the reference value is decreased to an attainable value. 79

5.26 Closed Loop Case 4. The Reynolds number is 150,000, and the angle of attack is 20°. This closed loop case illustrates the ability to track ramp trajectories. During training, the tunnel Reynolds number was set to 125,000, ensuring that online model adaptation would be required when tested at a higher Reynolds number. 80

5.27 Closed Loop Case 5. The Reynolds number shifts from 150,000 to 140,000, and the angle of attack is 20°. This case demonstrates that the ability to adapt enables the control system to be robust to changes in the flow conditions. 81

5.28 Baseline (a) and Controlled (b) V_x for 16°, 15 m/s. The baseline PIV data was collected with the control system off. In the controlled case, data was collected with the control system set to maximize Z_{lift}, and the tunnel speed corresponds to a Reynolds number of 150,000 based on chord length. 82

5.29 Baseline (a) and Controlled (b) V_x for 16°, 12 m/s. The baseline PIV data was collected with the control system off. In the controlled case, data was collected with the control system set to maximize Z_{lift}, and the tunnel speed corresponds to a Reynolds number of 125,000 based on chord length. 83

5.30 Baseline (a) and Controlled (b) V_x for 16°, 15 m/s. The baseline PIV data was collected with the control system off. In the controlled case, data was collected with the control system set to maximize Z_{lift}, and the tunnel speed corresponds to a Reynolds number of 90,000 based on chord length. 83

5.31 Baseline (a) and Controlled (b) V_x for 22°, 11 m/s. The baseline PIV data was collected with the control system off. In the controlled case, data was collected with the control system set to maximize Z_{lift}, and the tunnel speed corresponds to a Reynolds number of 90,000 based on chord length. 84

5.32 Baseline (a) and Controlled (b) V_x for 22°, 12 m/s. The baseline PIV data was collected with the control system off. In the controlled case, data was collected with the control system set to maximize Z_{lift}, and the tunnel speed corresponds to a Reynolds number of 125,000 based on chord length. 84

5.33 Baseline (a) and Controlled (b) V_x for 22°, 15 m/s. The baseline PIV data was collected with the control system off. In the controlled case, data was collected with the control system set to maximize Z_{lift}, and the tunnel speed corresponds to a Reynolds number of 150,000 based on chord length. 85

E.1 Lift Coefficient and L/D for $Re = 50000$. 100

E.2 Lift Coefficient and L/D for $Re = 60000$. 101

E.3 Lift Coefficient and L/D for $Re = 70000$. 101

E.4 Lift Coefficient and L/D for $Re = 80000$. 102

E.5 Lift Coefficient and L/D for $Re = 90000$. 102

E.6 Lift Coefficient and L/D for $Re = 100000$. 103

E.7 Lift Coefficient and L/D for $Re = 110000$. 103

E.8 Lift Coefficient and L/D for $Re = 120000$. 104

E.9 Lift Coefficient and L/D for $Re = 130000$. 104

E.10 Lift Coefficient and L/D for $Re = 140000$. 105

E.11 Lift Coefficient and L/D for $Re = 150000$. 105

LIST OF SYMBOLS

The following list contains symbols used throughout the document.

x	Vector of states
y	Vector of sensor outputs
$\hat{y}$	Vector of Predicted outputs
u	Vector of actuator inputs
T	Control period
RBF	Radial Basis Function
BPN	Back Propagation Network
ϕ_j	j^{th} hidden unit activation function
μ_j	j^{th} hidden unit centroid vector
σ_j	j^{th} hidden unit width
a_j	j^{th} hidden unit output layer weight vector
e_1	Instantaneous prediction error
e_2	RMS prediction error
e_3	Euclidean distance from nearest centroid
M	RMS window size
E_1	Instantaneous prediction error threshold
E_2	RMS prediction error threshold
E_3	Euclidean distance from nearest centroid threshold
$\delta_{p,k}$	k^{th} pruning threshold
$M_{p,k}$	k^{th} pruning window
N_H	Number of hidden units
L	BPN Network Gain
B	Branchout factor
N	Prediction horizon
N_c	Control Horizon
α	Learning rate
η	Momentum coefficient
ε	Solver tolerance
s	Constraint sharpness
λ	Damping factor

x_{O_2}	Oxygen concentration
x_{CO_2}	Carbon dioxide concentration
x_{CO}	Carbon monoxide concentration
ϕ	Air flow damper angle
Φ	Air inlet flow [kg/s]
Φ_f	Fuel inlet flow [kg/s]
c	Chord length [inches]
b	Span length [inches]
RE	Chord based Reynolds number
AOA	Angle of attack
C_L	Lift coefficient
C_D	Drag coefficient
Z_{lift}	Lift Performance Function
V_∞	Free stream velocity

ABSTRACT

Systems with *a priori* unknown, and time-varying dynamic behavior pose a significant challenge in the field of Nonlinear Model Predictive Control (NMPC). When both the identification of the nonlinear system and the optimization of control inputs are done robustly and efficiently, NMPC may be applied to control such systems. This dissertation presents a novel method for adaptive NMPC, called *Adaptive Sampling Based Model Predictive Control (SBMPC)*, that combines a radial basis function neural network identification algorithm with a nonlinear optimization method based on graph search. Unlike other NMPC methods, it does not rely on linearizing the system or gradient based optimization. Instead, it discretizes the input space to the model via pseudo-random sampling and feeds the sampled inputs through the nonlinear model, producing a searchable graph. An optimal path is found using an efficient graph search method. Adaptive SBMPC is used in simulation to identify and control a simple plant with clearly visualized nonlinear dynamics. In these simulations, both fixed and time-varying dynamic systems are considered. Next, a power plant combustion simulation demonstrates successful control of a more realistic Multiple-Input Multiple-Output system. The simulated results are compared with an adaptive version of Neural GPC, an existing NMPC algorithm based on Netwon-Raphson optimization and a back propagation neural network model. When the cost function exhibits many local minima, Adaptive SBMPC is successful in finding a globally optimal solution while Neural GPC converges to a solution that is only locally optimal. Finally, an application to flow separation control is presented with experimental wind tunnel results. These results demonstrate real time feasibility, as the control updates are computed at 100 Hz, and highlight the robustness of Adaptive SBMPC to plant changes and the ability to adapt online. The experiments demonstrate separation control for a NACA 0025 airfoil with Reynolds Numbers ranging from 90,000 to 150,000 for both fixed and pitching (.33 deg/s) angles of attack.

CHAPTER 1

RESEARCH OBJECTIVE

1.1 Motivation

Model Predictive Control (MPC) has been heavily researched and applied across several industries [60], especially in the process control industry. Few Adaptive MPC techniques have been developed [52], and the develpment of practical adaptive MPC methods that use nonlinear models is considered an open problem. The introduction of an efficient nonlinear adaptive method for MPC would significantly expand the range applications for which MPC is effective.

The understanding of nonlinear systems is key to solving numerous engineering problems. Along the path to understanding these systems and solving relevant problems, identification and control methods that capture and harness nonlinear behavior are necessary. To address problems of this sort, the proposed method, *Adaptive Sampling Based Model Predictive Control* (*Adaptive SBMPC*), was developed. The development of this nonlinear MPC method has culminated in the research focus of this dissertation. The unique optimization algorithm, Sampling Based Model Predictive Optimization (SBMPO), has been applied in conjunction with an adaptive, neural-network-based model in order to perform adaptive nonlinear MPC in a more practical and effective manner than existing methods.

A first implementation of Adaptive SBMPC solved a simple single-input, single-output (SISO) nonlinear example from the literature. This example served to demonstrate several properties of the approach, namely the ability to avoid convergence to a local minimum and handle a time-varying plant. A theoretical proof for the completeness of the proposed method is given. The results for this simplified example help us understand the identification and control algorithms' behavior while practical results contribute to real world problem solving. Two problems of considerable practical significance are addressed in this dissertation: the first is a power plant combustion control problem investigated by simulation, and the second is a problem of boundary layer separation control investigated by wind tunnel experiments.

The power plant combustion problem was the first application of Adaptive SBMPC and involves the immediately relevant competing objectives of efficient power generation and environmental sustainability. Constraints on inputs and outputs are critical in this industry and MPC techniques are often selected for their ability to satisfy these types of constraints. This simulation illustrates the capability to control a time-varying nonlinear plant and demonstrates the robustness added by using model adaptation. Furthermore, results will show the avoidance of locally optimal but globally suboptimal solutions. For comparison, an existing method, Neural GPC, is implemented and is shown to converge to a local minimum. Multiple-Input Multiple-Output (MIMO) results are obtained for the combustion control simulation.

The second practical application, control of flow separation, is investigated experimentally using hardware and real time feedback. As boundary layers along aerodynamic surfaces separate in active flight, the phenomenon of flow separation hampers the performance of rotary and fixed wing aircraft. Wings, tails, rotor blades, turbomachinery blades, and the fuselage itself are subject to stall, introducing losses and undesirable unsteadiness. While passive techniques achieve limited mitigation of separation effects in some applications, there is a growing need for active control methods that are able to handle diverse and changing flow conditions. Flows with Reynolds numbers on the order of 100,000 are transitional and are more susceptible to separation than flows in either laminar or turbulent regimes. Systems that employ existing passive or active control techniques are able to produce some delay or mitigation of separation effects, but a new adaptive approach is necessary to maximize performance and recover system losses under the realistic variation in operating conditions experienced in flight.

1.2 Problem Statement

The primary objective of this research is to develop, implement, and demonstrate a new Nonlinear Model Predictive Control (NMPC) method. The development of this method includes the specification of the algorithm and some theoretical analysis of the behavior and performance of the algorithm, the implementation includes the programming of this method for simulation and experimental use. Finally, the demonstration consists of results of the application of this algorithm in simulation and in experiments. Performance and computational cost comparisons to the best existing Adaptive NMPC method, Neural GPC, are provided. The procedures as well as the tuning values used to accomplish these tasks are recorded so that the results obtained here may be reproduced.

This dissertation develops a control system for general application to systems that could include nonlinearity and time dependent behavior. The following are included in the scope of this dissertation. The necessary software design includes simulation implementations, online nonlinear system identification algorithm implementations, and closed-loop control algorithm implementatinos. Experiments with wind tunnel hardware in the loop require the design and construction of an experimental platform for flow separation control. Next, analysis of the simulated test results allow for comparison with stated objectives and previously published adaptive model predictive control methods. Finally, the experimental results must be analyzed to determine the effectiveness of the presented method when applied to a real flow separation control problem.

1.3 Dissertation Contributions

The research in this dissertation makes unique contributions in the areas of MPC and flow control by being the first to publish the achievements listed below.

1. Apply the SBMPO graph search and RBF neural network identification methods to perform receding horizon NMPC.
    (a) First to perform adaptive NMPC using a neural network model that can change its structure as well as its parameter values.
    (b) First to present NMPC results for a time-varying plant.
    (c) Theoretically demonstrate the soundness and completeness of SBMPO.
2. Experimentally demonstrate flow separation control with robustness to changing flow conditions.
    (a) First to implement NMPC method for real time flow control.
    (b) Demonstrate robustness to Reynolds number and angle of attack changes.

CHAPTER 2

BACKGROUND AND LITERATURE REVIEW

2.1 Nonlinear Model Predictive Control

Model Predictive Control (MPC) is widely used in a growing number of industries [59]. Although most MPC implementations use linear models, nonlinear models allow for better performance over a wider operating range [6][24][75][31]. Nonlinear MPC (NMPC) methods require a nonlinear model for predicting system behavior, which can be obtained by first principles or from input and output data using system identification. Advantages of MPC and NMPC methods include satisfaction of input and output constraints and good performance for systems with time delays. The computational cost associated with the numerical solution techniques of many NMPC approaches hinders their application in most practical control problems except those with slow dynamic behavior. Adaptive implementations of NMPC provide the additional benefit of enabling the model to be updated as plant dynamics change. Several NMPC techniques have been developed by extending existing linear MPC techniques to handle plants with strong nonlinearities [59][67][5].

2.2 Predictive Optimization

The optimization for most current NMPC implementations use either sequential quadratic programming or interior point algorithms [52][7]; some other approaches include explicit approximate nonlinear programming [26] and neural network predictive optimization [43]. Drawbacks of sequential quadratic programming methods such as Neural GPC include the computational expense of computing first and second derivatives, possible convergence to local minima that are globally suboptimal, and a lack of robustness due to overly fine tuning requirements. The explicit approximate methods achieve rapid online computation times because the nonlinear programming is solved offline before execution begins, and the online control consists of linear model identification and Linear Quadratic Regulator (LQR) control of perturbations from the approximate nonlinear control law. This method lacks robustness and the ability to perform optimally for a time varying nonlinear system. Approaches that use neural networks for control are better equipped to adapt to changes in the nonlinear plant behavior, however they are computationally inefficient.

The most notable neural network control method, Adaptive Predictive Control employs the Levenberg-Marquardt algorithm to learn its neural network parameters. This variant of nonlinear least squares is reported to be computationally expensive and a barrier to online implementation [43]. NMPC, although theoretically suitible for particular applications such as flow control, has been considered impractical because of the computational cost associated with traditional techniques. For this reason, none of the NMPC methods mentioned above in this section have been successfully implemented in a real time flow control experiments. In his book *Reduced Order Modelling for Flow Control*, Noack writes that "even without contraints, a huge numerical burden will be involved in nonlinear MPC. Today, this is still a limiting factor for flow control applications" [54]. The proposed approach to adaptive NMPC, Adaptive Sampling Based Model Predictive Control (Adaptive SBMPC), first presented in [64], uses the optimization technique known a Sampling Based Model Predictive Optimization. This approach is unique from other methods used for NMPC because the optimization is done by performing a graph search on a sampled input space. This method is explored in this dissertation with an emphasis on achieving the computational efficiency to solve problems in real time.

2.3 Neural Network Identification

The use of an artificial neural network allows nonlinear models to be identified in a general manner by composing a function that computes future outputs based on past states. For this application the state vector,

$$\mathbf{x_k} = (\mathbf{y}_{k-1}^T, \mathbf{y}_{k-2}^T, ..., \mathbf{y}_{k-n_y}^T, \mathbf{u}_{k-1}^T, \mathbf{u}_{k-2}^T, ..., \mathbf{u}_{k-n_u}^T)^T, \tag{2.1}$$

consists of n_u prior plant inputs and n_y outputs. The form,

$$\mathbf{y_k} = f(\mathbf{y}_{k-1}, \mathbf{y}_{k-2}, ..., \mathbf{y}_{k-n_y}, \mathbf{u}_{k-1}, \mathbf{u}_{k-2}, ..., \mathbf{u}_{k-n_u}) \equiv F(\mathbf{x_k}), \tag{2.2}$$

is known as as a nonlinear autoregressive exogenous inputs (NARX) model form because it is analogous to the autoregressive exogenous inputs (ARX) form for linear models. If $F(\mathbf{x_k})$ were a linear function, the equation would simplify to an ARX formulation,

$$\hat{\mathbf{y}}_k = A\mathbf{x}_k, \tag{2.3}$$

with the matrix A of constant coefficients.

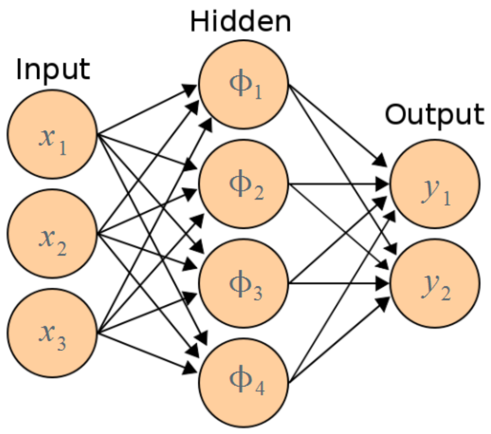

Figure 2.1: The layout of a sample RBF network consists of a hidden layer containing one hidden neuron for each distinct state pattern that the algorithm encounters. Collectively these pattern state vectors make up a basis with which all system dynamics are modelled. With enough of these hidden neurons the network is able to match arbitrarily complex nonlinear behavior.

While there are many ways to construct the nonlinear function $F(\mathbf{x_k})$, neural network methods construct this function as a composition of simpler functions called neural units, which can be arranged in series and parallel to form a network.

A widely used neural network technique is the Back Propagation Network (BPN) [30]. This method requires *a priori* specification of the network size and number of layers and performs parameter updates using an iterative update rule called back propagation. Since its introduction, many BPN variants have been proposed, such as recurrent versions of BPN [57] and the addition particle swarm optimization to the back propagation approach [74]. A disadvantage of BPN-type methods is their fixed structure. Each of the algorithms listed below are initialized with no neural units and are able to adapt their structure by learning the suitable number of units to represent the behavior of the system.

The General Regression Neural Network (GRNN) [69] and the Resource Allocation Network (RAN) [58] both use Radial Basis Function (RBF) neural network structures, depicted in Fig. 2.1, typically having Gaussian activation functions. Major differences between the two include the EKF parameter optimization used by RAN, which contrasts to the simpler update rule utilized for GRNN, and the larger parameter space of RAN. The RAN algorithm fits a separate width to each Gaussian unit while GRNN assumes a common width for each of its Gaussian units.

The network implemented in this research comes from an extension [73] of the RAN method by Platt. This Minimal Resource Allocation Network (MRAN), like RAN, has for its first layer a collection of neural units that respond in parallel when the state $\mathbf{x}_k$ is nearby (according to the *Euclidean norm*) to a previously seen pattern. This method adds to RAN a pruning strategy, which ensures that the model retains only the hidden neurons which have recently contributed significantly to the model output.

2.4 Power Plant Combustion

Energy policy and the rising cost of fossil fuels has highlighted the need for efficient and reliable methods to control the combustion processes of power plants. Legislation that taxes or sets limits on carbon emissions is becoming more common [46][61][3], which has increased demand for control systems that reliably meet constraints on emissions outputs.

When controlling a combustion system, constraints on inputs and outputs are necessary in order to meet power demands, ensure safe operating levels, or regulate environmental pollutants. For these reasons, the industry's need for handling these constraints has steadily increased, and Model Predictive Control (MPC) is arguably the control methodology most suitable to handle them [51]. MPC uses an internal model that represents the system to be controlled, and produces a future sequence of control inputs and the corresponding output trajectory that optimizes a cost function, subject to constraints on functions of the inputs and outputs. Receding horizon MPC approaches use this model to predict several steps in the future while implementing only the immediate next step.

MPC is commonly applied in simulations to power plants [9][47][38][23], and, for applications where no closed-form model is available, is typically applied in conjunction with an identified system model. Linear MPC techniques often use a Least-Squares, Gradient Descent, or Newton method to fit a linear model to observed data [59]. Nonlinear MPC techniques, which are far less commonly used, often fit a Neural Network, Neuro-Fuzzy, Nonlinear Polynomial, or other Nonlinear State Space model to predict system behavior [60].

Due to environmental effects, normal wear, and fatigue, power plant combustion chambers can exhibit time-dependent dynamic behavior. The neural network model form is suitable for modeling the nonlinearities and time variation, which lead to suboptimal performance when they are ignored. The Neural Generalized Predictive Control (Neural GPC) method [67][27] consists of a Back Propagation Neural Network (BPN) and Newton-Raphson cost optimization. It is best able to handle problems with nonlinearities and time variation among existing NMPC methods because it balances speed of optimization with adaptive capability.

An analytical model for coal combustion has been derived [8]. This model has been used in a Single-Input Single-Output (SISO) simulation of Gaussian Process NMPC [25], which requires *a priori* specification of the plant's dynamic equations and achieves rapid online computational speed, at the expense of significant offline computation and a lack of robustness to plant changes. This research in this dissertation solves the problem that was investigated in [25] using an adaptive algorithm that does not require prior knowledge other than the order of plant dynamics. Furthermore, the control problem is extended to include multiple inputs and outputs and time-varying plant dynamics.

2.5 Flow Separation

For decades, flow separation has been of particular interest in engineering applications where improved aerodynamic performance is desired. Control of flow separation, both active and passive, is a key component of existing aviation technology. Passive control methods, such as leading edge surface roughness or the inclusion of vortex generators, rely on a stationary structural component to produce a reduction or delay in separation effects. These techniques typically produce an early transition to turbulence or streamwise vortical structures, each of which have been shown to mitigate separation [40]. The effectiveness of passive techniques is limited in comparison with active techniques, which rely on powered mechanisms to alter the flow, especially when conditions off the design point are considered [10]. These types of off-design conditions are common for aircraft that perform maneuvers, micro-aerial vehicles, and aeronautical systems that are deployed in diverse environments.

Previous adaptive flow separation research has aimed to capture the nonlinear dynamics of the flowfield by identifying an instantaneously linearized model that varies with time. The optimization of a linear model has the advantages of speed and simplicity over those that consider nonlinear models. The unmodelled dynamics, however, can cause such techniques to be suboptimal and even unstable.

2.5.1 Nonlinear POD Methods

Proper Orthogonal Decomposition (POD) techniques have been used to identify models in the form of polynomial difference equations [65][36] that are sufficient for open loop control design [50]. However, due to computational expense, closed loop flow control implementations have been limited to linear models. The primary advantage of SBMPO over alternative methods is that the optimization phase does not prefer linear to nonlinear models, and the algorithm does not need to compute closed-form gradients. Although SBMPO has the ability to optimize inputs to a POD model, POD models are steady state in nature and do not capture the transient behavior or hysteresis effects that are necessary to control aerodynamic flows at relevant time scales.

2.5.2 Recent Advances in Active Flow Control

The significant increase in capability and decrease in cost of computing hardware has led to the feasibility of active control techniques of increasing sophistication. Both open-loop and closed-loop control schemes have been applied to flow control problems and there is evidence that closed loop approaches offer significant improvement in performance over open-loop control [55][34].

The linear method Generalized Predictive Control (GPC) [13] as well as ARMARKOV adaptive control [72] have been effective when applied to the problem of separation flow control [71]. GPC is, in fact, an implementation of receding horizon model predictive control (MPC) that uses closed-form expressions to compute the input sequence. Although many passive and open loop control approaches to the problem of flow separation have been examined, relatively few closed-loop separation control systems have been studied and successfully implemented. This recent work by Tian et al., is the first to incorporate a sophisticated adaptive control approach, implementing ARMARKOV online system identification and the ARMARKOV adaptive disturbance rejection algorithm. Their paper only presents results for stationary and very limited flow parameters: only one Reynolds number and one fixed angle of attack. More recent work presents performance for multiple angles of attack; however, each experimental trial is still conducted at a stationary angle [71]. Since the ARMARKOV and GPC control optimizations rely on closed-form expressions, they are very difficult, if not impossible, to generalize to nonlinear systems unless the dynamics are linearized. Using linearization techniques, GPC has been extended to nonlinear systems using neural network models. These extensions have yet to be applied for flow control although they have been applied in other nonlinear applications both in simulation and experimentally.

Several areas of flow control research, including suppression of cavity flow resonant tones and mitigation of flow separation, have advanced rapidly in recent years as new technologies have both created demand for and expanded the capabilities of such systems. The study of cavity flow control has demonstrated that mathematical techniques such as Proper Orthogonal Decomposition (POD) and model reduction are effective tools for controlling aerodynamic systems [50][20]. While these studies incorporated flow visualization and analysis efforts to produce nonlinear models that are effective for developing open-loop control strategies, it has been more practical to linearize these models for the sake of computational efficiency when implementing real-time closed loop control [55][34].

The problem of flow separation overlaps with the study of cavity flow; frequency domain methods are applied to model and control the flow dynamics in both applications [49][12][42]. POD methods similar to those applied to cavity flow have also been used for flow separation [22]. Actuator development has also been key to the recent advances in the field of flow separation control. Both synthetic jet unsteady actuators [71][70] and steady microjet actuators [12][4] have been effective in separation control experiments. Because of the advantage of high momentum capability with low power requirements [41], microjets have been selected as the primary actuators for this research.

2.5.3 Actuation for Flow Control

While the innovations outlined in this dissertation may be applied to many sensor and actuator hardware configurations, microjet actuators have been selected for this research. Microjet actuators have distinct advantages over alternatives actuation methods for the control of flow separation. This study will use microjets capable of steady actuation; however, the control system will also be able to supply unsteady input signal when a capable actuator is installed. While other micro actuators are able to produce comparable jet velocities, ease of fabrication and in-house expertise make microjet actuators a practical choice. After proving the control system concept with microjets, other actuators may easily be interchanged for comparison.

Piezoelectric synthetic jets, another common flow control actuator, while having the advantage of zero net mass flux, are known to have difficulty generating the mass flow rates and jet speed required for higher speed applications [4]. Newly developed plasma based thermal actuators have difficulties similar to those of synthetic jets and tend to take longer to alter the flow [53]. Non-thermal plasma based actuators are in development but are not as mature and have not achieved the control authority of microjet actuators. At this point, microjets provide the greatest control authority per unit of power consumption, but it is possible that still more efficient actuators may be available in the next few years.

2.5.4 The Need for an Improved Performance Function

Previous flow separation control research has used an RMS pressure value as the performance function for feedback control [71][70][68]. While minimizing p_{rms} at a particular transducer location will sometimes maximize the desired quantity C_L/C_D, Sheplak et al. present results where at different flow conditions, control that maximizes C_L/C_D produces an increase in p_{rms} [66]. This result gives evidence that minimizing

p_{rms} at a single sensor is insufficient for effective control across a wide range of flow conditions. As derived in [62], a performance function that incorporates several pressure transducer signals and correlates with C_L/C_D will make effective closed-loop performance possible over a wider range of angle of attack and Reynolds number conditions. Since combining multiple transducer signals in an intelligent manner collapses multiple variables into one performance variable, this method will also reduce the computational effort needed to perform system identification and control with multiple sensors.

CHAPTER 3

ADAPTIVE SBMPC

3.1 Methodology

The Adaptive SBMPC approach to nonlinear MPC consists of identification of an approximate system model during the learning phase followed by simultaneous identification and control during the control phase. As shown in Fig. 3.1, a neural network is used to model the plant dynamics and SBMPC is used to generate actuation signals to control the plant. A summary of the MRAN identification algorithm and the details of the SBMPC methodology is described below, a full description of the MRAN algorithm may be found in [2].

3.1.1 The MRAN Identification Network

The Minimal Resource Allocation Network (MRAN) algorithm implemented in this research was developed by Yingwei et al. [2]. It is based on the Resource Allocation Network algorithm, a general method for function approximation [58]. The advantage over other methods is that the network eventually reaches a constant size despite increasing the length of the training set. Yingwei et al. extended RAN to MRAN by adding a pruning step. The MRAN learning paradigm is sufficiently general to represent many different systems with little or no alteration of the algorithm's tuning parameters.

The RBF Neural Network. Referring to Fig. 3.2, MRAN is a general purpose procedure for function approximation that aims to represent some vector output $f(x)$ as the result of some nonlinear mapping of the input state vector x. When applying MRAN to learn a system's input-output behavior, x is the vector of the past m inputs and n outputs given by

$$x = [y_{i-1}^T, y_{i-2}^T, \ldots, y_{i-n}^T, u_{i-1}^T, u_{i-2}^T, \ldots, u_{i-m}^T]^T, \tag{3.1}$$

and $f(x)$ is the current output prediction given by

$$f(x) = \hat{y} = a_0 + \sum_{j=1}^{N_H} a_j \phi_j(x). \tag{3.2}$$

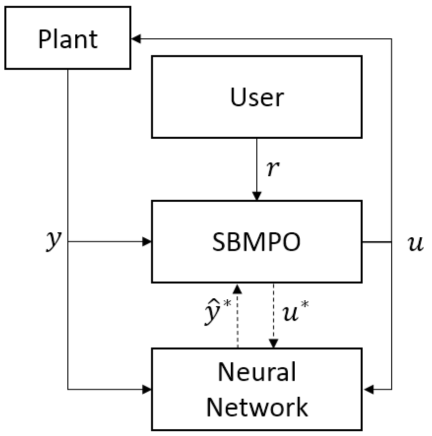

Figure 3.1: Block Diagram of Adaptive SBMPC. The control task is to provide inputs u to the plant such that outputs y match a reference trajectory r. The neural network model is identified online, and as candidate input trajectories u^* are provided by SBMPO to the neural network, their corresponding predicted outputs $\hat{y}^*$ are returned.

When each function ϕ_j is radially symmetric about some unique centroid μ_j, the function defined in (5.10) is known as a Radial Basis Function (RBF). The RBF is a single layer neural network structure as depicted in Figure 2.1. In MRAN, each ϕ_j is a Gaussian function with a unique width σ_j, that is,

$$\phi_j = \exp\left(-\frac{\|x_k - \mu_j\|^2}{\sigma_j^2}\right). \tag{3.3}$$

As seen in (5.10), the RBF network output is a linear combination of several Gaussian functions. Each set of parameters $\{\mu_j, \sigma_j, a_j\}$ constitutes a hidden unit. As the MRAN algorithm runs, the number of hidden units N may grow and shrink, and the parameter values are continually refined to minimize prediction error.

MRAN Methodology. The MRAN algorithm, depicted in Fig. 3.2, begins with an empty network ($N_H = 0$) and uses prediction error criteria at each time step k to determine whether an additional hidden unit is necessary to represent the system. In each algorithm iteration, the network is refined to reduce prediction error either via addition of a hidden unit or an Extended Kalman Filter (EKF) adjustment of the parameter vector of all current hidden units. Hidden units that have low relative contribution over a designated number of time steps M_p are removed from the network in the pruning stage.

The three error criteria are

$$e_1 = \|y_k - \hat{y}_k\|, \tag{3.4}$$

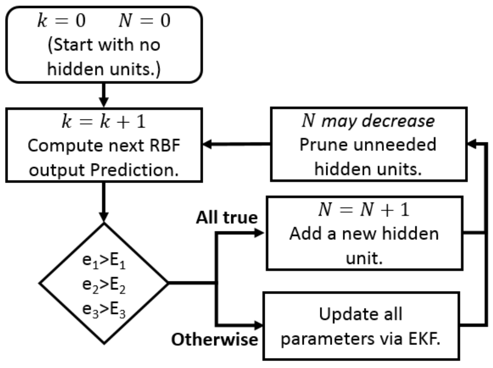
$k = 0 \quad N = 0$
(Start with no hidden units.)
$k = k + 1$
Compute next RBF output Prediction.
N may decrease
Prune unneeded hidden units.
All true
$N = N + 1$
Add a new hidden unit.
e1>E1
e2>E2
e3>E3
Otherwise
Update all parameters via EKF.

Figure 3.2: Minimal Resource Allocation Network Flowchart. The MRAN algorithm learns the number of hidden units needed to represent the system and continually refines the parameters of each hidden unit.

$$e_2 = \sqrt{\sum_{i=k-M+1}^{k} \frac{\|y_i - \hat{y}_i\|^2}{M}}, \tag{3.5}$$

$$e_3 = \|x_k - \mu^*\|. \tag{3.6}$$

Criterion e_1 represents instantaneous error, while e_2 is an RMS error averaged over the RMS window M, and e_3 is the Euclidean distance from the current state to the nearest basis vector, denoted μ^*. A new hidden unit is added only when

$$e_1 > E_1 \qquad \text{and} \quad e_2 > E_2 \qquad \text{and} \quad e_3 > E_3, \tag{3.7}$$

where thresholds E_1, E_2, and E_3 are tuning parameters.

When (3.7) is satisfied, a new hidden unit is introduced with parameter values chosen to cancel out the instantaneous error, yielding

$$a_{N_H+1} = e_k, \qquad \mu_{N_H+1} = x_k, \qquad \sigma_{N_H+1} = \kappa\|x_k - \mu^*\|, \tag{3.8}$$

where the initial Gaussian width σ_{N_H+1} depends on the basis function overlap parameter κ.

If a hidden unit was not introduced during a time step, the vector of model parameters,

$$w = [a_0^T, a_1^T, \mu_1^T, \sigma_1, ..., a_{N_H}^T, \mu_{N_H}^T, \sigma_{N_H}]^T, \tag{3.9}$$

is updated using the following Extended Kalman Filter (EKF) procedure. First, compute a gradient matrix $B_k \triangleq \nabla_w F(x_k)$ for the current time step, which is evaluated as

$$\begin{aligned} B_k = [&I_n, \phi_1 I_n, \phi_1(2a_1/\sigma_1^2)(x_k - \mu_1)^T, \\ &\phi_1(2a_1/\sigma_1^3)\|x_k - \mu_1\|^2, \cdots, \\ &\phi_{N_H} I_n, \phi_{N_H}(2a_{N_H}/\sigma_{N_H}^2)(x_k - \mu_{N_H})^T, \\ &\phi_{N_H}(2a_{N_H}/\sigma_{N_H}^3)\|x_k - \mu_{N_H}\|^2]^T, \end{aligned} \tag{3.10}$$

where I_n is the $n \times n$ identity matrix. To perform the EKF update, define the Kalman gain matrix

$$K_k = P_{k-1} B_k [R_k + B_k^T P_{k-1} B_k]^{-1}, \tag{3.11}$$

with system error covariance and sensor noise covariance matrices P_k and R_k. In the RAN algorithm, $R_k = R$, a constant matrix, specified by sensor properties or offline measurements. At each EKF step, P is updated using

$$P_k = [I_p - K_k B_k^T] P_{k-1} + q I_p, \tag{3.12}$$

where q is a step size parameter and dimension p is the number of elements in w. The parameters are updated to reduce the size of the identification error,

$$w_k = w_{k-1} + K_k e_k. \tag{3.13}$$

When a hidden unit is introduced, the dimensionality of P must increase by the number p_1 of parameters that are added to w, yielding

$$P_k = \begin{pmatrix} P_{k-1} & 0 \\ 0 & \gamma_0 I_{p_1} \end{pmatrix}. \tag{3.14}$$

The parameter γ_0 is an initial estimate of the variance for newly assigned data-based parameter values. This procedure, which results in either the addition of a new hidden unit or the EKF refinement of existing parameters, repeats until terminated.

The above specifies the Resource Allocation Network (RAN) algorithm [58], which combines EKF gradient based optimization with heuristic based pattern recognition and learning to produce identified models that approximate general nonlinear dynamics in an efficient manner. A pruning step is added to the RAN algorithm by Yingwei et al. to produce the MRAN algorithm [2]. This step removes hidden units whose relative contribution to the overall network output falls below a threshold for a number of consecutive time steps.

The Pruning Criterion. The pruning criterion ensures that the network does not retain hidden units that are not needed to describe system behavior. Without a proper pruning condition, the network size would tend to grow indefinitely as adaptations are made to capture new behavior patterns. A hidden unit's output is considered insignificant if the ratio of it's contribution to the summation of (5.10) to the largest term in the summation is smaller than a chosen threshold δ_p. To decide which hidden units to prune, a counter keeps track of the number of consecutive time steps during which each hidden unit has produced an insignificant contribution to the output. Once the number of consecutive time steps for a particular hidden unit exceeds a chosen limit M_p, that hidden unit is removed from the neural network.

Algorithm Extension: Multistage Pruning Criterion. This research extends the MRAN pruning logic by allowing multiple pruning criteria, each represented by a significance threshold $\delta_{p,k}$ and consecutive limit $M_{p,k}$. If any one of these criteria is met by a given hidden unit, the unit is pruned. By allowing for pruning behavior that specifies both fast-acting pruning behavior (with smaller $\delta_{p,k}$) and long-acting pruning behavior (with larger $\delta_{p,k}$), the multistage approach to pruning gives more flexibility to trade off network size and prediction accuracy.

MRAN Computational Complexity. The bottleneck in the computation of the MRAN algorithm is the EKF, which is intractably $\mathscr{O}(N^2)$ in the number of hidden units [29]. For a given real-time constraint, this will limit the maximum network size for which the algorithm may be feasibly executed. If assumptions are made about the hidden unit parameters, they may be organized into mutually exclusive groups, which would require smaller matrix inversions and reduce the complexity. For the problem presented below, the maximum network size is 480, a tuning parameter which allows for the tradeoff of prediction accuracy versus computational cost.

3.1.2 Sampling Based Model Predictive Optimization

As a means of solving model predictive optimization problems without computing gradients, Sampling Based Model Predictive Optimization (SBMPO) has been developed and implemented on experimental platforms [19][18][1]. For a nonnegative cost function $C(\cdot)$, SBMPO may be applied to solve the nonlinear optimization problem,

$$\min_{\{\mathbf{u}(k),\ldots,\mathbf{u}(k+N-1)\}} \sum_{i=0}^{N-1} C\left(\mathbf{y}(k+i+1)-\mathbf{r}(k+i+1)\right), \tag{3.15}$$

subject to the nonlinear state space equations,

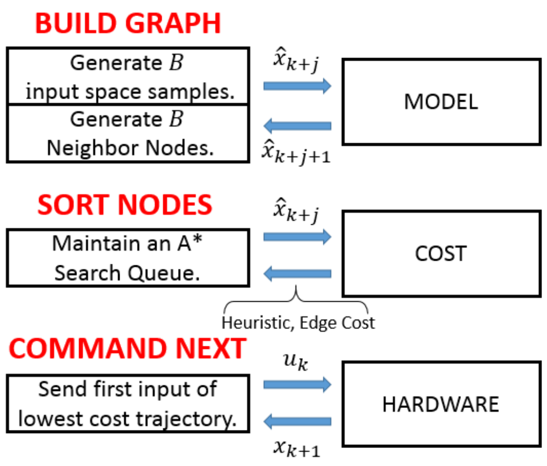
BUILD GRAPH
Generate B input space samples.
Generate B Neighbor Nodes.
$\hat{x}_{k+j}$
$\hat{x}_{k+j+1}$
MODEL
SORT NODES
Maintain an A* Search Queue.
$\hat{x}_{k+j}$
COST
Heuristic, Edge Cost
COMMAND NEXT
Send first input of lowest cost trajectory.
u_k
x_{k+1}
HARDWARE

Figure 3.3: Sampling Based Model Predictive Optimization Summary. The algorithm discretizes the input space and makes model-based state predictions, $\hat{x}_{k+j}$, in order to minimize a cost function.

$$\mathbf{x}(k+i) = g(\mathbf{x}(k+i-1), \mathbf{u}(k+i-1)), \tag{3.16}$$

$$\mathbf{y}(k) = h(\mathbf{x}(k)), \tag{3.17}$$

and the constraints,

$$\mathbf{x}(k+i) \in \mathbf{X}_{free} \; \forall \;\; i \leq N, \tag{3.18}$$

$$\mathbf{u}(k+i) \in \mathbf{U}_{free} \; \forall \;\; i \leq N, \tag{3.19}$$

where $r(k)$ is the reference input and $\mathbf{X}_{free}$ and $\mathbf{U}_{free}$ represent the states and inputs respectively that do not violate any of the problem constraints. SBMPO is described in Fig. 5.1 and is easily applied to both linear and nonlinear models, combining techniques for sampling the input domain with an efficient graph search method such as A*. The details of SBMPO are given in [1]. See Appendix A for a pseudocode listing of the SBMPO algorithm. The implicit grid test for overlapping states [21] is not implemented. This simplification of the algorithm is applied because for the short prediction horizons used, state overlap is improbable. Below, various aspects of SBMPO are emphasized.

Sampling the Input Domain. The field of path planning in robotics has seen recent innovations that have used sampling techniques [39][44]. SBMPO involves the sampling of the space of allowable inputs. Halton sampling, in particular, is a method based on the low-discrepancy Halton sequences that has been shown to provide representative sample sets consisting of fewer points than sets generated using pseudo-random numbers or regular grids [56][11]. Satisfaction of input constraints is automatic, since it is the allowable inputs that are sampled, and since the inputs are propagated forward through the model, no inversion of the model is needed.

The Graph Search. Using the current state and input samples, several nodes are computed by propagating the model and added to a graph with tree connectivity, as illustrated in Fig. 5.2. The branchout factor B, a tuning parameter of the algorithm, determines how many child nodes are generated when a particular parent node is expanded. In the implementation of this algorithm, each node has a pointer to its parent node so that, for every node, there is an implied path from the root node to itself. Therefore, the optimization task is to choose the node at horizon depth that is reachable by the lowest cumulative cost. The computation is done by best-first search using the A^* algorithm [28] or one of its variants such as LPA^* [37].

SBMPO Completeness. For the receding horizon MPC problem, we define a goal state as any horizon-depth node whose trajectory is minimal in cost. A *sound* graph search algorithm returns only trajectory solutions that reach a goal state. A given sound algorithm is *complete* if it always returns one such solution if any solution exists. Assuming the heuristic function always underestimates the lowest cost to the prediction horizon, SBMPO, like A^* and other graph search algorithms, may be shown to be complete over a given graph. A proof loosely based on the procedure in [35] is formally derived in Appendix B. Its culmination, Theorem B.0.6, guarantees that, subject to sufficient depth and breadth of sampling, SBMPO will find a globally optimal solution. Due to gaps between samples, some suboptimality will result. Note that with the nonuniform sampling strategy described in Subsection 3.1.2, the gaps between samples become very small at steady state.

Obstacles and Hard Constraints. Because the input domain samples are selected from the specified region only, hard input constraints are met automatically. An additional advantage of using a graph search approach is the ease of dealing with obstacles and hard output constraints. Naturally, if a node represents a state that is not allowed by the specified constraints or obstacles, it is removed from the queue and the next node in the queue is chosen instead.

Algorithm Contribution: Precomputed Samples. The Halton sequence algorithm, which is potentially used thousands of times at each time interval when the SBMPC routine is called, was a major contributor to the total runtime of SBMPC. Generating new Halton samples takes a median of 210 times longer than

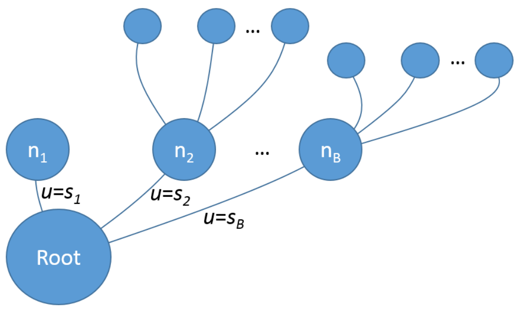

Figure 3.4: SBMPO Search Graph. The graph is built by expanding the most promising node to generate *B* child nodes. Each child node is assigned an input sample, which is propagated forward through the model to predict a state for that node. The potential cost of reaching that state is used to prioritize the nodes and select the most promising candidate for the next iteration of expansion.

a lookup table query; therefore, precomputing these samples and storing them in memory enables the run-time code to execute much faster while yielding identical results. Note that although the uniform samples are generated offline, the transformation to a nonuniform distribution, described in 3.1.2, is not precomputed. In order to maintain integrity near the boundary of the input sampling domain, it is necessary to use a truncated, asymmetric distribution when sampling changes in an input that is near its boundary. Because this calculation is state-dependent, it is carried out in run-time which is a major contributor to the execution time difference between the cases of uniform and nonuniform sampling density.

Algorithm Contribution: Nonuniform Distribution. The uniform sampling density typically used for SBMPC may be transformed in order to achieve greater relative sampling density in a desired region of the input domain. In order to preserve input constraint satisfaction, the range sampled by the uniform distribution should be maintained. The following procedure can be followed to obtain a nonuniform sampling distribution aggregated about zero:

1. Transform the samples linearly to occupy the range $[-1, 1]$
2. Record the sign of each transformed sample
3. Raise each transformed sample to an integer power
4. Restore the sign (if even power) and apply the inverse linear transform to the samples

Using a nonuniform sampling density can improve the performance of SBMPC by reducing the branchout factor required to converge to some near-optimal trajectory. Both the generation of Halton samples and the transformation described here may be computed offline and accessed through a lookup table.

SBMPO Computational Complexity. The execution time required to run SBMPO, the optimization phase of Adaptive SBMPC, is roughly proportional to the number of nodes expanded, which is the case for most graph search algorithms [17]. The SBMPO search tree is generated and explored in a best-first sense. For a maximum graph size of V vertices, SBMPO is an $\mathscr{O}(|V|)$ algorithm since, in the worst case, every node with depth less than the control horizon will be expanded, yielding an upper bound of B^{N-1} expansions. In practice, the number required is far fewer, but the worst case is considered when developing a real-time execution guarantee. While real time algorithms are often programmed to terminate early in the event of a longer-than-feasible execution time, this can often lead to undesired performance. In the implementation of SBMPO, the real-time guarantee is achieved by limiting the nodes that may be generated in a single call of the SBMPO routine. In the event that the optimization phase terminates early, the evaluated nodes of greatest depth are listed and the node among those with lowest cost is chosen.

3.2 Simulation and Results

For comparison, both Adaptive SBMPC and Neural GPC were used to control the benchmark SISO nonlinear plant [73] described by the difference equation

$$\begin{aligned} y(k) = \frac{29\beta(k)}{40} sin\left(\frac{16u(k-1)+8y(k-1)}{\beta(k)(3+4u(k-1)^2+4y(k-1)^2}\right) \\ +\frac{1}{5}u(k-1)+\frac{1}{5}y(k-1), \end{aligned} \tag{3.20}$$

where $\beta(k)$ is a parameter that may be modified to alter the behavior of the plant. The MPC cost function,

$$J = \sum_{i=0}^{N-1} \left(\mathbf{y}(k+i+1)-\mathbf{r}(k+i+1)\right)^2, \tag{3.21}$$

was optimized by each algorithm, equally weighting each future term up to the prediction horizon N. The SISO, first-order nature of the plant allows simple visualization of the state-to-cost behavior, by plotting the states $u(k-1)$ and $y(k-1)$ on the lateral axes and the cost (3.21) on the vertical axis. In order to simplify the visualizations, the cost functions have prediction horizon $N=1$. Two versions of the plant are visualized in Fig. 3.5: (a) $\beta = 1.0$ and (b) $\beta = 0.2$.

The following three plant cases were considered:

1. Fixed plant with $\beta = 1.0, \quad r(k) = 2.2$
2. Fixed plant with $\beta = 0.2, \quad r(k) = 0.4$

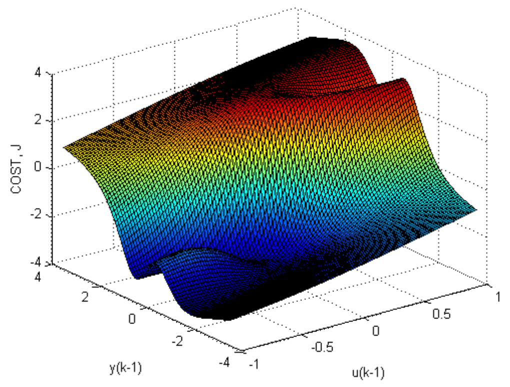

(a)

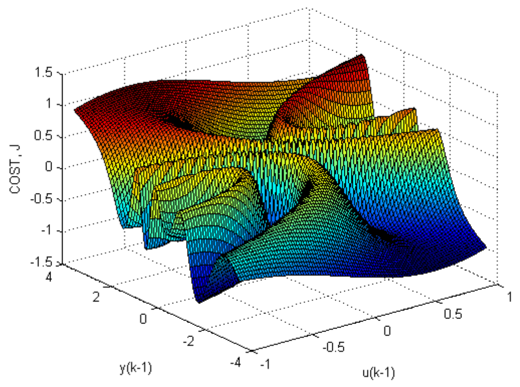

(b)

Figure 3.5: Benchmarking Plant Visualization. Plot (a) is for $\beta = 1.0$, and plot (b) has $\beta = 0.2$. By modifying β, the number of occurances of local minima in the state space may be greatly increased. In both plots, the prediction horizon $N = 1$.

3. Changing plant with $\beta \in [0.8, 1.0]$, $\quad r(k) = 2.2$

The first of these is a straightforward control problem in which the algorithms can usually plan from the initial state to the set point without encountering a local minimum. In the second plant configuration, however, many local minima exist between the initial state and desired set point. The set point r was also reduced to 0.4 for this case because the original set point, 2.2, is not reachable for small β. The third is a control problem with a time-varying plant, where the parameter β varies according to

$$\beta(k) = \begin{cases} 1.0 & \text{for } 0 < k \leq 50 \\ -0.9 & \text{for } 500 < k \leq 100 \\ 0.8 & \text{otherwise} \end{cases}, \tag{3.22}$$

so that both the neural network model and control inputs must be actively modified to maintain optimal set point tracking.

In each simulation trial Adaptive SBMPC or Neural GPC first identifies the nonlinear system during the learning phase and then is given a fixed set point to track as a reference trajectory. During the learning phase, only the neural network identification portion of the algorithm is active, while during the control phase, both identification and control algorithms are in operation.

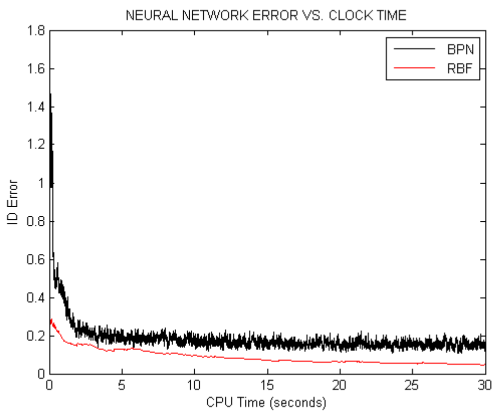

Figure 3.6: Training Phase Prediction Errors. Though the BPN algorithm is able to execute each iteration more quickly, completing 25 times more iterations than the RBF learning algorithm, the latter converges much faster and produces lower prediction errors throughout the 30-second learning phase.

3.2.1 Identification Comparison

The identification methods used in Adaptive SBMPC and Neural GPC differ significantly although both are neural network based. The MRAN algorithm described in Section 3.1.1 is used to construct the RBF network in Adaptive SBMPC, whereas Neural GPC uses a Back Propagation Network (BPN) with a sigmoid activation function, and selects a fixed number of hidden units. The neural network parameters are initialized randomly and modified at each time step using a back propagation rule.

In the learning phase, random white noise over the allowable input range was provided to excite the system. Input and output data was fed to the identification algorithm sequentially, and at each time step, a prediction was made before adjusting the neural network to reduce the error. For a single time step, the BPN method executed up to 25 times faster than MRAN, primarily due to the costly EKF. However, the RBF method trained using MRAN produced predictions with significantly lower errors than the BPN method. In order to make a proper comparison, both algorithms were allowed a thirty-second training phase. The learning phase error results of Fig. 3.6 indicate that throughout the learning phase, the RBF network made predictions with lower error. Even though the BPN method computed many more iterations within the thirty seconds, the convergence rate of back propagation is far slower than that of the EKF of MRAN.

3.2.2 Control Comparison

For the control phase, the algorithms were given a constant set point toward which to drive the system output. Optimization was performed in a receding horizon fashion with a control horizon N_C of 2 and a prediction horizon N of 10.

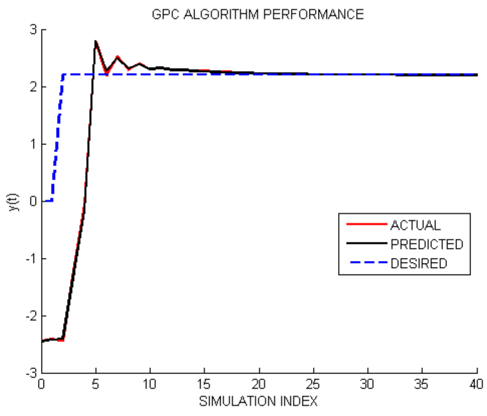

(a)

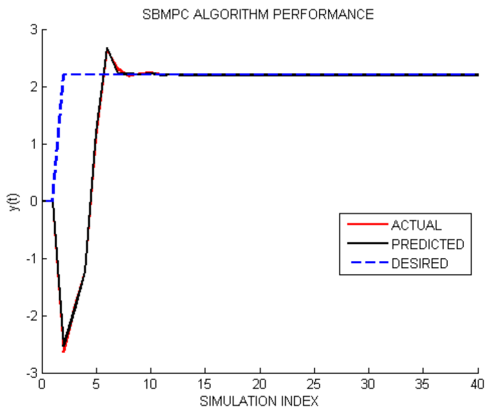

(b)

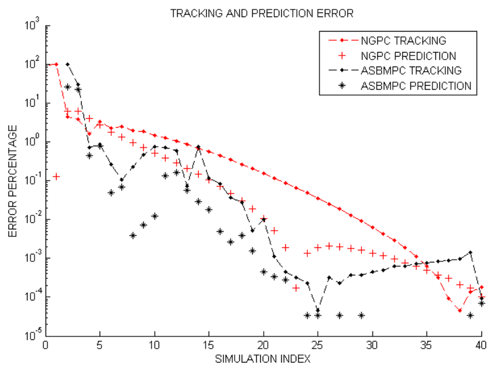

(c)

Figure 3.7: Case 1 Results—$\beta = 1.0$ step tracking. After a 30-second training phase, the reference was tracked using GPC (a) and SBMPC (b). Both converge rapidly to the desired set point and achieve steady state estimation and control errors of zero. In the error plot (c), tracking error is the absolute percent difference between desired and actual outputs, while prediction error is the absolute percent difference between predicted and actual outputs.

In Figs. 3.7(a) and 3.7(b) we see the control comparison under the conditions $\beta = 1.0$. Both algorithms produce good performance, and although the plant is nonlinear, there is no significant disadvantage caused by linearizing the system because local minima are not encountered. From the plots it is evident that both algorithms are able to achieve low errors for this case. For the $\beta = 0.2$ case, Figs. 3.8(a) and 3.8(b) show that Neural GPC converges to a suboptimal local minimum and hence fails to track the desired reference, whereas SBMPC converges to the global minimum and has near zero steady state tracking error. For the third case, with variable β, both algorithms achieve good performance, tracking the set point as shown in Figs. 3.7(a) and 3.7(b).

3.2.3 Run Time Statistics and Real Time Feasibility

The computational times presented in Table 4.2 were measured during simulation execution for each of the three cases. The timing period begins before the SBMPC routine and ends after SBMPC has computed the next control input. Median and worst case performance over each 200-timestep simulation run are presented. Both algorithms were implemented in C on a 2.0 GHz quad-core AMD processor.

The Adaptive SBMPC algorithm solves the nonlinear optimization more efficiently than Neural GPC. In particular, as seen in Table 4.2, it requires far less computational time per step, and as seen in Figs. 3.7(c), 3.8(c), and 3.9(c), it requires fewer time steps to converge to a near-optimal solution. Note that GPC uses a Newton-Rhaphson method relying on plant linearization while SBMPC is based on a graph search method that directly propagates the nonlinear plant model and is guaranteed to find the global minimum given sufficient sampling and sufficient length of the prediction horizon. Hence, SBMPC, unlike GPC, is not susceptible to slow convergence when the second derivative is small, large overshoot and constraint violations due to a non-well-behaved first derivative, and non-convergence due to poor initial estimates.

Table 3.1: Adaptive SBMPC Run Time Statistics: Case 1

Median CPU Times		
Plant Configuration	Control Algorithm	
	GPC	SBMPC
Case 1	146 MFLOPS	2.67 MFLOPS
Case 2	42.0 MFLOPS	4.83 MFLOPS
Case 3	148 MFLOPS	2.50 MFLOPS
Longest CPU Times		
Plant Configuration	Control Algorithm	
	GPC	SBMPC
Case 1	597 MFLOPS	5.33 MFLOPS
Case 2	166 MFLOPS	13.8 MFLOPS
Case 3	597 MFLOPS	6.50 MFLOPS

3.3 Summary

Adaptive SBMPC, a new approach to adaptive nonlinear model predictive control, is presented and applied in simulation to a benchmark nonlinear control problem from the literature. The nonlinear dynamics of the SISO benchmark system were learned and applied in feed-forward control. Efficient nonlinear optimization was performed and close reference tracking was achieved. The SBMPO algorithm for optimization is shown to be a complete search algorithm subject to sufficient length of the prediction horizon. Unlike approaches that optimize by linearization, global convergence is achievable even when numerous local minima exist. For comparison, the established NMPC technique, Neural GPC was also implemented. Through simulated identification and control problems, adaptive SBMPC was shown to be capable of faster and more optimal convergence.

Results were presented for a system with fixed as well as changing dynamics, which highlights the adaptive nature of the control system. One limitation of this and other NMPC approaches is the breakdown due to complexity for large numbers of inputs and outputs. However, SBMPO is naturally compatible with parallel computation since it uses a divide-and-conquer approach perform optimization. Node expansion is the most costly portion of the Adaptive SBMPC algorithm, but these computations can be implemented in parallel. There is also a possibility for significant computational improvement with the addition of search heuristics and a parallel implementation of portions of the algorithm. Within an A* optimization, a good heuristic can dramatically reduce the number of nodes that are expanded, and performing the edge cost calculation in parallel on multiple cores could significantly reduce the required run time per node. Future work includes the incorporation of learned heuristic functions for problems where no good heuristic is known based on first principles.

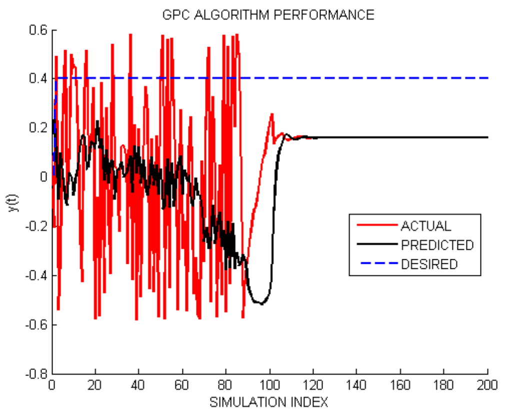

(a)

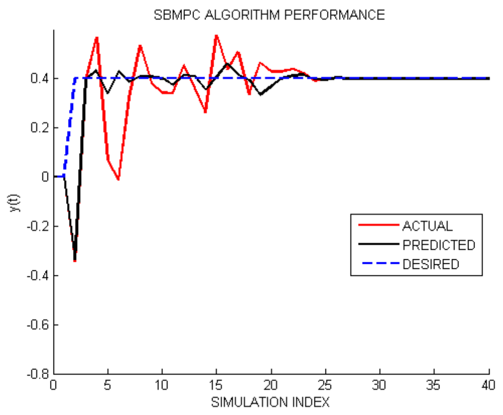

(b)

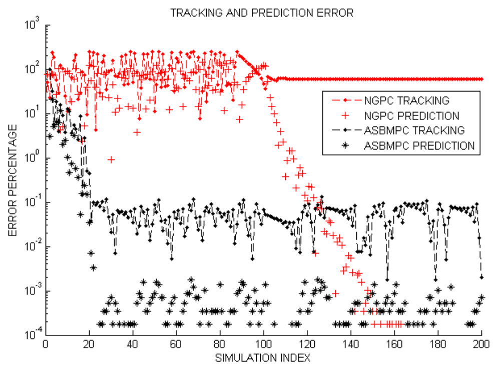

(c)

Figure 3.8: Case 2 Results—$\beta = 0.2$ step tracking. After a 90-second training phase, the reference was tracked using GPC (a) and SBMPC (b). Both converge more slowly than in the previous case. However Neural GPC convergence takes 100 simulation steps while the Adaptive SBMPC method converges within 20 steps. The GPC suboptimal convergence state is due to finding a local minimum. The error plot (c) indicates a difference of 2.5 orders of magnitude between globally optimal convergence of SBMPC and the locally optimal convergence of GPC.

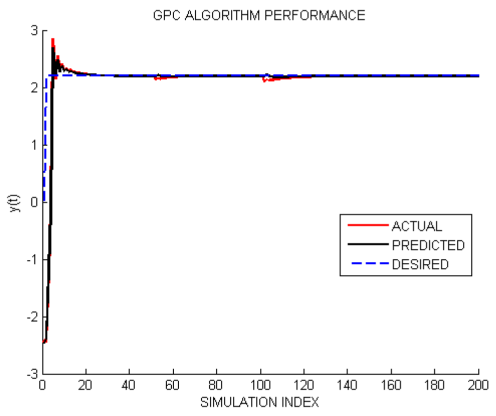

(a)

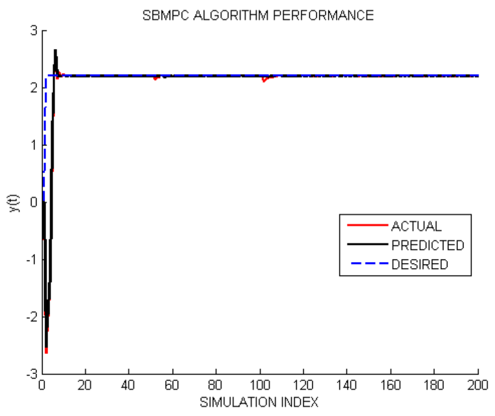

(b)

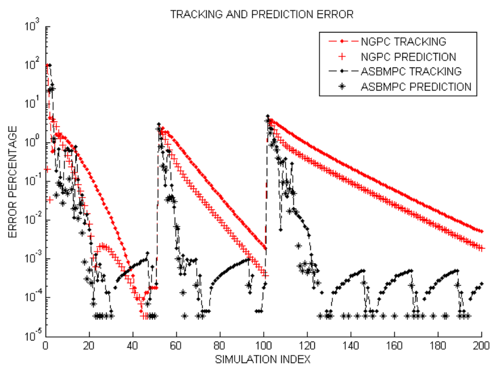

(c)

Figure 3.9: Case 3 Results—Variable β step tracking. After a 30-second training phase, the reference was tracked using GPC (a) and SBMPC (b). Both converge rapidly to the desired set point and achieve low errors, maintaining good performance as the plant dynamics undergo abrupt changes at time steps 50 and 100. The error plot (c) indicates that Adaptive SBMPC converges more quickly than Neural GPC in response to these changes.

CHAPTER 4

APPLICATION TO COMBUSTION CONTROL

4.1 Introduction

Energy policy and the rising cost of fossil fuels has highlighted the need for efficient and reliable methods to control the combustion processes of power plants. Legislation that taxes or sets limits on carbon emissions is becoming more common [46][61][3], which has increased demand for control systems that reliably meet constraints on emissions outputs.

When controlling a combustion system, constraints on inputs and outputs are necessary in order to meet power demands, ensure safe operating levels, or regulate environmental pollutants. For these reasons, the industry's need for handling these constraints has steadily increased, and Model Predictive Control (MPC) is arguably the control methodology most suitable to handle them [51]. MPC uses an internal model that represents the system to be controlled, and produces a future sequence of control inputs and the corresponding output trajectory that optimizes a cost function, subject to constraints on functions of the inputs and outputs. Receding horizon MPC approaches use this model to predict several steps in the future while implementing only the immediate next step.

MPC is commonly applied in simulations to power plants [9][47][38][23], and, for applications where no closed-form model is available, is typically applied in conjunction with an identified system model. Linear MPC techniques often use a Least-Squares, Gradient Descent, or Newton method to fit a linear model to observed data [59]. Nonlinear MPC techniques, which are far less commonly used, often fit a Neural Network, Neuro-Fuzzy, Nonlinear Polynomial, or other Nonlinear State Space model to predict system behavior [60].

Due to environmental effects, normal wear, and fatigue, power plant combustion chambers can exhibit time-dependent dynamic behavior. Furthermore, the addition of solar and wind power plants, which provide intermittent power to the grid, has caused the duty cycle of traditional power plants to fluctuate more than ever before. The neural network model form is suitable for modeling the nonlinearities and time variation, which lead to suboptimal performance when they are ignored. The Neural Generalized Predictive Control (Neural GPC) method [67][27] consists of a Back Propagation Neural Network (BPN) and Newton-Raphson cost optimization. It is best able to handle problems with nonlinearities and time variation among existing NMPC methods because it balances speed of optimization with adaptive capability.

An analytical model for coal combustion has been derived [8]. This model has been used in a Single-Input Single-Output (SISO) simulation of Gaussian Process NMPC [25], which requires *a priori* specification of the plant's dynamic equations and achieves rapid online computational speed, at the expense of significant offline computation and a lack of robustness to plant changes. This research solves the same problem in simulation using an adaptive algorithm that does not require prior knowledge other than the order of plant dynamics. Furthermore, the control problem is extended to multiple inputs and outputs and time-varying plant dynamics.

Chapter 3 of this dissertation presented an adaptive NMPC approach known as Adaptive Sampling Based Model Predictive Control (Adaptive SBMPC) and contained a description of the algorithm, theory, and SISO examples. The application in simulation to solve a relevant NMPC problem is given here in Part 2. Results of this chapter include a comparison between Adaptive SBMPC and Neural GPC for the simulated Multiple-Input, Multiple-Output (MIMO) combustion problem. The results are the first published for either control method for a system which is both MIMO and time varying.

The chapter is organized as follows: Section 4.2 describes the plant and neural network identification results using both RBF and BPN neural networks. Section 4.3 presents the control results of the combustion simulations, including SISO, MIMO, and time-varying MIMO cases in Sections 4.3.1, 4.3.2, and 4.3.3, respectively. Finally, Section 4.4 gives concluding remarks.

4.2 Combustion Plant and Neural Network Identification

A simulation of the application being studied, power plant combustion, was used to demonstrate both Adaptive SBMPC and Neural GPC. The plant description of Section 4.2.1 is taken as ground truth, and the dynamics described are initially unknown to the algorithms. The RBF and BPN neural network identification algorithms are tasked with learning the plant behavior. In Section 4.2.2, results from the training phase are given.

4.2.1 Description of the Plant

The PK 401 boiler, used for power generation of up to 200 megawatts, has a combustion process that has been modeled by Čretnik [14]. For this research, two inputs and three outputs are considered. The first input, the air flow damper angle $\phi \in [0^\circ, 90^\circ]$ determines the volume flow rate of air, Φ (m^3/s), according to the relationship

$$\Phi = \begin{cases} \frac{\Phi_{\max}}{2} \exp\left(\frac{\phi-45}{15}\right), & 0^\circ \leq \phi \leq 45^\circ, \\ \frac{\Phi_{\max}}{2}\left(2-\exp\left(\frac{45-\phi}{15}\right)\right), & 45^\circ < \phi \leq 90^\circ, \end{cases} \tag{4.1}$$

where $\Phi_{\max}$ specifies the air flow when the damper is fully open. This nonlinear damper-to-flow relationship is used by Čretnik in [8]. Air is assumed to be composed of 79% nitrogen and 21% oxygen.

The second input is fuel mass rate $\Phi_f \in [0.7, 1.3]$ kg/s. Modifying these two inputs influences the chemical concentrations in the flue gas exiting the boiler. The three gas concentrations of interest, x_{O_2}, x_{CO}, $x_{CO_2} \in [0\%, 100\%]$, are the outputs of the control system and change according to the equations

$$\dot{x}_{O_2} = \frac{-x_{O_2}\left(\Phi + \Phi_f(V_d - V_O) + 21\Phi - 100V_O\Phi_f\right)}{V}, \tag{4.2}$$

$$\dot{x}_{CO} = \frac{-x_{CO}\left(\Phi + \Phi_f(V_d - V_O) + 1.866ax_c^f\Phi_f\right)}{V}, \tag{4.3}$$

$$\dot{x}_{CO_2} = \frac{-x_{CO_2}\left(\Phi + \Phi_f(V_d - V_O) + 1.866(1-a)x_c^f\Phi_f\right)}{V}, \tag{4.4}$$

where V_d (m^3/kg) is the theoretical volume of gas produced by the combustion of 1 kg of fuel, V_O (m^3/kg) is the theoretical volume of O_2 needed for total combustion of 1 kg of fuel, a is the fraction of Carbon that reacts to form CO, x_C^f is the Carbon fraction of the fuel mass, and V (m^3) is the chamber volume. The numerical value of each of the parameters used in simulation is given in Table C.1 of Appendix C.

The concentration of x_{O_2} is monitored as a metric of efficiency. For this particular boiler, we compare x_{O_2} to the value that is optimal for burning efficiency $x_{O_2,opt}$, a value that is prescribed in [15] as an empirical function of Φ_f. When the flue concentration is above optimal, the oxygen-rich reaction is burning at excessive temperature, and energy is wasted via heat in the flue gas. In oxygen-deficient reactions, where the flue concentration is below optimal, energy is wasted in the form of unburned fuel escaping in the flue gas.

In order to consider the boiler's environmental impact as well as its mechanical efficiency, the O_2-only analytical model used by Grancharova et al. has been extended to compute carbon monoxide (CO) and carbon dioxide (CO_2) concentrations as well. Both pollutants are regulated by the UN Kyoto Protocol as well as by governments of individual nations, which tax excessive carbon emissions [16]. CO_2 is the most prominent and strictly-regulated greenhouse gas, and in proximity to humans, CO excess is harmful and potentially fatal. While this research includes these two greenhouse gasses, other key pollutants such as nitrous oxides (NO_x) are not considered because their formation process is not well understood [32].

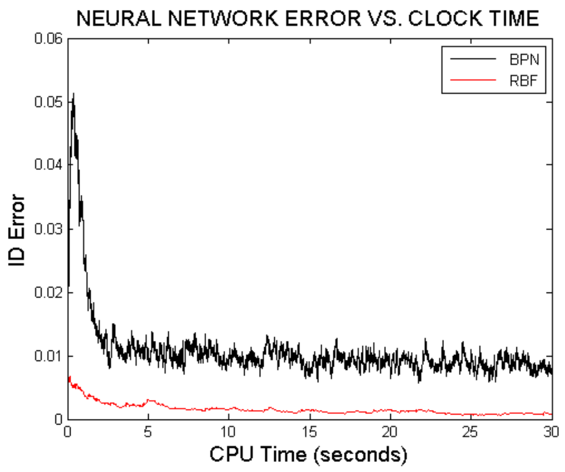

Figure 4.1: Single Output Neural Network ID comparison. Each neural network is trained with sequential input and output data during the training phase. Prediction error is based only on prediction of x_{O2}.

4.2.2 Neural Network Identification

Identification of the nonlinear system dynamics was achieved by training both RBF and BPN neural network models. The MRAN identification algorithm [73], described in Part 1, was used to train the RBF network, while the more standard back propagation adaptation rule [76] was used to train the BPN network. A key distinction between the two identification approaches is that for BPN, a fixed network size must be assumed, while the RBF adds new hidden units when needed to model newly seen data.

For this simulation, the BPN network was initialized with random parameters for each hidden unit, and the RBF network was initialized with no hidden units. To determine the network size for the BPN network, system identification simulations were run with integer network sizes between 1 and 400 hidden units. The network size of 39 hidden units produced the smallest cumulative error, so this network size was assumed for the cases presented. The ability to learn the size of the network while the identification algorithm runs is an advantage of MRAN learning over back propagation.

The simulation was run on one CPU core of a 2.0 GHz quad-core AMD laptop with 6 gigabytes of RAM. All algorithms were implemented in C.

During neural network training, a sequence of white noise over the allowable range for each input was provided as the open loop excitation signal. These signals as well as the measured outputs that result from the inputs were sequentially passed to the identification algorithms. Identical sequences were used for the

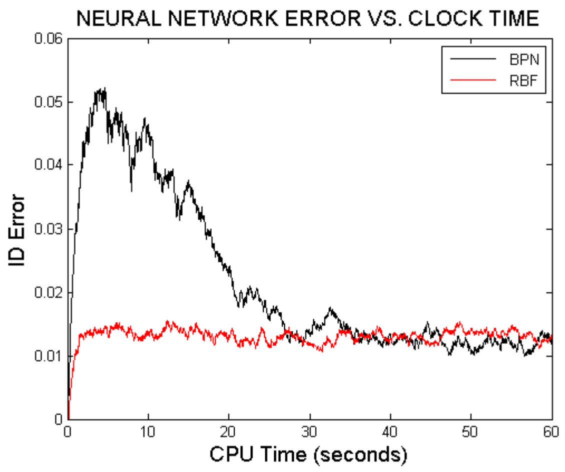

Figure 4.2: Multiple Output Neural Network ID comparison. Identification error is computed based on predictions for the three outputs, x_{O2}, x_{CO}, x_{CO2}. For this case, the BPN adaptation converges more slowly, but two identification methods eventually attain comparable prediction error.

BPN and RBF networks. Comparison Figs. 4.2.2 and 4.2.2 plot the error metric

$$e_{\text{pred}}(k) = \sum_{i=0}^{100} \|y(k-i) - \hat{y}(k-i)\|, \tag{4.5}$$

where $\|\cdot\|$ denotes the Euclidean norm, on the vertical axis and the CPU time on the horizontal axis. While in the single output case, Fig. 4.2.2, the RBF network predicts with lower error than the BPN network, the prediction error between the two is comparable in the three output case, Fig. 4.2.2.

4.2.3 Neural Network Tuning

The process of tuning the MRAN algorithm includes the tuning of the Extended Kalman Filter parameters, q, p_0, and R. These were tuned according to the procedure given in [48]. Next, the error thresholds, E_1, E_2, and, E_3, and the pruning thresholds, $\delta_{p,1}$ and $\delta_{p,2}$, were given values of 0, resulting in automatic addition of a hidden unit, with no pruning possible, at each time step. The remaining parameters were set with an initial guess based on parameters used in another application of MRAN [73]. From this starting point, the thresholds were systematically increased by monitoring the error data values of e_1, e_2, and e_3 during the execution of MRAN with training data. These initial values result in rapid growth of the number of hidden units. The network was then tuned to slow this growth. After each run, each error threshold parameter was modified by computing the 20^{th} percentile of the corresponding error data. This process was repeated until the resulting post-training size of the neural network decreased to about 200. This size represented an acceptable trade-off between prediction accuracy and computational time. Likewise, the pruning thresholds, $\delta_{p,1}$ and $\delta_{p,2}$, were modified using the 1^{st} and $\frac{1}{10}^{th}$ percentile values of e_2. The resulting tuning parameter choices are given in Table D.1 of Appendix D.

The tuning parameters for the BPN identification algorithm, given in Table D.2 of Appendix D, were chosen through an iterative process, beginning with an initial guess based on parameters α, η, and L that were used in another application [48]. From this starting point, the parameters were modified and used for an identification simulation. The parameter configuration yielding the smallest overall prediction error was retained. Since BPN requires outputs scaled within 0 and 1, the scaling multiplier and biases were selected to transform the outputs into the range [0,1], based on the minimum and maximum y values observed in the training data. The number of hidden units N_H was selected by running the BPN algorithm on the training data for each N_H between 1 and 400 and selecting the value resulting in the lowest prediction error.

4.3 Control Results

In order to clearly compare the control results, Adaptive SBMPC was implemented not only in the typical configuration, using the RBF network, but also with the BPN network used by Neural GPC. These two implementations are here referred to as SBMPC$_{RBF}$ and SBMPC$_{BPN}$. Three cases are presented: a SISO problem, a MIMO problem, and a time-varying MIMO problem. The two control inputs and outputs are

$$u_1 = \phi, \quad u_2 = \Phi_f, \tag{4.6}$$

and the three plant outputs are

$$y_1 = x_{\mathrm{O}_2}, \quad y_2 = x_{\mathrm{CO}}, \quad y_3 = x_{\mathrm{CO}_2}. \tag{4.7}$$

The second input, fuel mass rate Φ_f, is prescribed over time as an exogenous input in Case 1, but specified by SBMPC or GPC as a control input in Cases 2 and 3. The outputs to be controlled are the flue volume concentrations of oxygen, carbon dioxide, and carbon monoxide.

For each trial, 120 seconds of processor time was used to initially train the neural network. During this phase, inputs consisted of uniform white noise within the constrained range for each input, $u_1(k) \in [0°, 90°]$ and $u_2(k) \in [0.7, 1.3]$kg/sec. The MRAN learning algorithm starts with an empty neural network and learns the network size during this training period. The back propagation network, initialized with random hidden unit parameters between -0.5 and 0.5, assumed a fixed network size, which was provided *a priori*. The same prediction horizon $N = 4$ and control horizon $N_C = 2$ were used for both SBMPC and GPC. The complete list of tuning parameters is given in Appendix D.

4.3.1 Case 1: Time-Invariant SISO Problem

The first simulated case is the problem addressed by Grancharova et al. in Problem P3 of [25], in which only the mechanical efficiency of the burner is considered for optimization. In this case, Φ_f is specified externally, and only a single control input ϕ is used. The control task is to seek the concentration of oxygen x_{O_2} in the flue gas that is optimal for burning efficiency $x_{\mathrm{O}_2,\mathrm{opt}}$, a value that is prescribed in [15] as an empirical function of Φ_f. The cost function being optimized,

$$C = \sum_{i=0}^{N-1} C_{\mathrm{mec}}(i) \tag{4.8}$$

has a single quadratic cost term

$$C_{\mathrm{mec}}(i) = \big(x_{\mathrm{O}_2}(k+i) - x_{\mathrm{O}_2,\mathrm{opt}}(k+i)\big)^2, \tag{4.9}$$

and control signals are determined by sampling inputs in bounded increments such that

$$-0.5^\circ \leq \Delta u_1 \leq 0.5^\circ \tag{4.10}$$

in any two consecutive time steps.

After the 60-second learning phase for Case 1, the number of RBF hidden units had converged to 19. The number of hidden units remained constant throughout the control phase of the simulation. SBMPC and GPC both successfully used the learned models to track the reference signal. Figure 4.3 shows results from three run configurations and presents the results when Neural GPC (a), SBMPC$_{RBF}$ (b), and SBMPC$_{BPN}$ were used. SBMPC demonstrated more rapid convergence for the SISO case, while requiring less computation time as seen in Table 4.2. The neural network performance was similar, as seen by comparing SBMPC$_{RBF}$ and SBMPC$_{BPN}$ plots, although SBMPC$_{RBF}$ achieved lower overshoot, due to initially larger prediction errors of the BPN network.

4.3.2 Case 2: Introducing a Carbon Penalty Cost

Case 2, and extension to three outputs, considers greenhouse gases CO and CO_2 in order to control environmental impact of the power plant. The updated cost function is

$$C = \sum_{i=0}^{N-1} C_{\mathrm{env}}(i) + C_{\mathrm{mec}}(i), \tag{4.11}$$

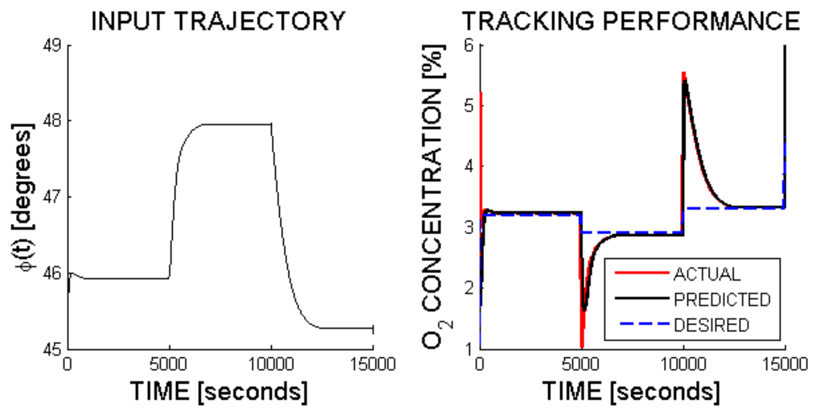

(a)

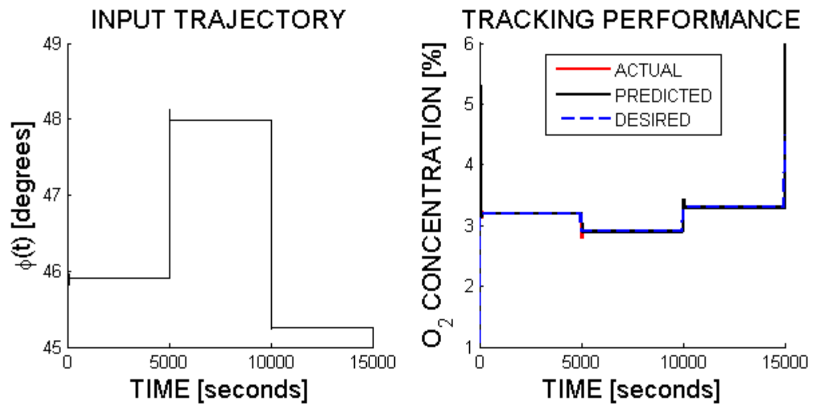

(b)

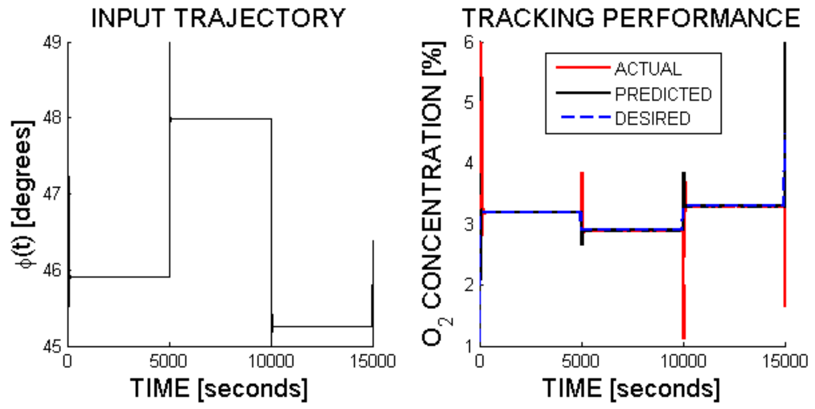

(c)

Figure 4.3: Case 1 Results—Step Tracking.The reference input was tracked using Neural GPC (a), SBMPC$_{RBF}$ (b), and SBMPC$_{BPN}$ (c). The neural network type affects overshoot due to larger BPN prediction errors. SBMPC convergence, however, is still more rapid than that of GPC regardless of neural network choice.

where

$$C_{\text{env}} = C_{\text{CO}} + C_{\text{CO}_2} \tag{4.12}$$

and

$$C_{\text{CO}} = \begin{cases} 0, & x_{\text{CO}} < L_{\text{CO}}, \\ (x_{\text{CO}} - L_{\text{CO}})P_{\text{CO}}, & x_{\text{CO}} \geq L_{\text{CO}}, \end{cases} \tag{4.13}$$

$$C_{\text{CO}_2} = \begin{cases} 0, & x_{\text{CO}_2} < L_{\text{CO}_2}, \\ (x_{\text{CO}_2} - L_{\text{CO}_2})P_{\text{CO}_2}, & x_{\text{CO}_2} \geq L_{\text{CO}_2}. \end{cases} \tag{4.14}$$

It introduces terms that linearly penalize pollutant levels above the respective thresholds L_{CO_2} and L_{CO} with penalty slopes P_{CO} and P_{CO_2}. The limitations on CO and CO_2 are implemented as soft constraints via these linear penalties rather than hard constraints. This is done because initial conditions and time variation of the plant yield states in violation of the desired range of outputs. Starting from this initial condition, the use of hard constraints would allow no feasible solutions. Instead, a large penalty was placed on outputs above desired levels to so that optimal control strategies must quickly bring the outputs into compliance.

For Cases 2 and 3, there are two control inputs, air inlet damper angle ϕ and fuel rate Φ_f. In addition to the constraints on the damper angle, fuel rate is constrained on $\{u_{min}, u_{max}\} = \{0.7 \text{ kg/s}, 1.3 \text{ kg/s}\}$. A saturation function,

$$u_{SAT}(u) = \begin{cases} u_{max}, & u < u_{min}, \\ u, & u_{min} \leq u \leq u_{max}, \\ u_{max}, & u > u_{max}, \end{cases} \tag{4.15}$$

is applied to the control signals, so that whenever either of the constraints is violated, the limiting value is passed to the plant instead. The reference trajectory $x_{\text{O}_2,\text{opt}}$, a sinusoid, simulates the requirement of power plant boilers to meet demands that vary over time.

For case 2, the length of the training phase was 120 seconds. After the training phase, the number of hidden units converged to 199. By the end of the simulation, the number of units had increased to 201.

The data for the second case, shown in Figures 4.4, 4.5, and 4.6, gives the Case 2 results for Neural GPC, SBMPC$_{RBF}$, and SBMPC$_{BPN}$. CO levels, which remained at zero throughout the control phase, are not plotted. Although CO was generated during the training phase, by nature of the combustion process the constraint on CO_2 is the more stringent of the two constraints, and meeting the constraint on CO_2 forced the CO level to zero. In Figure 4.4, Neural GPC fails to track the reference due to an input constraint violation, which occured because GPC produced a fuel rate that was out of bounds. The value $u_{2,SAT}$ is input to the

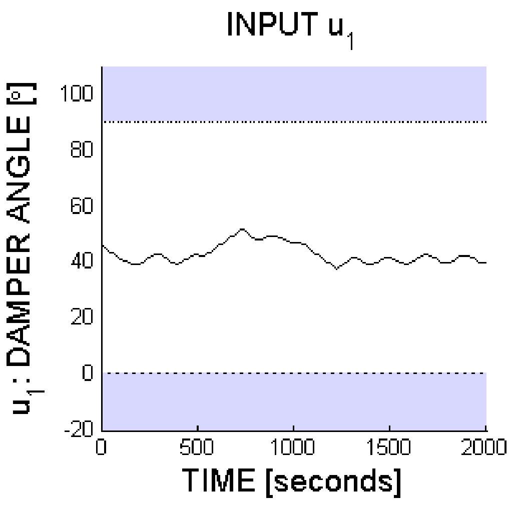

(a)

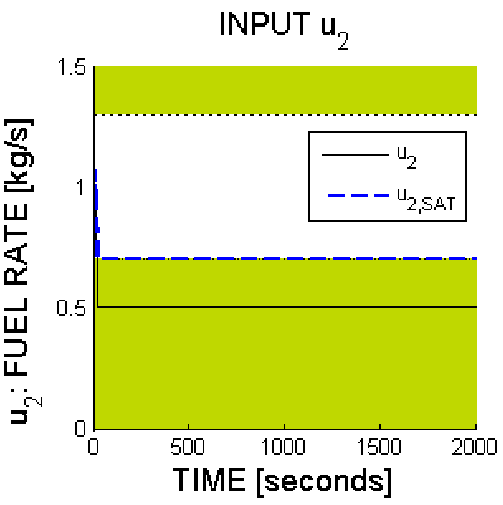

(b)

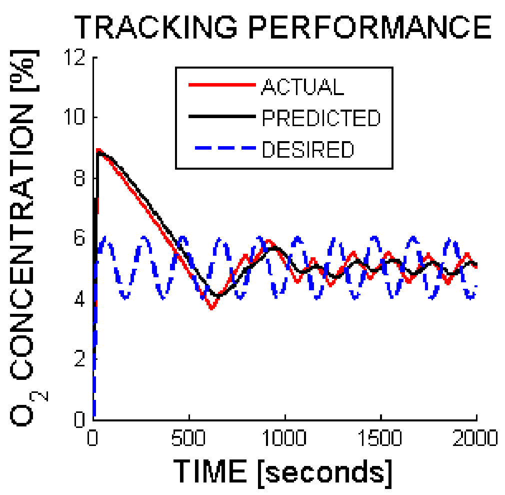

(c)

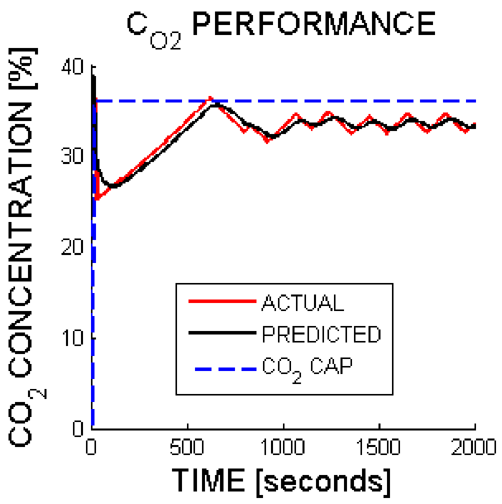

(d)

Figure 4.4: Neural GPC Case 2 Results. Penalties on CO and CO_2 are introduced and plots of inputs dampler angle (a) and fuel rate (b), and outputs oxygen concentration (c) and carbon dioxide concentration (d) are given. The shaded upper and lower regions on the input plots are infeasible regions beyond the input constraints. The value $u_{2,SAT}$ is input to the plant when the fuel rate constraint violation occurs.

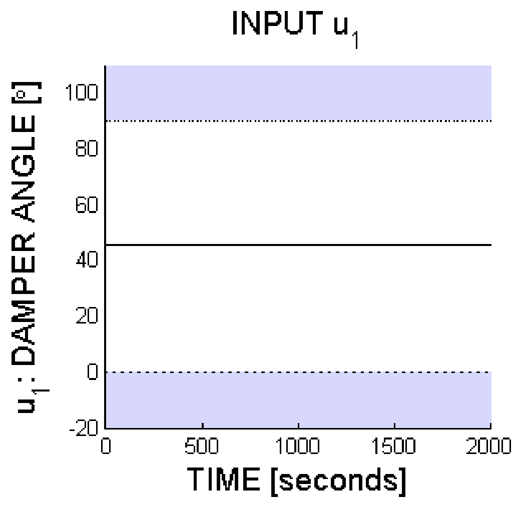

(a)

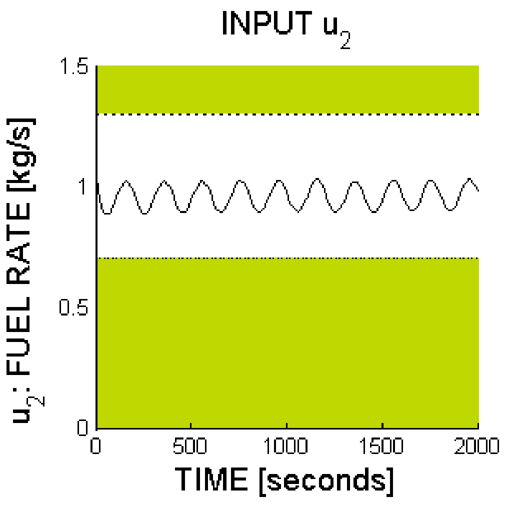

(b)

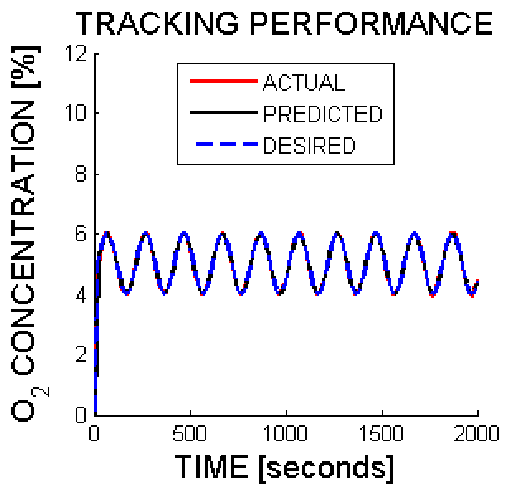

(c)

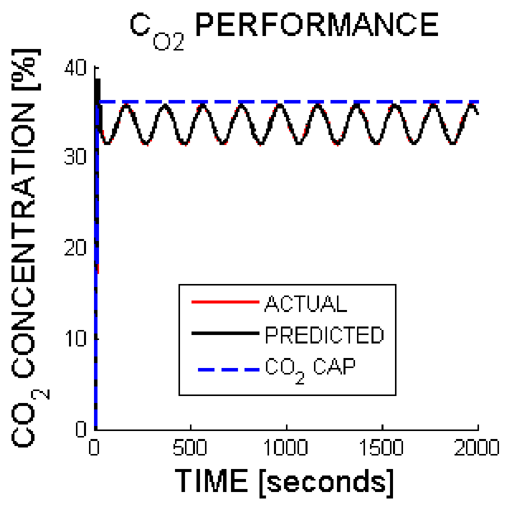

(d)

Figure 4.5: SBMPC$_{RBF}$ Case 2 Results. The performance of Adaptive SBMPC is shown. Plots of inputs dampler angle (a) and fuel rate (b), and outputs oxygen concentration (c) and carbon dioxide concentration (d) are given. The shaded upper and lower regions on the input plots are infeasible regions beyond the input constraints.

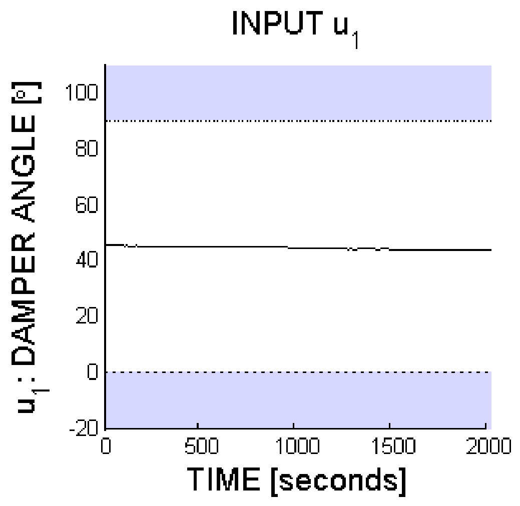

(a)

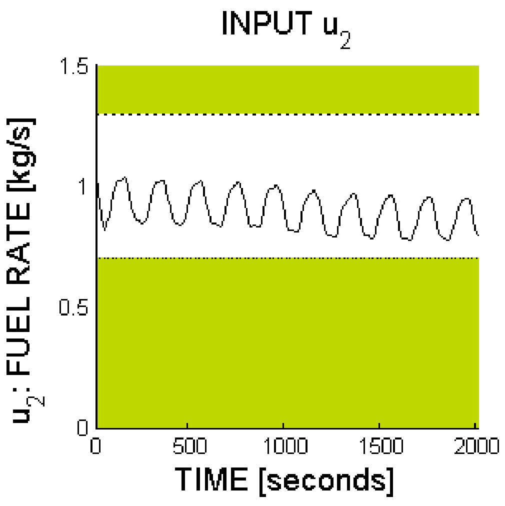

(b)

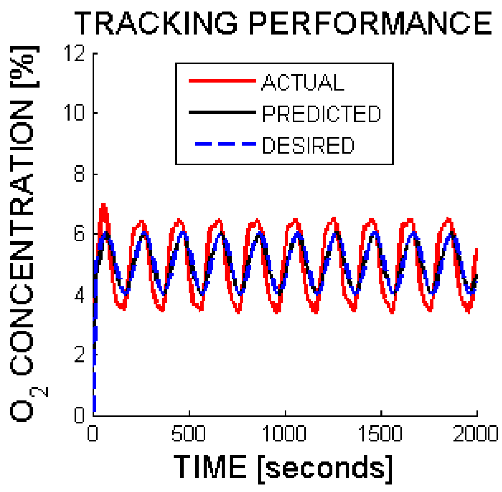

(c)

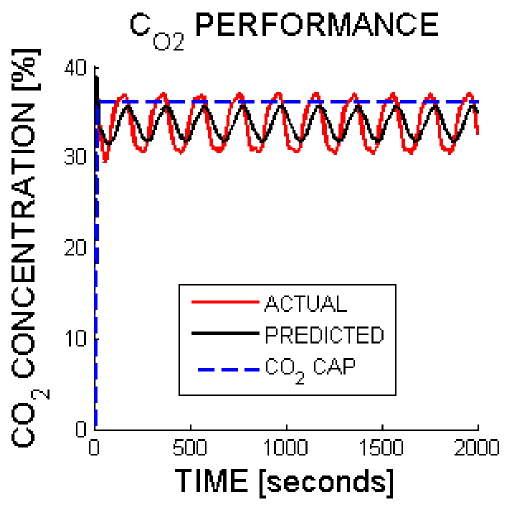

(d)

Figure 4.6: SBMPC$_{BPN}$ Case 2 Results. The performance of SBMPC using BPN identification is shown. Plots of inputs dampler angle (a) and fuel rate (b), and outputs oxygen concentration (c) and carbon dioxide concentration (d) are given. The shaded upper and lower regions on the input plots are infeasible regions beyond the input constraints.

Table 4.1: Time Variation of Simulation Plant Dynamics

Time (s)	Description	Quantitative Changes
0 to 5000	Normal boiler operation	None
500 to 1000	Constricted air flow	Φ_{max} is 36% smaller
1000 to 1500	Damp fuel	H_2O added to comprise 5% of fuel mass
1500 to 2000	Smaller chamber volume	15% reduction in volume

plant when the fuel rate constraint violation occurs. Because of this saturation of u_2, tracking performance is poor as u_1 alone lacks the control authority to track the reference. The damper angle alone lacks the control authority to track the reference trajectory. SBMPC$_{RBF}$ converges with small error and satisfaction of output constraints. Prediction errors are rapidly corrected in the first few time steps of the control phase. SBMPO$_{BPN}$ network similarly achieves overall constraint satisfaction, but the tracking is less effective due to the prediction error of BPN. The execution time of SBMPO$_{RBF}$ was improved over that of SBMPO$_{BPN}$, as seen in Table 4.2, which is primarily due to the smaller number of graph node expansions required when model predictions are more accurate. This time is also directly proportional to number of hidden units required to represent the system. The MRAN algorithm converged to 201 hidden units, whereas the fixed number of hidden units for the BPN network was 39.

4.3.3 Case 3: Control System Adaptation Under Changing Dynamics

The third simulation case demonstrates the versatility of the adaptive algorithms as changes in plant dynamics are introduced that require active model updates. The online identification algorithms are able to quickly adjust to changing plant behavior, either by back-propagation (BPN) or the EKF optimization of MRAN (RBF).

In the simulation, plant dynamics are applied as step parameter changes at the beginning of each 500 second interval of simulation time. The nature of the changing boiler dynamics is presented in Table 4.1. Each change is from the normal dynamic behavior, such that the changes mentioned are in effect during the interval but revert back to the normal values.

For case 3, the length to the training phase was 120 seconds. After the training phase, the number of hidden units converged to 199. By the end of the simulation, the number of units had increased to 205.

The data for the third case, shown in Figures 4.7, 4.8, and 4.9, indicates that after each shift in plant dynamics, the neural networks are adapted and prediction errors were corrected. In Figure 4.7, Neural GPC exhibited significant and sustained tracking error due to the u_2 input constraint violation that was

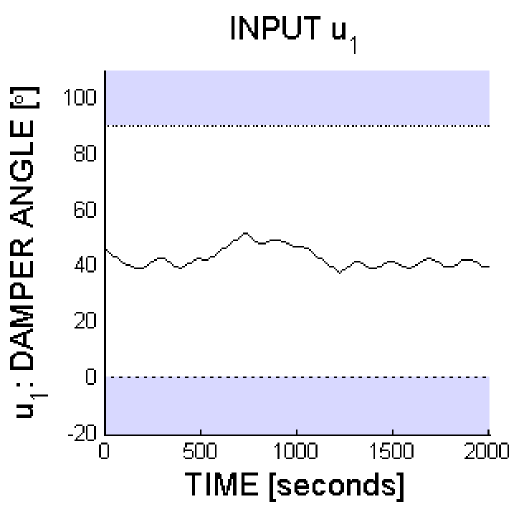

(a)

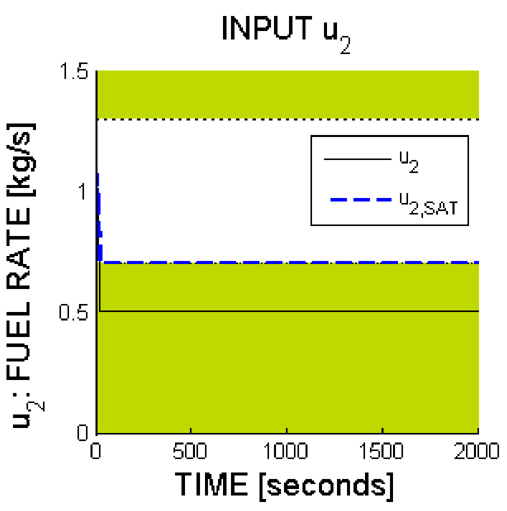

(b)

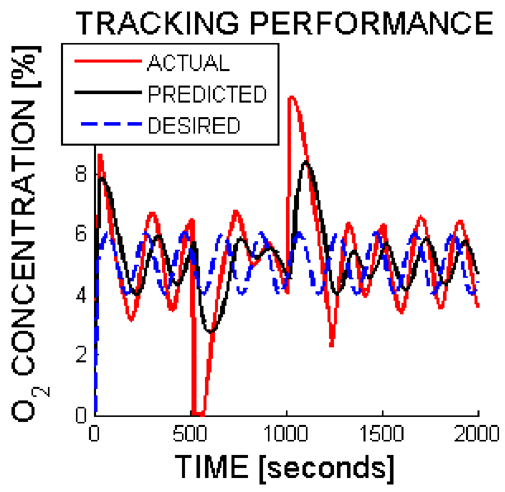

(c)

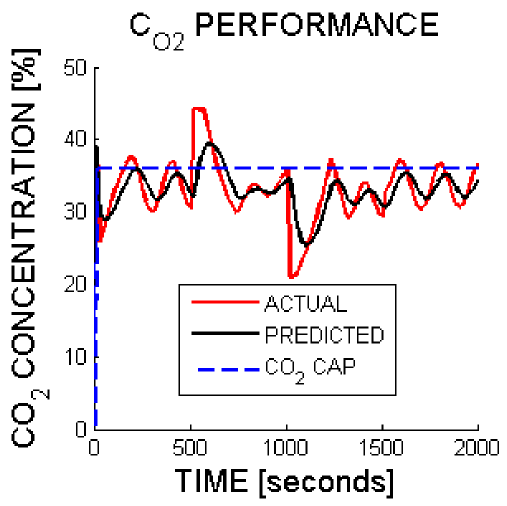

(d)

Figure 4.7: Neural GPC Case 3 Results. With plant changes occuring every 500 seconds, the model adapts and control inputs are updated simultaneously. Plots of inputs dampler angle (a) and fuel rate (b), and outputs oxygen concentration (c) and carbon dioxide concentration (d) are given. The shaded upper and lower regions on the input plots are infeasible regions beyond the input constraints. The value $u_{2,SAT}$ is input to the plant when the fuel rate constraint violation occurs.

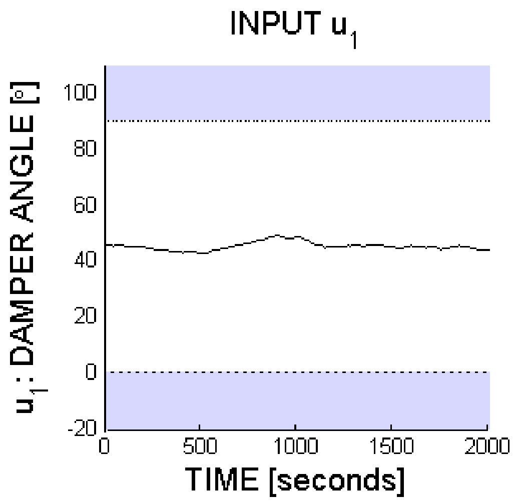

(a)

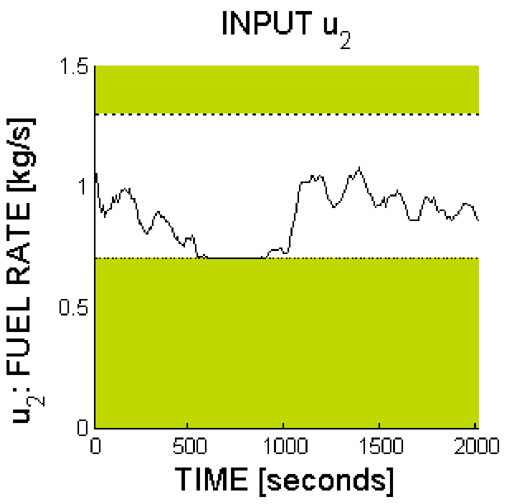

(b)

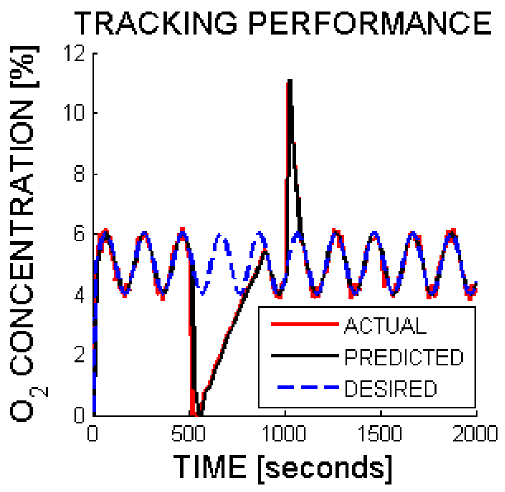

(c)

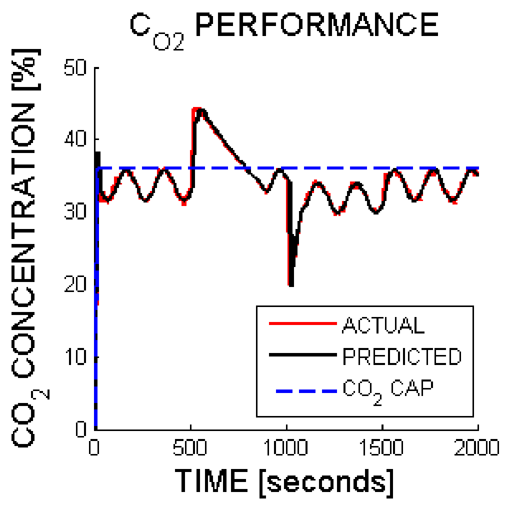

(d)

Figure 4.8: SBMPC$_{RBF}$ Case 3 Results. SBMPC$_{RBF}$ adapts to the plant changes at 500 second intervals. Plots of inputs dampler angle (a) and fuel rate (b), and outputs oxygen concentration (c) and carbon dioxide concentration (d) are given. The shaded upper and lower regions on the input plots are infeasible regions beyond the input constraints.

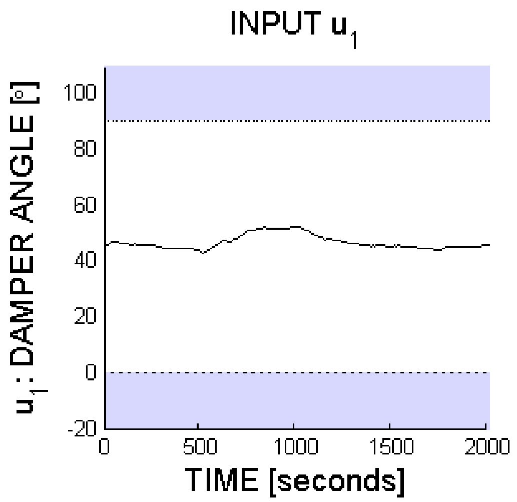

(a)

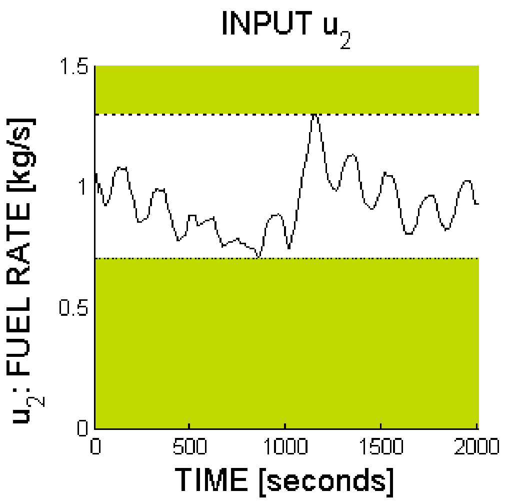

(b)

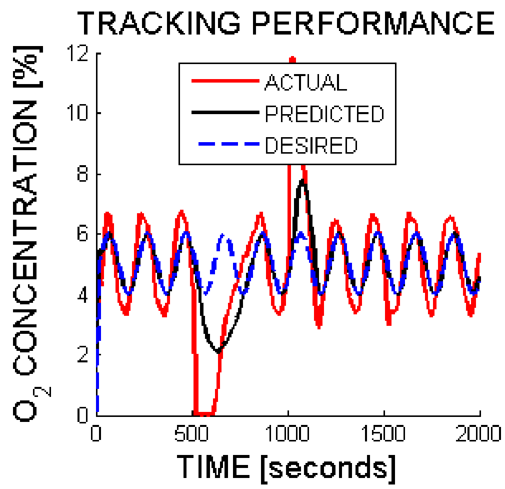

(c)

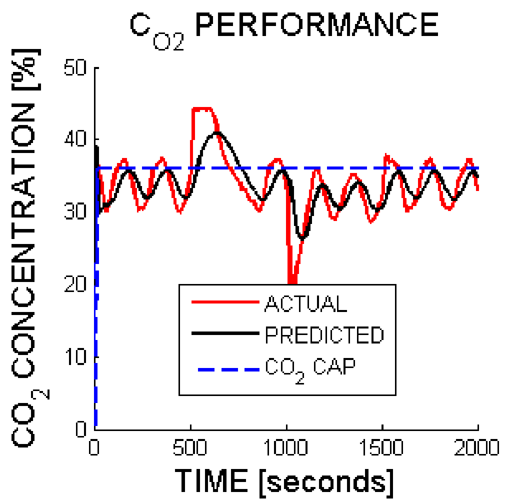

(d)

Figure 4.9: SBMPC$_{BPN}$ Case 3 Results. SBMPC$_{BPN}$ adapts to the plant changes at 500 second intervals. Plots of inputs dampler angle (a) and fuel rate (b), and outputs oxygen concentration (c) and carbon dioxide concentration (d) are given. The shaded upper and lower regions on the input plots are infeasible regions beyond the input constraints.

mentioned in Section 4.3.2. SBMPC$_{RBF}$ achieved similar tracking behavior and did not violate the input constraints. Similar results were produced by SBMPC$_{BPN}$, and no input constraints were violated. After each plant change, the neural networks quickly adapt to decrease the prediction error and, as in Case 2, the improved neural network prediction accuracy leads to lower computational cost for SBMPC$_{RBF}$ compared to SBMPC$_{BPN}$.

4.3.4 Run Time Statistics and Real Time Feasibility

The computational times presented in Table 4.2 were measured during simulation execution for each of the three cases. The timing period begins before the SBMPC or GPC control routine and ends after control routine has computed the next control input. Median and worst case performance over each simulation run are presented. Benchmarking statistics of median and longest CPU times are given. The longest CPU times reflect the transient solve times that occur initially, and the median CPU times indicate the computation cost after these transient periods. The control period for this application is 10 seconds, so the measured computational times are all within feasibility requirements for real time implementation. The real time requirement was met by each algorithm, but compared to GPC, SBMPC achieved better overall computation performance in addition to better tracking performance. Either algorithm could be tuned to run more quickly, but this comes at the expense of diminished tracking performance.

Table 4.2: Adaptive SBMPC Run Time Statistics

Median CPU Times			
Plant Configuration	Control Algorithm		
	N. GPC	SBMPC$_{RBF}$	SBMPC$_{BPN}$
Case 1	0.667 MFLOPS	0.500 MFLOPS	0.167 MFLOPS
Case 2	297 MFLOPS	97.2 MFLOPS	175 MFLOPS
Case 3	295 MFLOPS	132 MFLOPS	134 MFLOPS
Longest CPU Times			
Plant Configuration	Control Algorithm		
	N. GPC	SBMPC$_{RBF}$	SBMPC$_{BPN}$
Case 1	628 MFLOPS	137 MFLOPS	325MFLOPS
Case 2	1300 MFLOPS	297 MFLOPS	353 MFLOPS
Case 3	1225 MFLOPS	787 MFLOPS	1287 MFLOPS

4.3.5 Tuning the Control Algorithms

Compared with the neural network algorithms, the NMPC algorithms involved less effort to tune. For both SBMPC and GPC the prediction horizon $N = 4$ was chosen large enough to limit the overshoot of the transient behavior of the controlled system. For both algorithms the control horizon $N_C = 2$ was chosen to keep the computations small.

After these were fixed, the only remaining SBMPC tuning parameter is the branchout factor B. This parameter allows a trade-off between low computational cost (small B) and low tracking error (large B). The value $B = 60$ was selected after trial simulations with various values.

In order to tune the Newton solver of GPC, a solver tolerance ε, iteration limit $I_{\max}$, input constraint sharpness s, and damping factor λ were selected. The parameters ε and $I_{\max}$ allow for a trade-off between computational cost and tracking error, so they were selected to match the Case 1 steady state tracking error performance of SBMPC. The parameters s and λ, if not properly selected, led to instability of GPC. The damping factor was selected based on trial and error, which was a tedious process because this search spanned many orders of magnitude before producing stable results. The value of $s = 10^{-12}$ suggested in [67] produced stable solver results. Smaller values also produced stable results, while larger values led to instability. Even though the solver results were stable in the sense that the Newton solver converged to finite values, no tuning configuration was found that avoided an input constraint violation under the conditions of Cases 2 and 3.

4.4 Summary

Adaptive SBMPC, an adaptive approach to nonlinear model predictive control, is presented and applied in simulation to a combustion control problem from literature. For comparison, the nonlinear dynamics of coal combustion within a commercial boiler were learned and controlled using Neural GPC as well as Adaptive SBMPC. SBMPO was demonstrated as an efficient nonlinear optimization was performed and close reference tracking was achieved. Strengths of SBMPO, including computational speed, ease of tuning, and compatability with any model, were demonstrated in a MIMO nonlinear application. A direct comparison of the RBF and BPN neural network identification approaches is given using SBMPO optimization with each neural network type. The major strengths of the RBF network are the ability to modify the neural network structure during controller operation and the ability to learn plant behavior without the *a priori* specification of network size.

The original problem was extended to consider additional outputs and an additional control input as well as time-varying plant dynamics. Adaptive SBMPC was shown to be capable of rapid adjustments to changes in plant behavior and efficient nonlinear optimization for MIMO systems. The achieved execution times were, in the worst case, well under the ten-second sampling interval appropriate for feedback control of combustion.

For the purpose of comparison, results were presented for a combustion system identification and control problem. The MIMO system was identified using BPN and RBF neural networks and the Adaptive SBMPC and Neural GPC control systems were used to perform NMPC. The results presented in Case 3 are the first control results of a time-varying MIMO plant using Neural GPC as well as the first control results for SBMPC implemented with the BPN neural network model. The results indicate that both neural network structures are capable of representing the nonlinear system and both control methodologies easily handle the SISO control case. When the MIMO problem was considered, Neural GPC tended to violate the input constraints, which led to poor reference tracking. By design, Adaptive SBMPC cannot violate input constraints and good tracking results were achieved using both the RBF and BPN neural network structures. Adaptive SBMPC generally achieved better computational times and in the worst case did not exceed the control period of 10 seconds.

One potential improvement to Adaptive SBMPC, the learning of A* search heuristics for general nonlinear systems, which would enable further computational improvements, are planned as future work. This improved implementation will exploit past optimization cost information to speed up subsequent optimizations for the same plant. Further computational improvement is possible using parallel computations. During SBMPO execution, the majority of the the computational effort is spent on expansion of nodes. These expansions may be computed in parallel in order to leverage the capabilities of multi-core CPU or GPU hardware. These computation improvements will allow the application of Adaptive SBMPC to larger systems as well as systems with fast real-time computation requirements.

CHAPTER 5

APPLICATION TO FLOW SEPARATION CONTROL

5.1 Introduction

For decades, flow separation has been of particular interest in engineering applications for which improved aerodynamic performance is desired. Control of flow separation, both active and passive, is a key component of existing aviation technology. Passive control methods, such as leading edge surface roughness or the inclusion of vortex generators, rely on stationary structural components to produce a reduction or delay in separation effects. These techniques typically produce an early transition to turbulence or streamwise vortical structures, each of which has been shown to mitigate separation [40]. The effectiveness of passive techniques is limited in comparison with active techniques, which rely on powered mechanisms to alter the flow, especially when conditions different from the design point are considered [10]. These types of off-design conditions are common for aeronautical systems that are deployed in diverse environments, including micro-aerial vehicles and full-size aircraft that perform maneuvers.

The significant increase in capability and decrease in cost of computing hardware has led to the feasibility of active control techniques of increasing sophistication. Both open-loop and closed-loop control schemes have been applied to flow control problems and there is evidence that closed loop approaches offer significant improvement in performance over open-loop control [55][34].

Several areas of flow control research, including suppression of cavity flow resonant tones and mitigation of flow separation, have advanced rapidly in recent years as new technologies have both created demand for and expanded the capabilities of such systems. The study of cavity flow control has demonstrated that mathematical techniques such as Proper Orthogonal Decomposition (POD) and model reduction are effective tools for controlling aerodynamic systems [50][20] under limited Reynolds number conditions and a fixed angle of attack. While these studies incorporated flow visualization and analysis efforts to produce nonlinear models that are effective for developing open-loop control strategies, it has been more practical to linearize these models for the sake of computational efficiency when implementing real-time closed loop control [55][34].

Frequency domain methods have been applied to model and control the flow dynamics in flow control and related applications [49][12][42]. Nonlinear POD methods similar to those applied to cavity flow have also been used for flow separation [22]; however, these models exhibit little robustness and have only been used to perform open-loop control. Actuator development has also been key to the recent advances in the field of flow separation control. Both synthetic jet unsteady actuators [71][70] and steady microjet actuators [12][4] have been effective in closed-loop separation control experiments. Because of the advantage of high momentum capability with low power requirements [41], microjet arrays are used as actuators in this research. These actuators are capable of both pulsed and steady blowing.

Nonlinear model predictive control (NMPC) has been proposed for flow control, but "a huge numerical burden" is listed as a drawback of such methods [54]. The method presented in this dissertation, Adaptive Sampling Based Model Predictive Control (Adaptive SBMPC) [64], is a new paradigm for NMPC that is computationally efficient. Adaptive SBMPC differs from past adaptive, closed-loop approaches to flow control by identifying a *nonlinear* model for control. This chapter provides the experimental results, Particle Image Velocimetry (PIV) visualization, and detailed analysis of the flow separation control problem. The identification and control processing is executed in real time, demonstrating the potential of this method for in-flight application.

5.1.1 Control Objective

The primary objective of this research is to maximize the lift coefficient C_L by means of delaying the onset of separation as well as controlling flows with initially-separated boundary layers. The experimental model is not instrumented with sensors capable of approximating the drag coefficient C_D, but the lift-drag ratio C_L/C_D is typically also improved when flow separation is mitigated and C_L increases. Given a discrete time series of multiple sensor measurements located along an airfoil's chord (inputs), the proposed research aims to determine an optimal series of microjet pressure signals (outputs), maximizing the lift performance of the airfoil. The control system should achieve this task for a broad range of steady or dynamically-prescribed Reynolds numbers or angle of attack parameters. This is to be accomplished without direct measurement of either parameter and without the modification of tuning parameters.

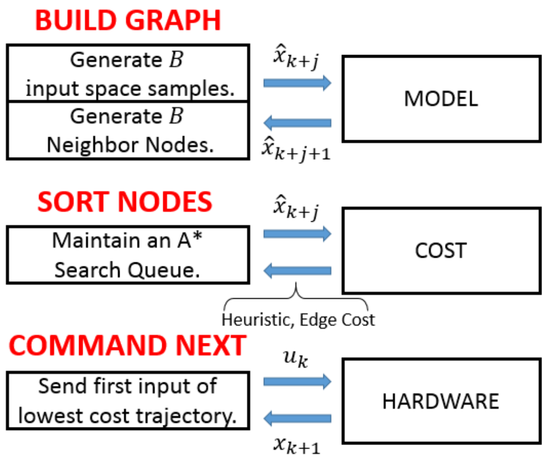

BUILD GRAPH
Generate B input space samples.
Generate B Neighbor Nodes.
$\hat{x}_{k+j}$
$\hat{x}_{k+j+1}$
MODEL
SORT NODES
Maintain an A* Search Queue.
$\hat{x}_{k+j}$
COST
Heuristic, Edge Cost
COMMAND NEXT
Send first input of lowest cost trajectory.
u_k
x_{k+1}
HARDWARE

Figure 5.1: Sampling Based Model Predictive Control Summary. The algorithm discretizes the input space and makes model-based state predictions, $\hat{x}_{k+j}$, in order to minimize a cost function.

5.2 Control Method

As a means of solving Model Predictive Optimization problems without computing gradients, Sampling Based Model Predictive Optimization (SBMPO) has been developed and implemented on both simulated and experimental platforms [64][63][19][18][1]. One key advantage of SBMPO is the ability to find globally optimal solutions, while other methods that rely on linearization are likely to converge to locally minimum solutions. A second advantage, computational efficiency enables the use of SBMPO to solve real time NMPC trajectories. When SBMPO is combined with a neural network model of system behavior, the overall method for identification and control is called *Adaptive Sampling Based Model Predictive Control* (*Adaptive SBMPC*). SBMPO may be applied to solve the nonlinear optimization problem,

$$\min_{\{\mathbf{u}(k),\ldots,\mathbf{u}(k+N-1)\}} \sum_{i=0}^{N-1} C\left(\mathbf{y}(k+i+1)-\mathbf{r}(k+i+1)\right), \tag{5.1}$$

subject to the nonlinear state space equations,

$$\begin{aligned} \mathbf{x}(k+i) &= g(\mathbf{x}(k+i-1),\mathbf{u}(k+i-1)), & (5.2)\\ \mathbf{y}(k) &= h(\mathbf{x}(k)), & (5.3) \end{aligned}$$

and the constraints,

$$\mathbf{x}(k+i) \in \mathbf{X}_{free}\ \forall\ \ i \le N, \tag{5.4}$$

$$\mathbf{u}(k+i) \in \mathbf{U}_{free}\ \forall\ \ i \le N, \tag{5.5}$$

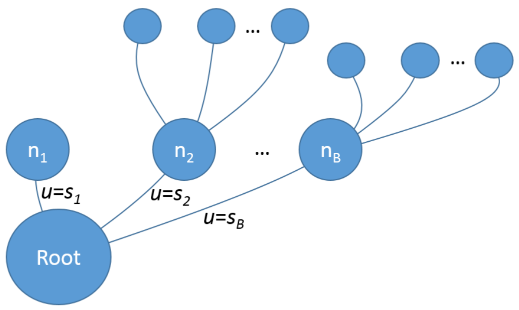

Figure 5.2: SBMPC Search Graph. The graph is built by expanding the most promising node to generate B child nodes. Each child node is assigned an input sample, which is propagated forward through the model to predict a state for that node. The potential cost of reaching that state is used to prioritize the nodes and select the most promising candidate for the next iteration of expansion.

where the cost function $C(\cdot) \geq 0$, $r(k)$ is the reference input, and $\mathbf{X}_{free}$ and $\mathbf{U}_{free}$ respectively represent the states and inputs that do not violate any of the problem constraints. SBMPC is described in Fig. 5.1 and is easily applied to both linear and nonlinear models, combining techniques for sampling the input domain with an efficient graph search method such as A*.

5.2.1 Sampling the Input Domain

The field of path planning in robotics has seen recent innovations that have used sampling techniques [39][44]. SBMPC involves the sampling of the space of allowable inputs. Halton sampling, in particular, is a method based on the low-discrepancy Halton sequences that has been shown to provide representative sample sets consisting of fewer points than sets generated using pseudo-random numbers or regular grids [56][11]. Satisfaction of input constraints is automatic because it is the allowable inputs that are sampled. Also, since the inputs are propagated forward through the model, no inversion of the model is needed.

5.2.2 The Graph Search

Using the current state and input samples, several new nodes are computed by propagating the model and adding to a graph with tree connectivity, as illustrated in Fig. 5.2. The branchout factor B, a tuning parameter of the algorithm, determines how many child nodes are generated when a particular parent node is expanded.

The uniform sampling density typically used for SBMPC may be transformed in order to achieve greater relative sampling density in a desired region of the input domain. In order to preserve input constraint satisfaction, the transformation must guarantee that no valid inputs are mapped to invalid inputs. Using a nonuniform sampling density can improve the performance of SBMPC by sampling large input changes more coarsely while sampling small input changes more finely. This finer sampling allows the trajectory to converge with small steady-state errors.

The Halton sequence algorithm, which is potentially used thousands of times at each time interval when the SBMPC routine is called, was a major contributor to the total runtime of SBMPC. During benchmark testing of C code on multiple machines, batches of 1 million elements of a Halton sequence were computed, and then precomputed batches of equivalent size were loaded from a binary file. The median CPU time required to compute the samples was 210 milliseconds, while the median time required to load the precomputed values was 1 millisecond; therefore, computing these samples offline and storing them in a binary file enables the run-time code to execute much faster while yielding identical results. The offline computation of these Halton samples is a contribution of this dissertation and reduces the run-time computational cost of SBMPC.

5.2.3 Nonlinear Modelling

Previous adaptive flow separation research has aimed to capture the nonlinear dynamics of the flow field by identifying an instantaneously linearized model that varies with time. The optimization of a linear model has the advantages of speed and simplicity over those that consider nonlinear models. The unmodeled dynamics, however, can cause such techniques to be suboptimal and even unstable.

Nonlinear POD Methods. Proper Orthogonal Decomposition (POD) techniques have been used to identify models in the form of polynomial difference equations [65][36] that are sufficient for open loop control design [50]. However, due to computational expense, closed loop flow control implementations have been limited to linear models [54]. Although SBMPO has the ability to optimize inputs to a POD model, POD models are steady state in nature and do not capture the transient behavior or hysteresis effects that are necessary to control dynamic stall.

SBMPO Compatibility with More General Models. A primary advantage of SBMPO over alternative optimization methods is that this technique has no intrinsic preference for linear models over nonlinear models, and the algorithm does not need to compute closed-form gradients. This allows SBMPO to be applied to a more general class of systems than could be handled by previous methods. Even systems with strong nonlinearities or non-differentiable functions can be optimized using SBMPO.

Nonlinear Neural Network Methods. The use of an artificial neural network allows nonlinear models to be identified in a general manner by composing a function that computes future outputs based on past states. For this application the state vector,

$$\mathbf{x_k} = (\mathbf{y}_{k-1}^T, \mathbf{y}_{k-2}^T, \ldots, \mathbf{y}_{k-n_y}^T, \mathbf{u}_{k-1}^T, \mathbf{u}_{k-2}^T, \ldots, \mathbf{u}_{k-n_u}^T)^T, \tag{5.6}$$

consists of n_u prior plant inputs and n_y outputs. The form,

$$\mathbf{y_k} = f(\mathbf{y}_{k-1}, \mathbf{y}_{k-2}, \ldots, \mathbf{y}_{k-n_y}, \mathbf{u}_{k-1}, \mathbf{u}_{k-2}, \ldots, \mathbf{u}_{k-n_u}) \equiv F(\mathbf{x_k}), \tag{5.7}$$

is known as as a nonlinear autoregressive exogenous inputs (NARX) model form because it is analogous to the autoregressive exogenus inputs (ARX) form for linear models. If $F(\mathbf{x_k})$ were a linear function, the equation would simplify to an ARX formulation,

$$\hat{\mathbf{y}}_k = A\mathbf{x}_k, \tag{5.8}$$

with the matrix A of constant coefficients.

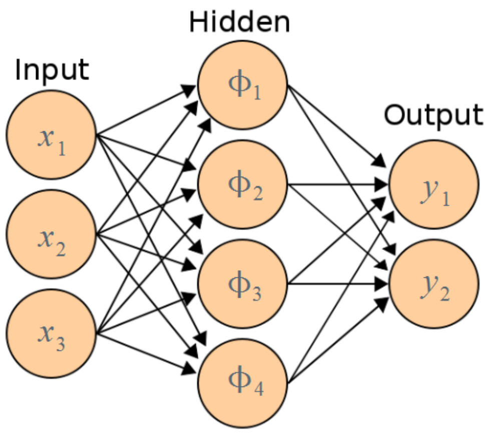

Figure 5.3: The layout of a sample RBF network consists of a hidden layer containing one hidden neuron for each distinct state pattern that the algorithm encounters. Collectively these pattern state vectors make up a basis with which all system dynamics are modeled. With enough of these hidden neurons the network is able to match arbitrarily complex nonlinear behavior.

While there are many ways to construct the nonlinear function $F(\mathbf{x_k})$, neural network methods construct this function as a composition of simpler functions called neural units, which can be arranged in series and parallel to form a network. The network implemented in this research has a two-layer structure first proposed by Platt [58]. This Resource Allocation Network (RAN) has for its first layer, a collection of neural units that respond in parallel when state $\mathbf{x}_k$ is nearby (according to the *Euclidean norm*) to a previously seen pattern. An extension of RAN, the Minimal Resource Allocation Network (MRAN)[73], is used in this research. MRAN adds a pruning step that keeps the neural network size reasonable by discarding neural units with insignificant contribution to the output. The Gaussian function,

$$\phi_i = \exp\left(-\frac{\|\mathbf{x}_k - \mu_i\|^2}{\sigma_i^2}\right), \tag{5.9}$$

is selected for the first layer because it achieves the desired radial symmetry using a simple computation that has closed-form derivatives. The second layer combines these Gaussian outputs in a weighted sum, yielding the Radial Basis Function (RBF) representation,

$$\mathbf{y} = F(\mathbf{x}_k) = \mathbf{a}_0 + \sum_{i=1}^{N} \mathbf{a}_i \phi_i. \tag{5.10}$$

For each of the N neural units, the MRAN algorithm must specify a basis vector μ_i, a Gaussian width σ_i, and weight coefficients $\mathbf{a_i}$. The detailed specification of the MRAN algorithm is given in Chapter 3.

5.3 Formulation of Lift Based Performance Function

Earlier approaches to adaptive flow separation control have passed one or more pressure transducers to the controller as elements of the system output vector y and select a single transducer signal as the controller's performance signal z [70]. However, often it is desirable to define a scalar performance function using more than one sensor. Unfortunately, due to the complexity of fluid dynamics, it is not obvious how each sensor contributes to the performance function. Rather than minimizing the pressure fluctuation at some selected sensor, this paper seeks to minimize a physics-based performance variable that incorporates the pressure signals from all sensors. To do this, it is necessary to approximate the aerodynamic pressure force vector based on a set of pressure transducer measurements.

For typical aerodynamic applications, an airfoil's efficiency is measured by the lift-to-drag ratio L/D that is achieved during operation. Ideally, this research aims to develop a performance function that may be used to optimize L/D, allowing for dynamic flow conditions that are unknown *a priori*. To perform optimal control of separation over an airfoil, it is desirable to attain a performance function that has its minimum where L/D, or equivalently the ratio of normalized quantities C_L/C_D, is optimized. Additionally, this mininmum should be unique in parameter space in order to avoid convergence to a local minimum. The equations that describe the pressure contribution to the lift and drag coefficients,

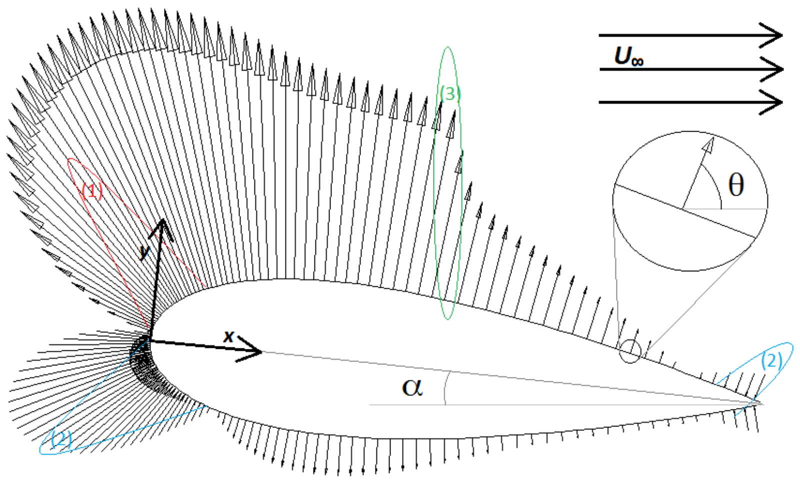

Figure 5.4: XFOIL Simulation of NACA 0025, 6 degrees, Re = 100,000.

$$C_L = \frac{2\oint p\sin(\theta)dA}{\rho {U_\infty}^2 bc} \tag{5.11}$$

and

$$C_D = \frac{2\oint p\cos(\theta)dA}{\rho {U_\infty}^2 bc}, \tag{5.12}$$

involve pressure integrals over the airfoil surface, which are not directly evaluated in experiments because the integral requires unrealistic sensor resolution. Let θ, illustrated in Fig. 5.4, represent the angle between the airfoil's local surface normal and the free stream velocity. Useful normalization to to the lift and drag coefficients is achieved by dividing the force quantities by a characteristic force quantity, $\frac{1}{2}\rho {U_\infty}^2 bc$, where ρ is the flow density, U_∞ is the free stream velocity, b is the span, and c is the chord length. As long as we can show that the pressure distribution being integrated is well-behaved, it is more practical to approximate these integrals with their corresponding summations using a discrete number of sensors. This approximation is the basis of the lift based performance function presented in this paper.

Figure 5.4 is a pressure distribution for turbulent flow that was obtained computationally using a numerical panel method that accounts for viscosity for the transitional range Reynolds number 10^5. The simulation assumed incompressible flow and thus applied low Mach number flow dynamics. By physical intuition, one observes three features of the pressure distribution, labeled in Fig. 5.4: (1) negative pressure gradient due to

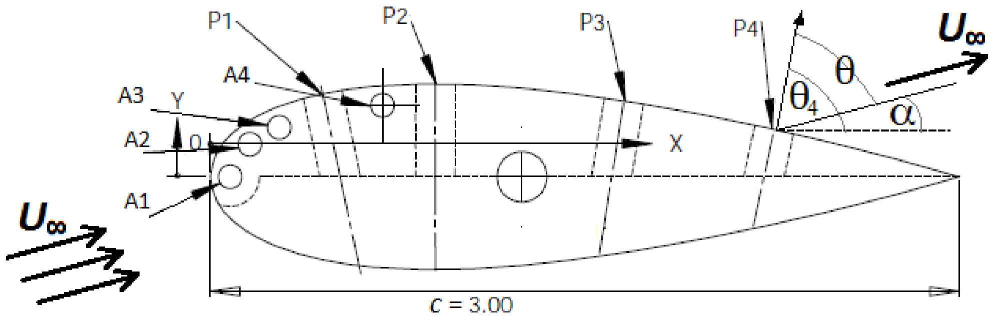

Figure 5.5: Airfoil Microjet Array and Pressure Transducer Schematic.

the acceleration caused by the impeded flow, (2) locally maximum positive pressure locations corresponding to the two stagnation points (fore and aft), and (3) apparent discontinuity on the top surface, indicating early stages of flow separation at the rear of the airfoil. Inspecting this and many other pressure distribution plots has led to some key observations. First, the surface pressure will never exceed the free stream stagnation pressure; this bounds the pressure distribution from above. Additionally, the surface pressure will be bounded from below by the solution of the potential flow (inviscid case, $Re \to \infty$), which can be solved analytically by using a conformal mapping. Lastly, the gradient $\frac{\partial p}{\partial x}$ is bounded as long as we consider incompressible Mach numbers (no shocks). Furthermore, the separation point and the high turning angles at the leading edge produce the largest gradients along the chord.

As a result of these observations, it is hypothesized that a limited number of discrete pressure measurements can be used to compute an approximation of aerodynamic forces that is sufficiently accurate to use as a control feedback variable. The aerodynamic pressure force is by definition a path integral of the pressure normal vectors around the surface of the airfoil. As described in Eqs. (5.11) and (5.12), this vector can be decomposed into two components: lift, which is normal to the free stream, and drag, which is parallel to the free stream. Note that this is only one of the components comprising the total drag force since shear force must also be accounted for. It is assumed that pressure data alone will provide a sufficient estimation for separation control purposes. This assumption is justified by the data presented in Appendix E, which indicates that points of maximal lift and points of maximal L/D are coincident for transitional Reynolds numbers.

An approximation of lift that is suitable for control purposes must practically preserve the global maximum of the actual lift quantity. The design of Fig. 5.14 is based on the hypothesis that four pressure sensors (marked P1 through P4) provide sufficient resolution to preserve the global maximum. An additional desired trait of a lift based performance function is that the function is positive definite about the optimal (design) point in flow condition space and that in its time derivative, it satisfies the negative definite condition of a Lyapunov function. This behavior is important because it permits control of a nonlinear system to converge to the optimal point while operating over a range of conditions.

Proposed here is a performance function along with validating results from both simulation and experimental data. Using four pressure sensors located along the airfoil center chord, a lift approximation is obtained in the following manner: take a weighted average of the calibrated pressure signals using $\sin(\theta)$ at each transducer location as a weighting function. Note that θ, the normal angle relative to the freestream, depends on both airfoil geometry and angle of attack. For this formulation, we assume that airfoil geometry angle (denoted θ_i relative to the chord axis) is known but angle of attack (α) is unknown, as this parameter would change during typical operation. The sine function in the lift integral (5.11) has argument $\theta = \theta_i - \alpha$. We assume a constant value for α, which introduces a tolerable error to the summation weights. Since flow separation is the phenomenon to be controlled, the 11.5° average separation angle (α_{sep}) for the NACA 0025 is a reasonable choice for the constant angle of attack parameter. For the range of angles of attack considered in this study ($\alpha \in [0^\circ\ 16^\circ]$) the error induced may be evaluated directly by comparing $\sin(\theta_i - \alpha)$ with $\sin(\theta_i - \alpha_{sep})$ for each of the four sensors. This calculation has been performed and in Fig. 5.6 is expressed as percent error for the computed weight of each sensor.

For the assumed range of flight conditions, Fig. 5.6 reveals we may ignore variations in the angle of attack when evaluating these weights with a penalty in accuracy of less than 7%. More importantly, the airfoil geometry component, which is known *a priori*, captures what an intuitive physical understanding of the problem would suggest: pressure sensors toward the leading edge, which are more vertically oriented, will provide more information about lift and less information about drag. Conversely, the rear sensors have a greater lateral component and therefore give a better indication of pressure drag than do their upstream counterparts. When evaluating the performance function, only the lift approximation is used because the drag approximation is subject to higher uncertainty and the changes in the lift coefficient alone are a good indicator of separation effects. Although only lift is accounted for in the design of the performance function, comparisons to the full L/D quantity have been made in validation, and the performance function approximates the shapes of these curves adequately well (see plots in Appendix E). XFOIL simulation results confirm that there is little to no difference in the optimal lift point and the optimal L/D point in each angle

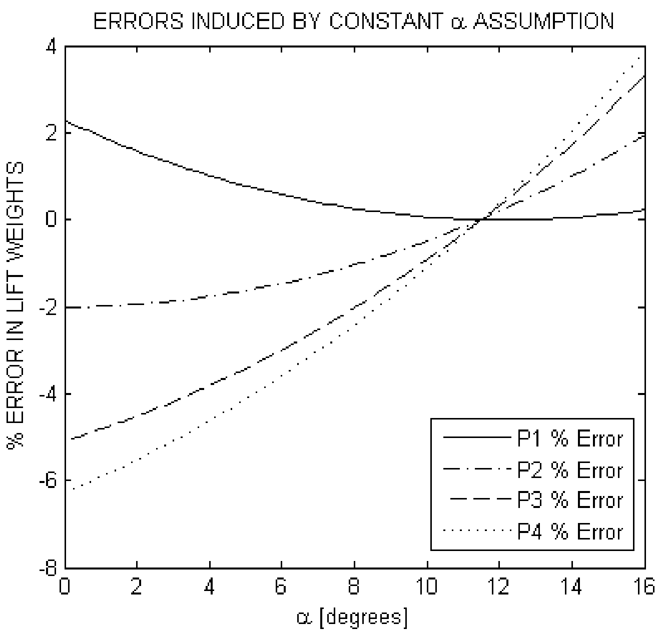

Figure 5.6: Percent errors when angle approximation $\alpha = \alpha_{sep}$ is used.

of attack series. The Lift-Approximating Function, Z_{lift}, and the Lift Based Performance Function, V_{lift}, may be computed as

$$Z_{lift} = \sum_{i=1}^{N} w_i \sin(\theta_i - \alpha_{sep}) p_i, \tag{5.13}$$

$$V_{lift} = (L_{max} - Z_{lift})^2, \tag{5.14}$$

where weights w_i appear in the summation to approximate the integral using N trapezoidal regions based on the pressures measured at each sensor p_i.

5.3.1 Lift Based Performance Function Validation Results

The results of the XFOIL analysis as well as some experimental validation are presented in this section. The XFOIL program solves viscous flow around an airfoil using an iterative panel method and turbulence modeling. The program is mainly used for optimal airfoil design because it produces high-fidelity lift and drag predictions. Experimental data has also been used to further validate the analytically derived performance function.

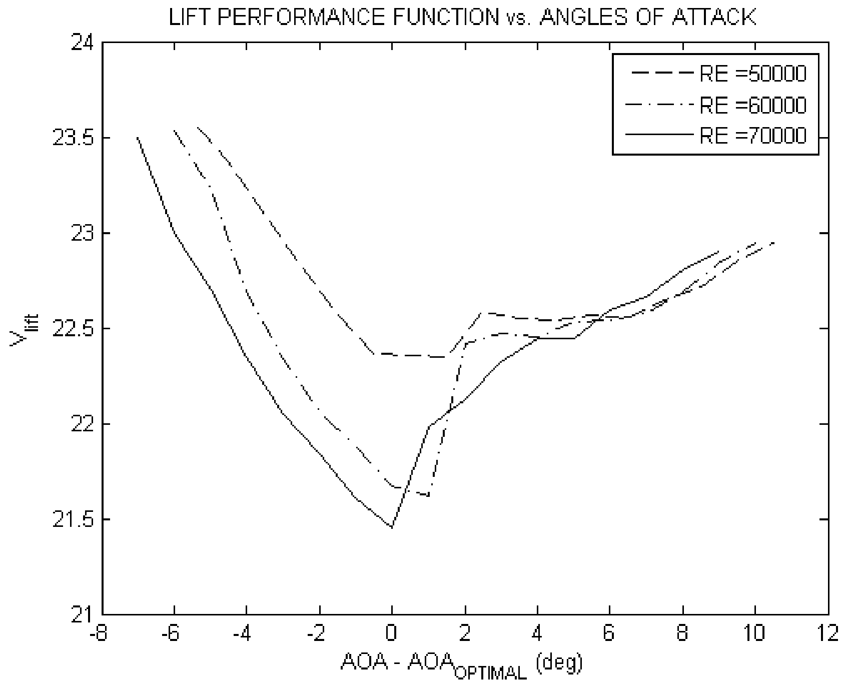

Figure 5.7: V_{lift} for lower Reynolds numbers, evaluated from simualated pressures.

Simulation Results. To evaluate the performance function in simulation, XFOIL viscous simulations have been run for each combination of *eleven Reynolds numbers* and *each integer angle of attack* from 0° to 16°. From these simulations, the 4 surface pressure values at the respective pressure transducer locations were the only information extracted from the simulation used to compute V_{lift}.

Figures 5.7, 5.8, and 5.9 present the evaluated performance function on the vertical axis and shifted angle of attack on the horizontal axis. The angle of attack is shifted to represent the difference, in degrees, from the point of maximum L/D ratio. (These optimal angles come from L/D peaks in plots such as in Fig 5.10.) Ideally, every curve should have it's minimum at $\alpha - \alpha_{optimal} = 0$, and for the transitional Reynolds numbers (80,000 through 120,000), this is the case. From the simulation data it can be seen that this behavior breaks down for Reynolds numbers outside of this range; however, it should be noted that for the higher Reynolds number off-design cases, V_{lift} tends to behave conservatively, favoring lower angles of attack. This means that even for Reynolds numbers outside of the transitional range, the control system, although giving up some optimality due to conservatism, should drive the system to the attached region as opposed to the separated region.

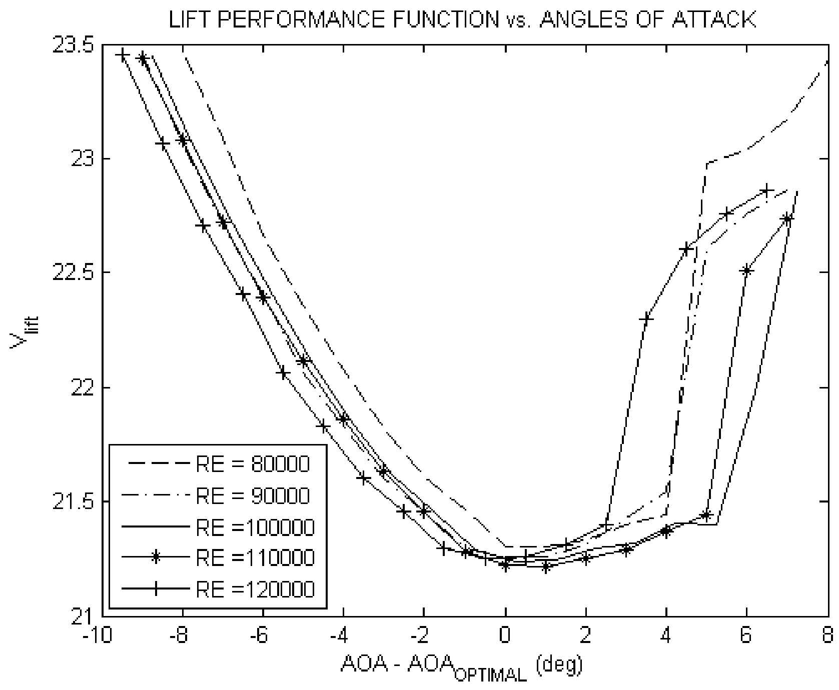

Figure 5.8: V_{lift} for transitional Reynolds numbers, evaluated from simualated pressures.

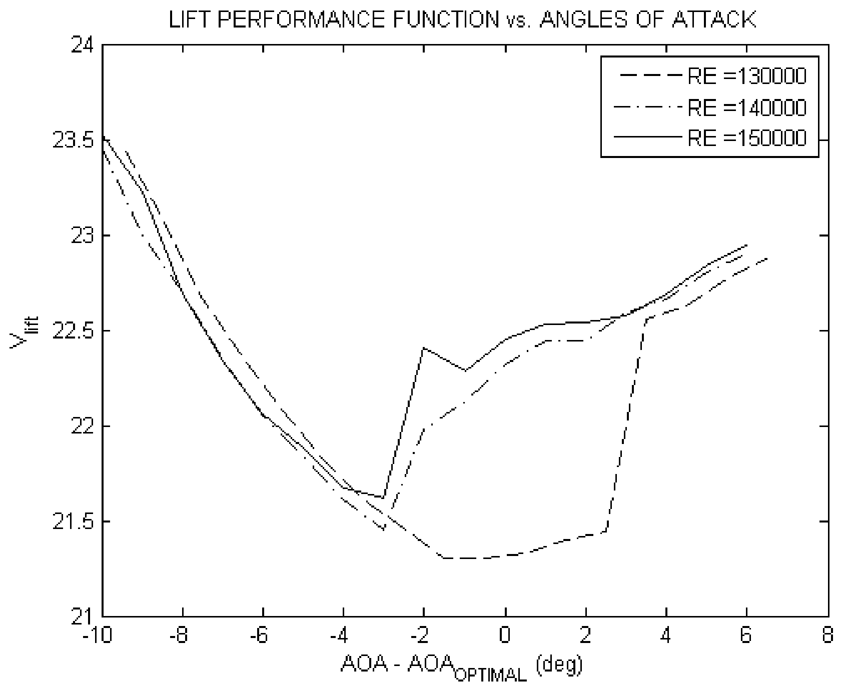

Figure 5.9: V_{lift} for higher Reynolds numbers, evaluated from simualated pressures.

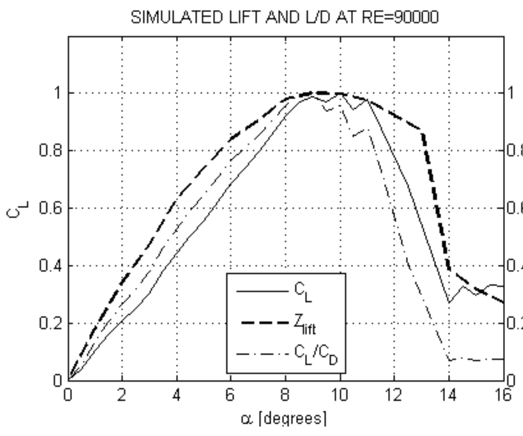

(a)

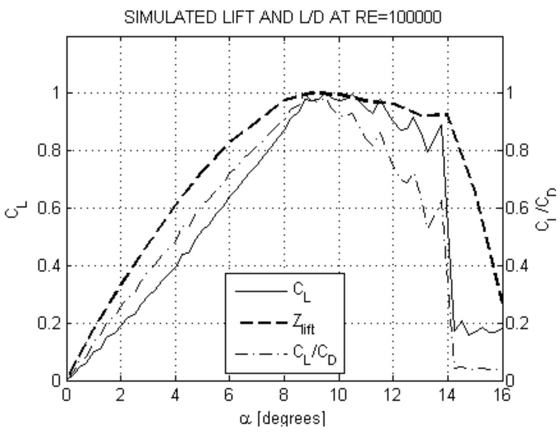

(b)

Figure 5.10: Lift Coefficient and L/D for $Re = 90000$ (a) and $Re = 100000$ (b).

Experimental Results. Lift and drag force measurement tests were performed in a subsonic, closed return, wind tunnel with a 12" x 12" test section on a NACA 0025 airfoil. The wind tunnel velocity corresponds to a Reynolds number of 1.0×10^5. The airfoil is designed to be modular so that multiple arrays of microjets can be utilized as well as multiple arrays of pressure sensors. Multiple airfoils are built allowing for tests to be performed with and without the use of Endevco unsteady pressure transducers. The stationary angle of attack can be modified by changing out the bottom cover of the airfoil. Currently, bottom covers have been manufactured for 0°, 2°, 4°, 6°, 8°, 9°, 10°, 11°, 12°, 13°, 14°, 15°, 16°, 18°, 20°, and 22°; therefore, up to this point force measurements using this configuration are attainable only at this resolution. These angles were selected to allow lift and drag readings to be recorded over a large span of angles, while allowing for a better understanding of baseline flow as well as a higher level of accuracy in determining where flow is separating. It is assumed that flow will separate around $11° - 12°$ angle of attack.

Lift tests were completed in this experimental configuration, and for comparison purposes, pressure transducers were installed on a separate NACA 0025 airfoil in each of the four design locations (p1-p4 location shown in Fig. 5.14). A CAD illustration of the tunnel model with installed pressure transducers is given in Fig. 5.11. After calibrating the pressure transducers, the experimental pressure signals were given as inputs to the same function for Z_{lift} that was used in the simulation tests. Figure 5.12 shows the lift measurements compared with the performance function evaluated for three trials of experimental data. In this experiment, total flow separation occured between 14° and 15°. The predictions made by the lift performance function match very well when compared to the measured lift values, capturing the over trend

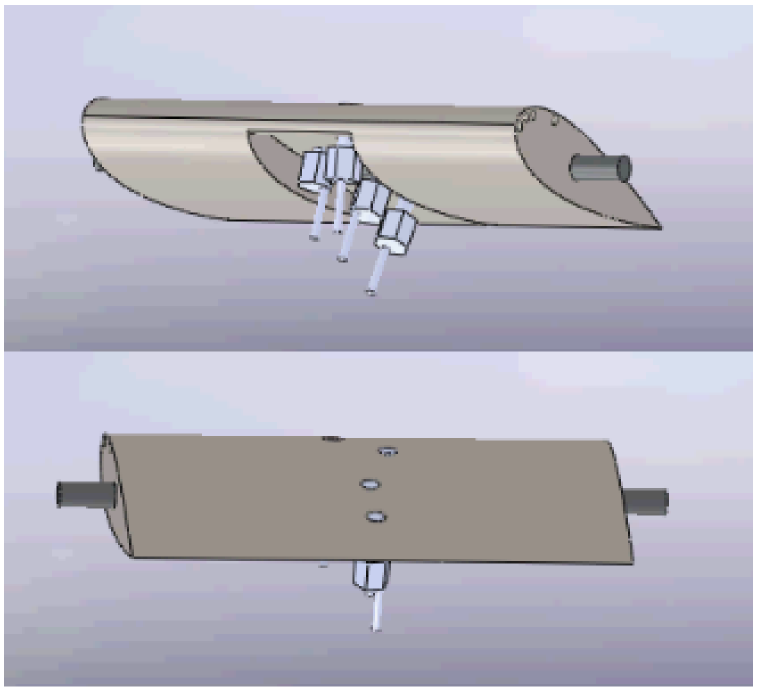

Figure 5.11: Assembled Airfoil CAD with Pressure Transducers

of increasing lift and the drop caused by the separation event. For the sake of comparison, the p_{rms} plot for a single sensor is given in Fig. 5.13 (p_4 gave the best results for this Reynolds number). Although this more traditional performance function distinguishes between separated and attached regimes, the presence of local maxima may lead to convergence to a local minimum of L/D.

Ideally, the experimental data plot (Re of approximately 95,000) should closely match the shape of the simulated data plots of Fig. 5.10. The difference between simulation and laboratory results is primarily due to the unpredictable nature of the transition in the boundary layer from laminar to turbulent flow. While the simulation evaluates the flow based on a turbulence model, the precise location at which a particular flow will transition is highly sensitive to surface roughness and is difficult to predict. In addition to the transition point uncertainty, the wind tunnel fan apparatus introduces turbulence that has not been accounted for in the simulated data. For this reason, the Reynolds number of the tunnel experiment is effectively higher than the computed value 95,000. The separation location observed in experiment is closer to the angle observed in the Re=110,000 simulation than either of the Re=90,000 or Re=100,000 simulations. Even though these difficulties exist in matching experimental flow separation to simulated flow separation, the performance function, based only on steady pressures, is able to make good estimates for both sets of data.

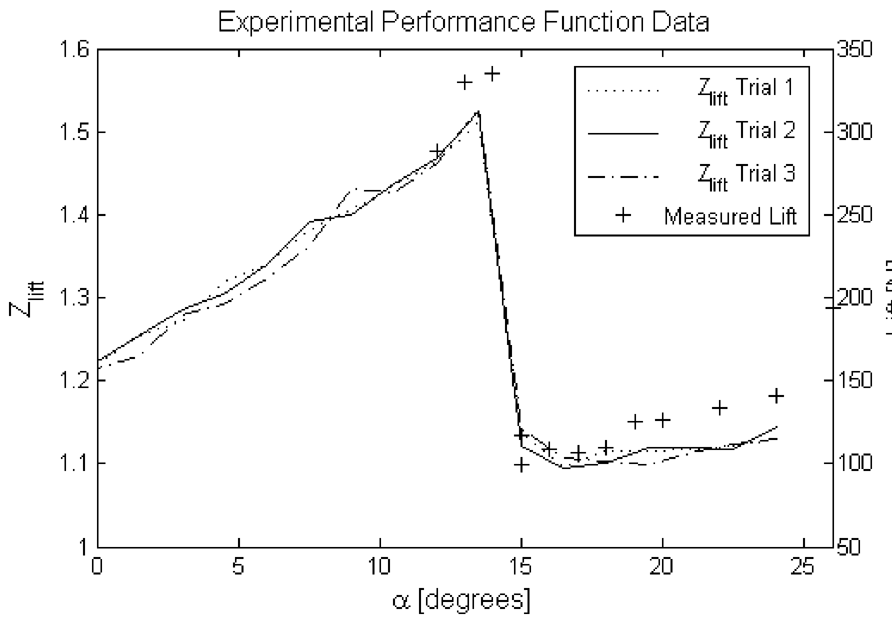

Figure 5.12: Z_{lift} evaluated with measured pressures compared to measured lift for Re=95,000.

5.4 Experiments and Results

Results are presented for wind tunnel experiments with the goal of mitigating separation and therefore controlling lift. This section contains a description of the experimental setup in Subsection 5.4.1, results of open-loop characterization tests in Subsection 5.4.3 and results of closed-loop control in Subsection 5.4.4.

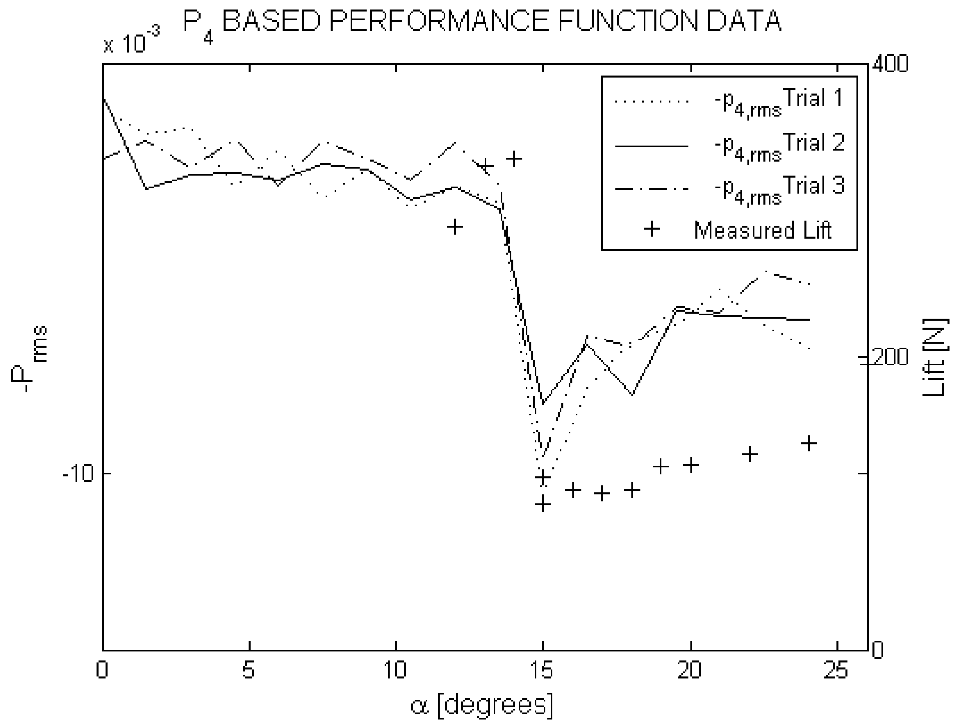

Figure 5.13: Measured lift and negative p_{rms} evaluated with a single measured pressure signal for Re=95,000.

5.4.1 Flow Control Experimental Setup

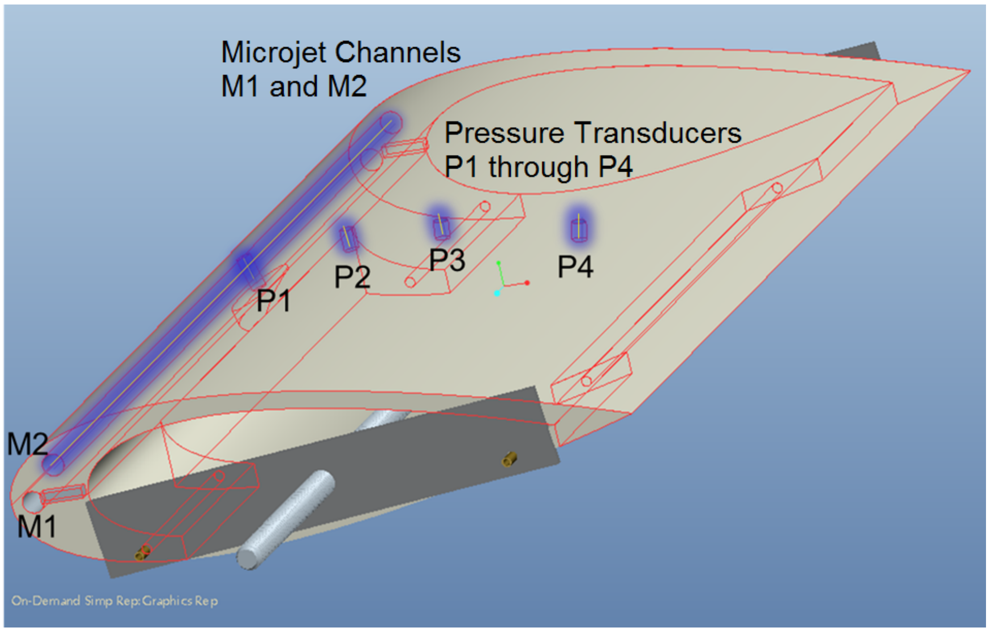

Figure 5.14: Airfoil Schematic. This diagram includes the locations of microjet array M1 and M2 and pressure transducers P1 though P4.

The wind tunnel experiments were carried out in the subsonic closed loop wind tunnel at the FAMU-FSU College of Engineering. This wind tunnel has a 12 inch x 12 inch square test section and is capable of air flow speeds from 3.5 m/s to 35 m/s. The NACA 0025 airfoil model of Fig. 5.14 is used in the following tests and is mounted to allow a variable pitch angle. Sensor and actuator placement is given in Table 5.1, and chord and span dimensions are given in Table C.2 of Appendix C. At each pressure transducer location, P1 through P4, an Endevco unsteady pressure transducer (model 8510B, 1 psi) was mounted flush with the airfoil surface along the center chord. At each microjet location, M1 and M2, an array of 40 equally-spaced microjets were drilled into the channel, normal to the airfoil surface. Each microjet channel was supplied from both ends by plastic tubing to the output end of a solenoid valve (SensorTechnics HF Pro). The input end of the solenoid valve was attached to a steady pressure source supply between 0.5 psig and 10 psig. In each experiment, angle of attack was measured by taking a side view photograph and comparing pixel coordinates of the support pins to pixel coordinates of points on the tunnel wall.

During tests, data signals from the four pressure transducers were amplified using a Hendrick & Associates multichannel amplifier and acquired digitally using dSPACE hardware. The command signals to

Table 5.1: Chord Locations of Microjet exits and Transducers.

Component	M1	M2	P1	P2	P3	P4
x/c	0.0	0.063	0.127	0.300	0.452	0.667

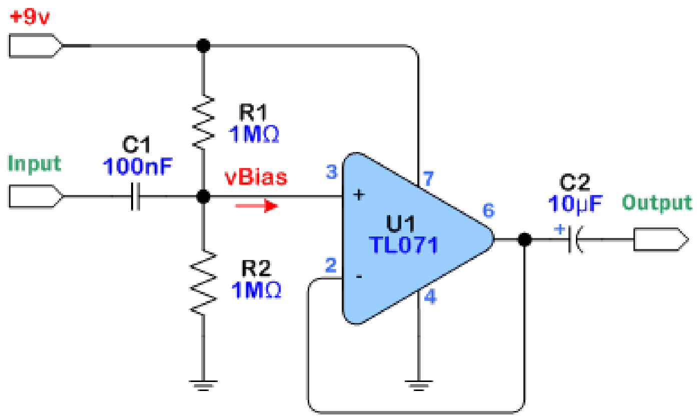

Figure 5.15: Buffer Circuit Diagram . The buffer circuit amplifies an input voltage signal so that the output voltage has sufficient current to drive the solenoid valves.

pressure transducers were sent from dSPACE and amplified using the op-amp buffer circuit of Fig. 5.4.1. In open and closed loop testing, the single-input cases used only microjet array M2, and the two-input cases used both arrays M1 and M2, supplied independently by two solenoid valves.

5.4.2 Particle Image Velocimetry

Two-Component Particle Image Velocimetry (PIV) was used in order to quantitatively examine the flow field and provide evidence of reattachment of the separated flow. Because surface mounted unsteady pressure sensors were in operation during PIV acquisition, a seeding fluid which left little to no residue on the sensors was needed. For this application, Di-Ethyl-Hexyl-Sebacat (DEHS) was used with a Laskin type seeder; nominal particle diameter was ~ 1 μm. A 200 mJ, pulsed, Quantel® Nd:YAG laser illumined the seeded flow field of interest on the suction side of the airfoil. The laser sheet was formed by passing the beam through LaVision sheet forming optics and expanded by a cylindrical lens; the optics were adjusted to achieve a laser sheet thickness of ~ 1 mm throughout the measurement domain. The spanwise location of the laser sheet was approximately at the airfoil centerline. Due to the unsteady pressure sensors installed at

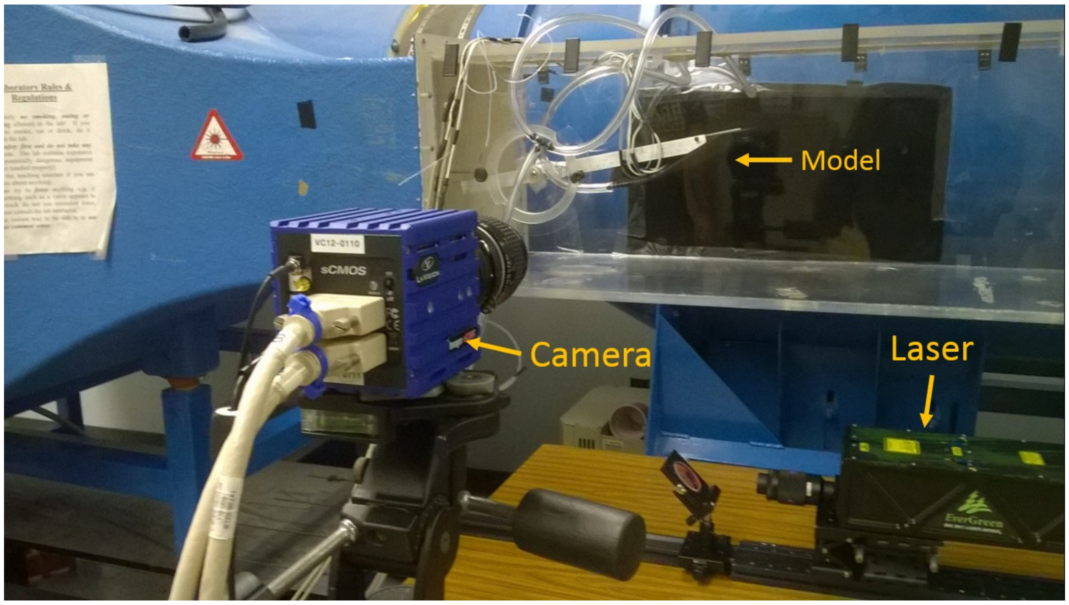

Figure 5.16: PIV Experiment Photograph. The PIV setup takes snapshot images of illuminated smoke particles. Processing the images yields velocity field measurements. The laser and optical hardware are configured to illuminate only the smoke particles in the desired plane.

the airfoil's true centerline, the laser sheet was offset by one pressure sensor diameter ($\sim$3 mm) in order to minimize reflections. The PIV configuration is shown in Fig. 5.16.

Images were acquired at a rate of 15 Hz with a 5.5 megapixel sCMOS camera equipped with a 55 mm lens. Each PIV case consisted of the ensemble average of 1,000 instantaneous image pairs in order to adequately estimate mean and turbulent statistics of interest. Images were processed using LaVision's DaVis 8.2 software. Velocity fields were correlated using a multipass algorithm with a final interrogation window size of 32 x 32 with a 75% overlap. The resulting velocity field spatial resolution is $\sim$ 0.9 mm x 0.9 mm.

5.4.3 Open-Loop Characterization

Open loop characterization of the flow separation control system relied on a frequency sweep input. The supply voltage was a 50% duty cycle square wave of increasing frequency. After conducting tests using a steady supply pressure, the frequency was increased from 0 Hz to 300 Hz in 6 Hz increments, and 3 seconds of data was taken at each frequency. Measurements consisted of signals from pressure transducers located at the microjet channel (at the edge of the airfoil span) and at the microjet exit (2mm from the jet exit at the center of the airfoil span). For each input frequency, the time domain response was analyzed using phased

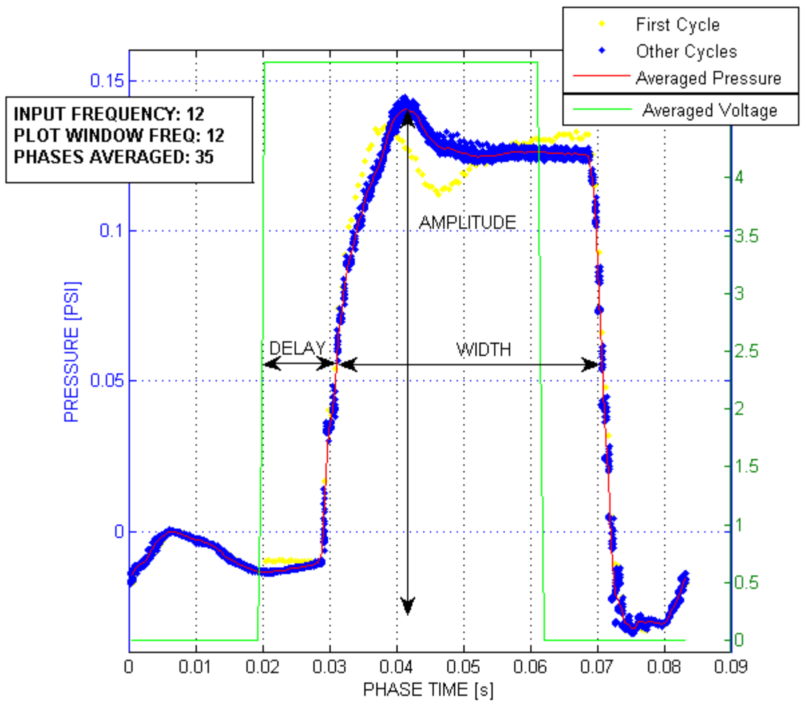

Figure 5.17: Time Domain Channel Pressures during Pulsed Actuation. The phase-averaged response of the actuator to a 12 Hz square wave is plotted. The width and delay computations are calculated at half of the maximum height of the waveform.

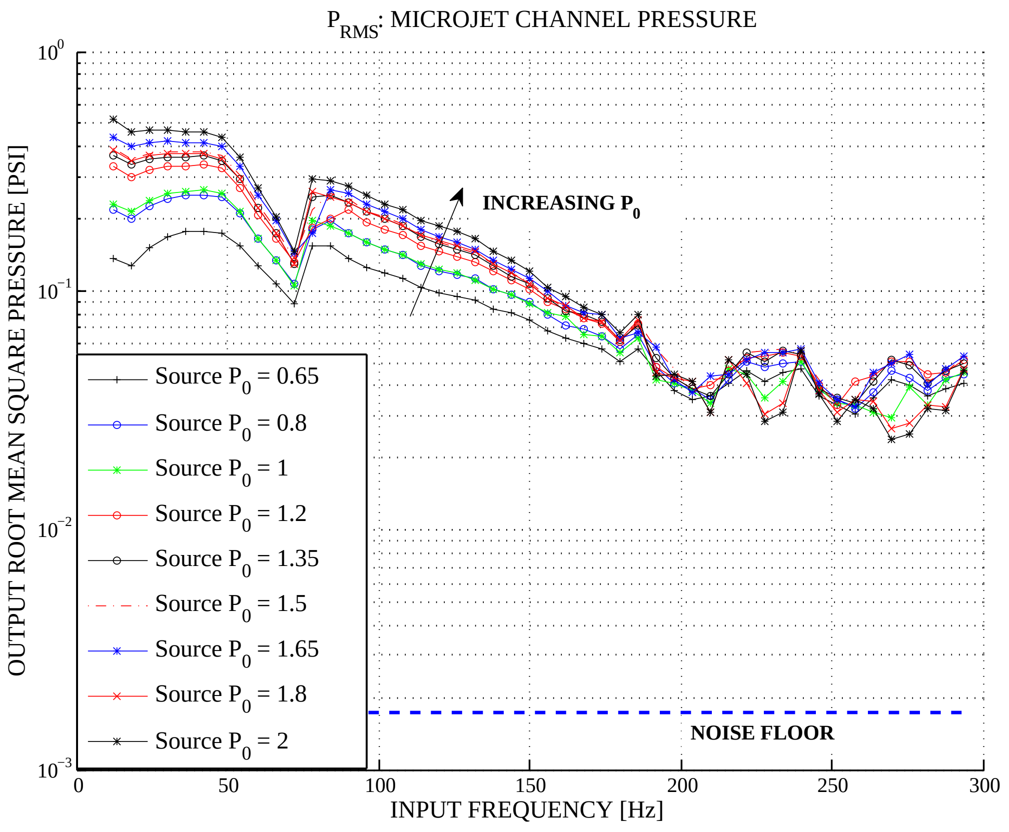

Figure 5.18: Frequency Domain Channel Pressures during Pulsed Actuation. The response of the actuator to frequency inputs is plotted.This plot displays the response measured at the microjet channel for several different source pressures P_0.

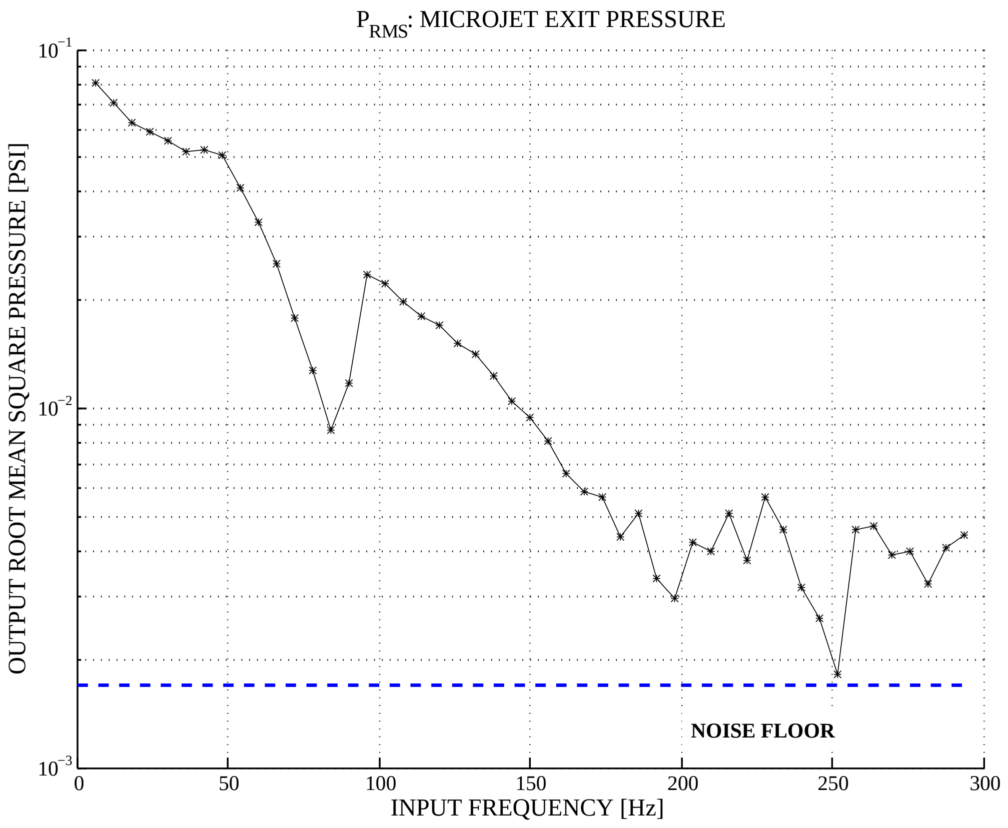

Figure 5.19: Exit Pressures during Pulsed Actuation. The pressures measured at the microjet exit display a similar trend to those measured within the channel; however, because of the low signal-to-noise ratio, the data for a 10 PSI source pressure is plotted.

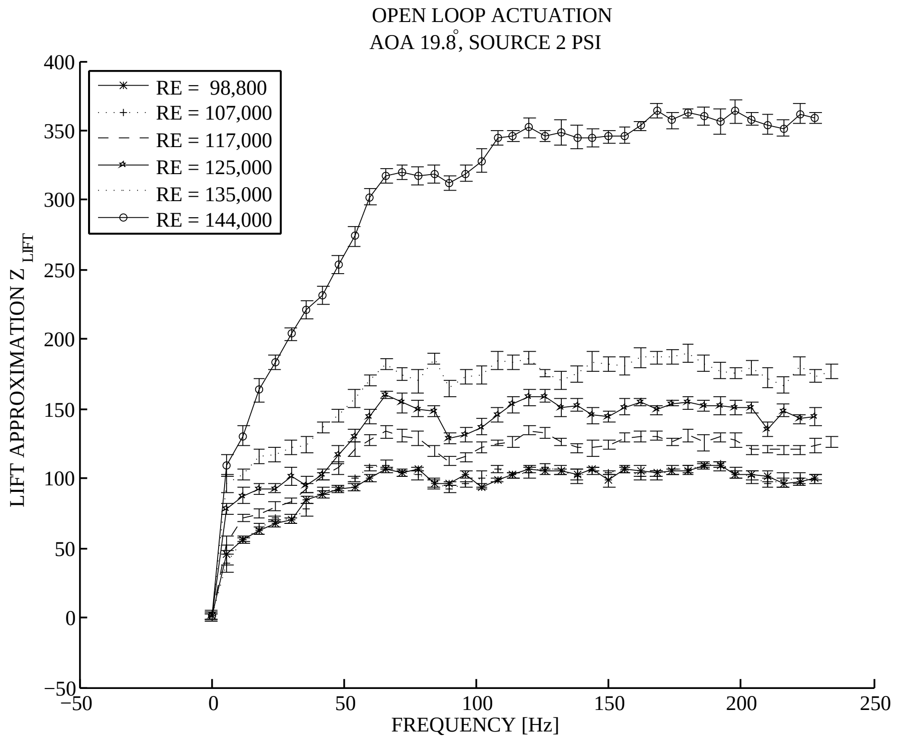

Figure 5.20: Z_{lift} Response to Frequency Actuation at AOA = 19.8°. For various flow conditions, the majority of the lift improvement occurs from 0 to 80 Hz. This is consistent with findings from bandwidth tests, which indicated that 80 Hz was the highest frequency to which the valves are capable of responding.

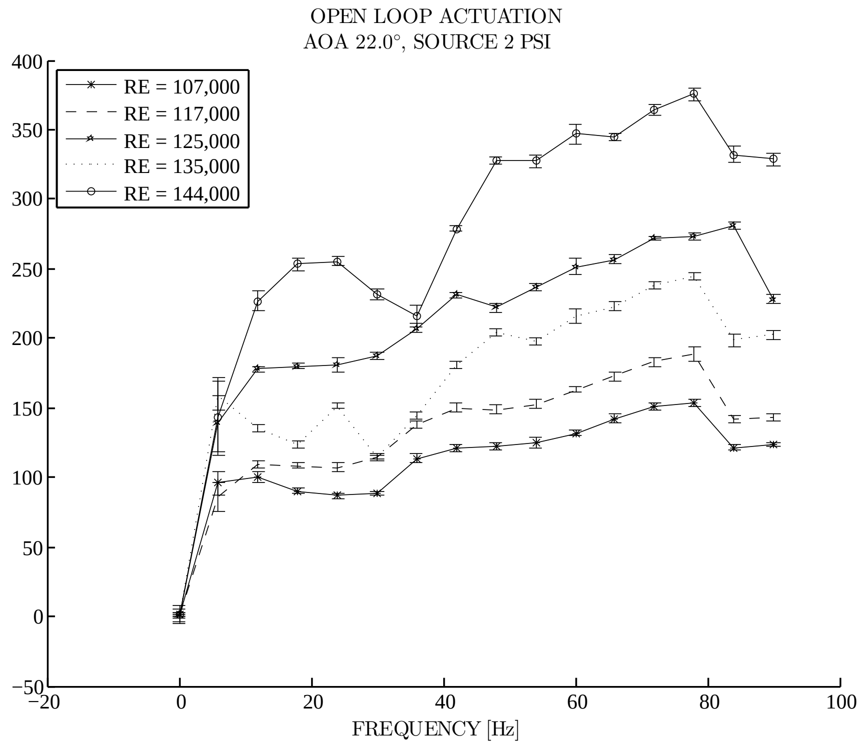

Figure 5.21: Z_{lift} response to frequency actuation at AOA = 22.0°. Open loop results at a different angle of attack indicate a clearly nonlinear relationship between input frequency and Z_{lift}.

averaged data, such as the data plotted in Fig. 5.17 for the data collected during 12 Hz excitation. From these phase averaged curves, the amplitude, width, and time delay between voltage excitation and pressure response were calculated, as displayed in the figure. The delay and width of the waveform were computed at 50

The data was sampled at 2 kHz, and time and frequency domain analysis was performed on these measurements. From 0 to approximately 80 Hz, the pressure output frequency is identical to the voltage excitation frequency. Above 80 Hz, mode switching occurs due to the dynamics of the solenoid valve. The valve, which is designed for 30 Hz operation, switches primarily between the input frequency and $\frac{1}{2}$ of the input frequency.

Microjet exit pressure data is plotted in Fig. 5.19. In order to attain reasonable signal-to-noise ratio (SNR) at the jet exit, the source pressure was increased to 10 psi. The pressure data collected at the microjet exit (Fig. 5.19(b)) displayed similar trends to the data collected at the microjet channel (Fig. 5.19(a)).

In addition to bench top characterization, the open loop response of the overall system was measured in the wind tunnel. The input for these tests was the solenoid valve voltage frequency, and the output was Z_{lift}, the lift based performance function computed from the transducer measurements at locations P1 through P4. This performance function, derived in prior research [62], uses the four pressure signals to approximate lift changes, weighting each sensor reading based on sensor spacing and airfoil geometry. For the NACA 0025 with sensors located as indicated in Table 5.1, Z_{lift} may be computed as

$$Z_{lift} = \sum_{i=1}^{N} w_i p_i, \tag{5.15}$$

with the weights w_i given in Table C.2 of Appendix C. In the state vector of Eq. (5.6), each $\mathbf{y}_k$ represents a Z_{lift} measurement, and each $\mathbf{u}_k$ represents a voltage frequency supplied to the solenoid valve for microjet channel M2. Changes in the command voltage frequency were observed to cause changes in the steady state value of Z_{lift}. After each 6 Hz frequency increment, data was collected after the system reached a steady state. The data is presented in Figs. 5.20 and 5.21. Evidence of an actual change in lift as Z_{lift} changes is given in the c_p plots of Fig. 5.22. These discrete c_p measurements suggest that the magnitude of the area under the curve increases when going from 0 Hz to 72 Hz, which corresponds to greater suction on the upper surface and higher lift. Further evidence includes observations of separation reduction indicated by alignment of tufts on the airfoil surface as well as the generation of significant moments that were able to rotate the airfoil setup when the microjets were actuated without the shaft clamped in place. Additionally, the

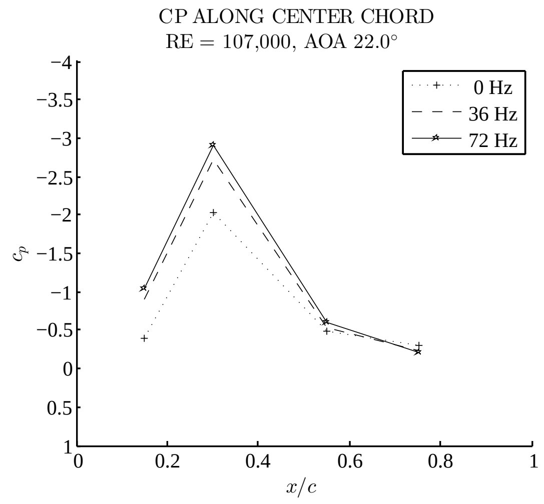

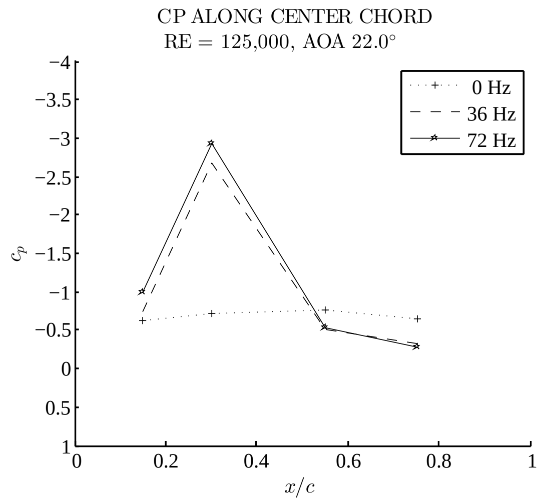

(a) (b) (c)

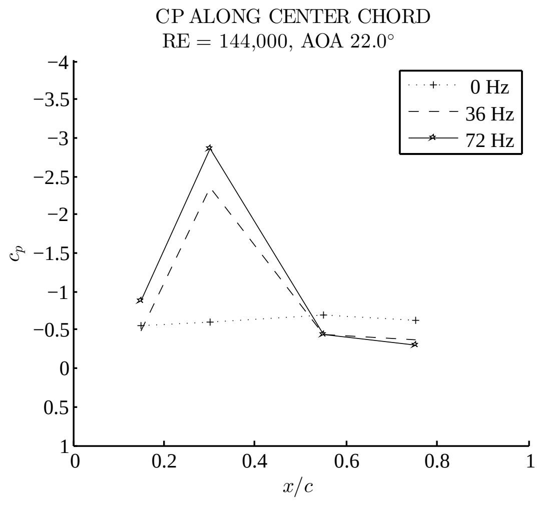

Figure 5.22: Measured c_p Values at Pressure Transducer Locations. The pressure transducers are positioned to resolve the suction peak, which grows in each case due to frequency actuation. Larger suction peaks generally correspond to increased overall lift.

PIV measurements that are included in the following section provide definitive evidence of the effectiveness of the microjet actuators to mitigate separation. Momentum coefficients c_μ in these experiments ranged from 0.33 (higher Reynolds number tests) to 0.5 (lower Reynolds number tests), since the typical microjet velocity was approximately 5 m/s.

5.4.4 Closed-Loop Control

Frequency sweeps as mentioned above were used to train the neural network and represent the input-output behavior of the system with a nonlinear model. Using a model initialized with sweep data, Adaptive SBMPC was applied to perform closed loop control. During the 30-second learning phase (not plotted), the identification algorithm was enabled, but the control algorithm was disabled. During the control phase, both the controller and identification were enabled and produced successful tracking of the desired reference value of Z_{lift}. In each experiment, the reference value was commanded manually, and the control system automatically made the input adjustements necessary to drive the measured Z_{lift} signal to match the desired reference signal. The tuning parameters selected for the identification and control algorithms are given respectively in Figures D.1 and D.3 of Appendix D. In the plots of Figs. 5.23 through 5.26, the Z_{lift} was normalized (divided by 100) to match the order of magnitude of the input space. This type of scaling is commonly applied [33] when using neural networks so that inverted matrices are numerically well-conditioned. Reference tracking capability is demonstrated for a variety of reference trajectories. Figs. 5.23 and 5.24 indicate with an arrow the time at which control was activated. In the subsequent figures, the controller is already active at time zero.

These results demonstrate the capability to not only maximize lift, but also control lift by commanding intermediate values. In Fig. 5.23, the commanded reference signal (dashed line) is constant, which means the control system was configured to increase and hold Z_{lift} constant. For this case, the momentum ratio c_μ of microjet momentum to free stream momentum is 0.4 and the Reynolds number is 125,000. The actual ouput signal (solid line) achieves the commanded increase-and-hold behavior. In Fig. 5.24, the commanded reference was manually stepped downwards, in order to demonstrate the ability of the control system to decrease Z_{lift} when desired. This test was also configured with AOA= 20°, RE= 125,000, and c_μ=0.4. Fig 5.25 displays similar results and includes both upward and downward stepwise motion, again with AOA= 20°, RE= 125,000, and c_μ=0.4. For the case shown in Fig 5.26, the neural network was trained at a Reynolds number of 125,000, but control is demonstrated for a Reynolds number of 150,000. In this test case, the momentum coefficient c_μ is 0.33. Some prediction error, indicated by the departure of the dotted line from the solid line, occurs around 13 seconds, but the error is corrected within 5 seconds. This demonstrates the robustness achieved by online system identification.

Fig. 5.27 shows the control adjustment in reaction of the control system to changes in Reynolds number during operation. The system adjusts the neural network model at the same time as the updated control signal is being computed and executed. When the Reynolds number decreases from 150,000 to 140,000, c_μ also changes from 0.33 to 0.36. The adaptation of the neural network model is vital when flow conditions change. In Fig. 5.27, the model adaptation is what allows the neural net prediction signal (dotted curve) to adjust to match the measured signal (solid curve) even when the flow conditions change. SBMPC is then responsible for modifying the control input signal so that the prediction signal matches the reference signal (dashed curve). Because of the closed loop control system, it was possible to take a scenario where the flow was controlled and attached, change the wind tunnel speed so that the flow separates, and observe the neural network adaptation and controller reaction as the flow is automatically reattached.

In order to verify that the changes in Z_{lift} actually correspond to a changing degree of separation in the flow, visualization experiments were performed to capture the velocity field surrounding the wing both with and without control enabled. In these experiments, the airfoil wind tunnel configuration was fixed to a particular angle of attack and tunnel velocity. The velocity field was then measured via PIV and averaged over a 1000-frame, 60-second window. For the purpose of visualization, the image processing results are displayed with a flipped y-axis so that the angle of attack is depicted as positive (the PIV experiments were performed with a negative angle of attack). The control system was then enabled to maximize Z_{lift}. The control system can be configured to maximize lift by prescribing a constant reference trajectory that is greater than the attainable range of Z_{lift} values. In this case, the reference for Z_{lift} was set to 0. A second series of PIV measurements of the same duration was collected to characterize the controlled flow. Contours of streamwise velocity are shown in Figs. 5.28 through 5.33, and display the uncontrolled and controlled flows for two different flow conditions (AOA 16°, Re 150,000, and 22°, Re 90,000, respectively) when the controller is set to maximize Z_{lift}. In these figures, the separated region is outlined by zero-velocity contours shown in black. In the cases of Figs. 5.28, 5.31, and 5.32, the separation bubble is greatly reduced in size and begins further downstream. The remaining cases of Figs. 5.28, 5.28, and 5.28 represent unsuccessful control cases, in which control at all available frequencies is ineffective. The main limitation on control authority of the microjet actuators is the valve bandwidth of 80 Hz. Higher frequency actuation would

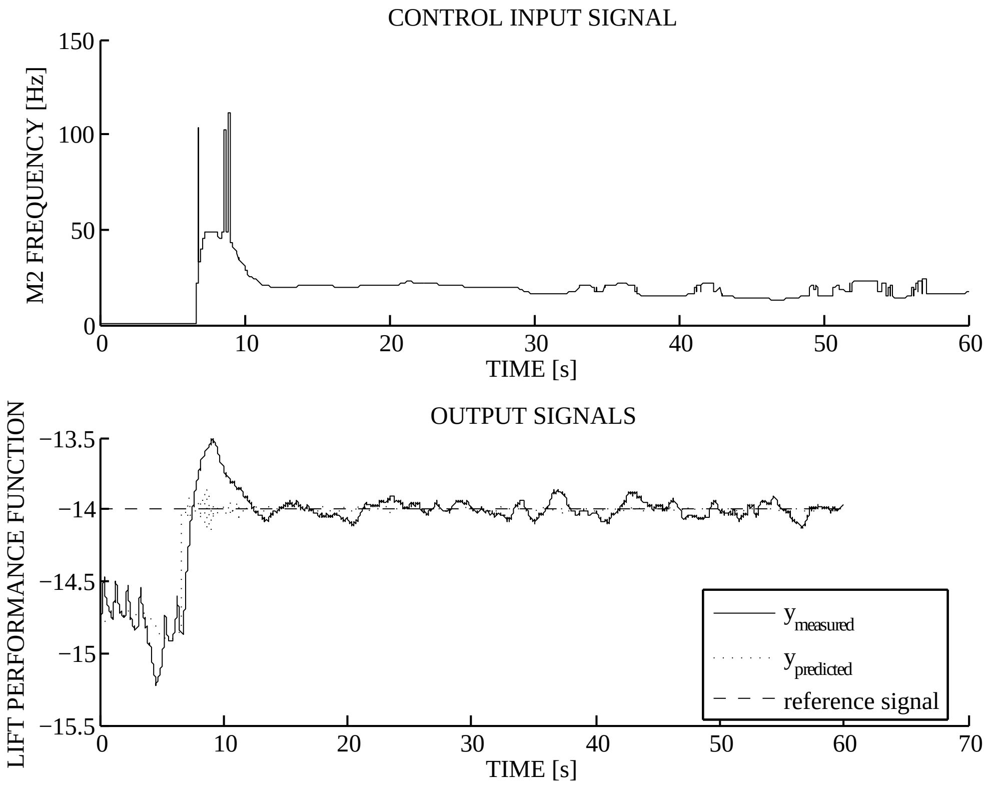

Figure 5.23: Closed Loop Case 1. The Reynolds number is 125,000, and the angle of attack is 20°. This closed loop case illustrates ability to follow a step reference signal subsequent to the activation of the SBMPC controller.

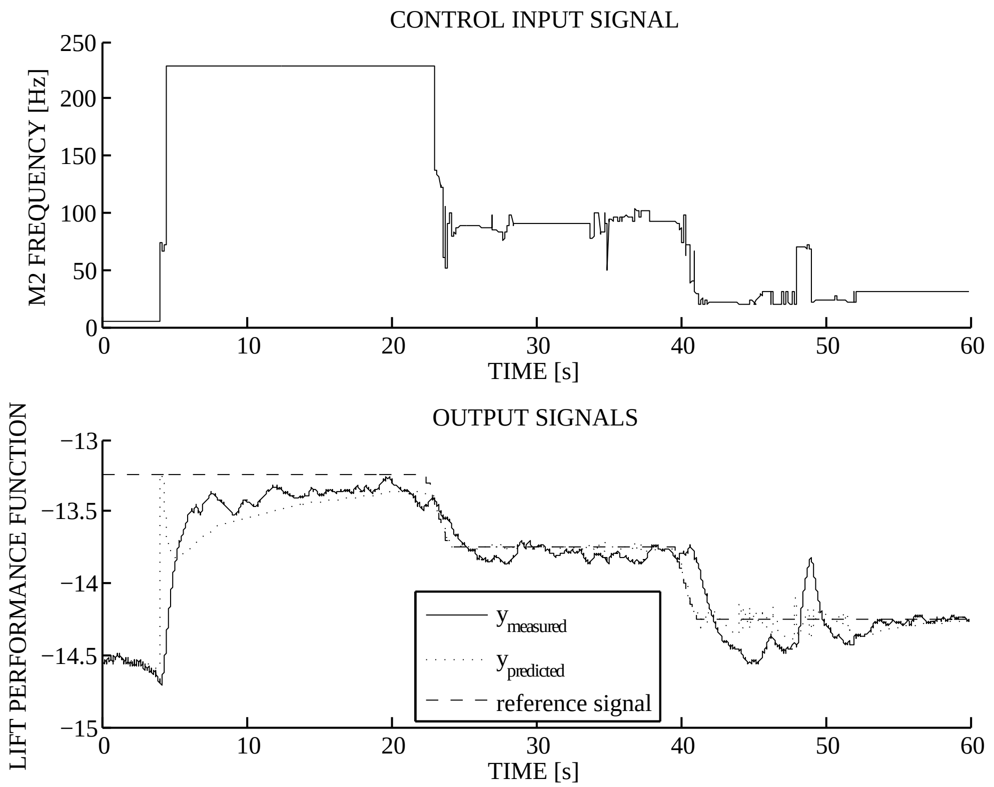

Figure 5.24: Closed Loop Case 2. The Reynolds number is 125,000, and the angle of attack is 20°. This closed loop case illustrates the ability to command intermediate vales of Z_{lift}.

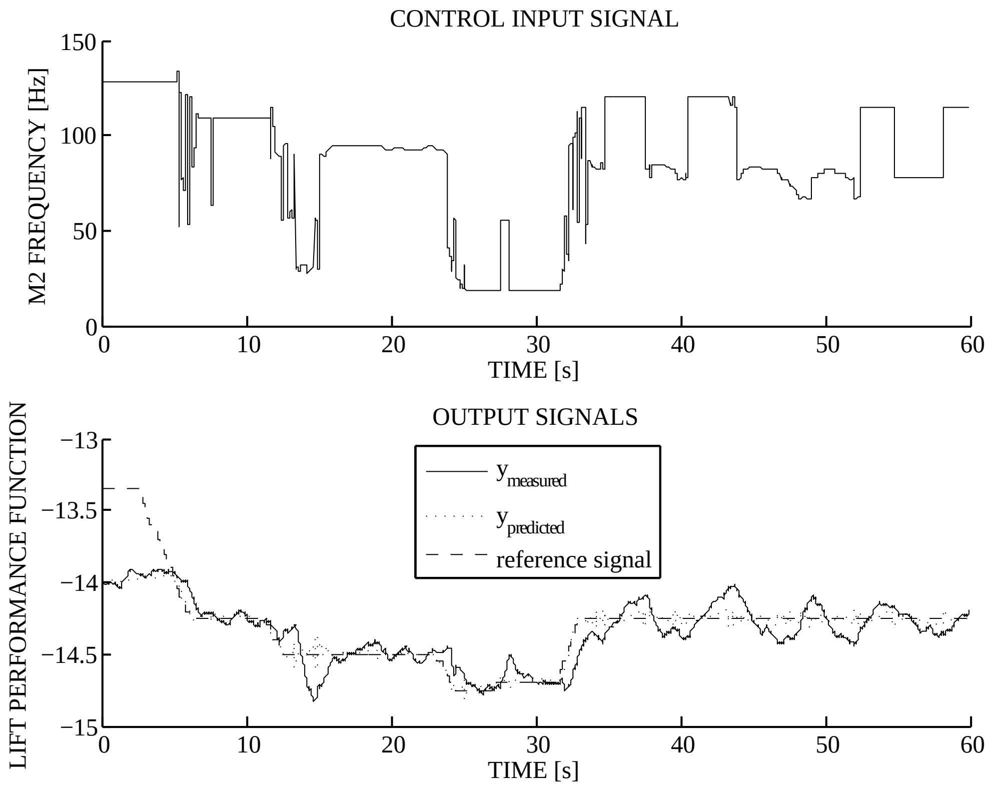

Figure 5.25: Closed Loop Case 3. The Reynolds number is 125,000, and the angle of attack is 20°. This closed loop case illustrates the saturation behavior of the controller: from time 0 to 5 seconds, Z_{lift} is simply maximized when the specified reference is above the attainable actuation range. Tracking resumes when the reference value is decreased to an attainable value.

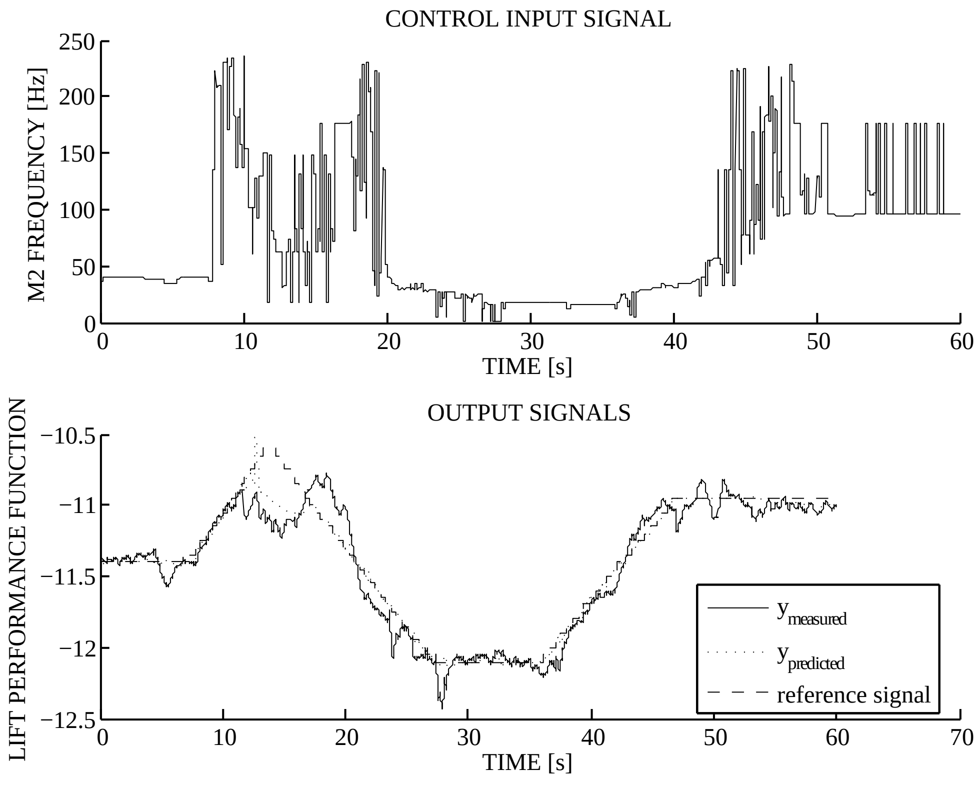

Figure 5.26: Closed Loop Case 4. The Reynolds number is 150,000, and the angle of attack is 20°. This closed loop case illustrates the ability to track ramp trajectories. During training, the tunnel Reynolds number was set to 125,000, ensuring that online model adaptation would be required when tested at a higher Reynolds number.

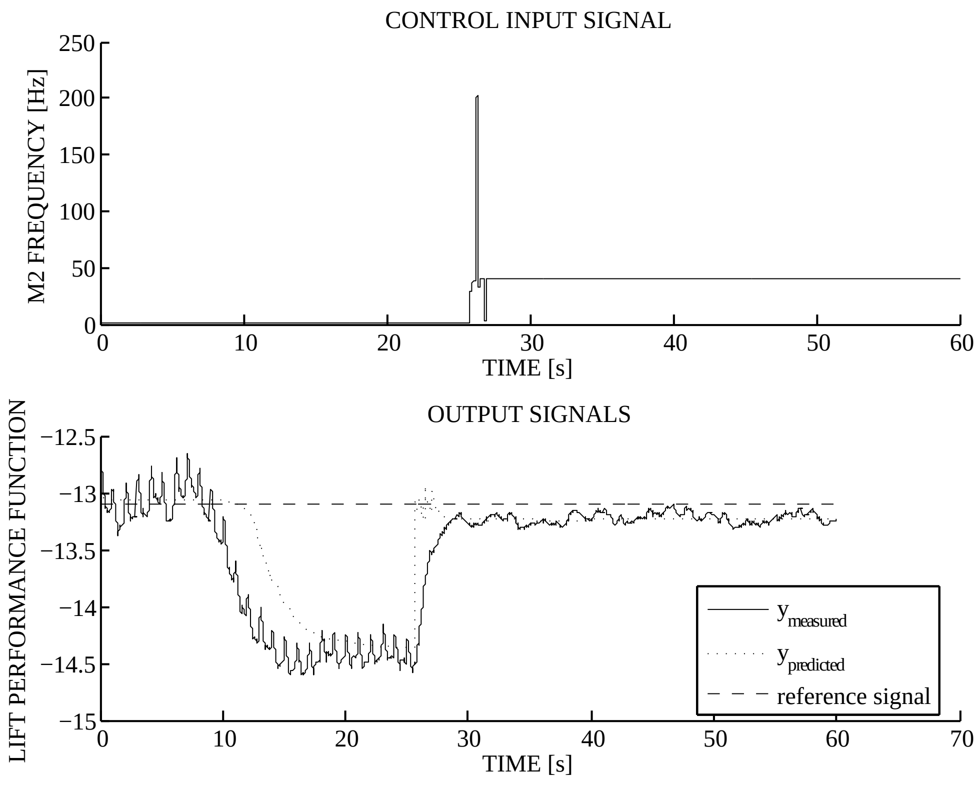

Figure 5.27: Closed Loop Case 5. The Reynolds number shifts from 150,000 to 140,000, and the angle of attack is 20°. This case demonstrates that the ability to adapt enables the control system to be robust to changes in the flow conditions.

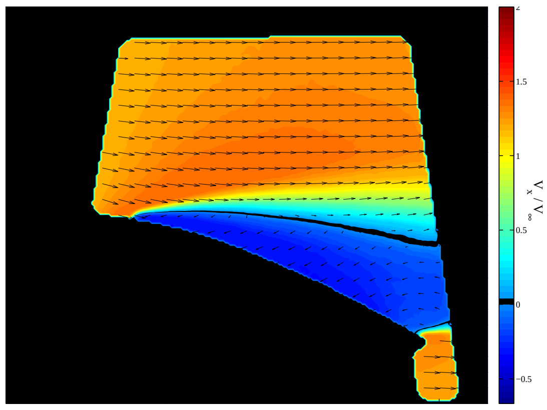

(a)

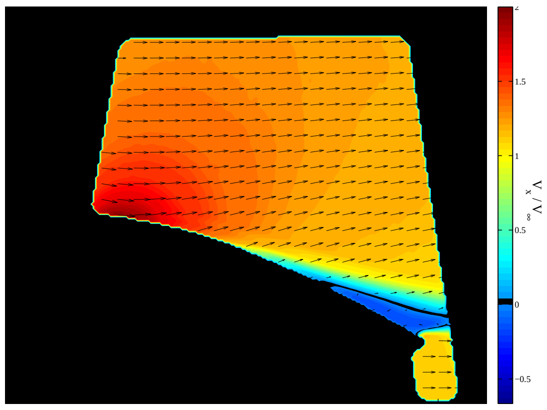

(b)

Figure 5.28: Baseline (a) and Controlled (b) V_x for 16°, 15 m/s. The baseline PIV data was collected with the control system off. In the controlled case, data was collected with the control system set to maximize Z_{lift}, and the tunnel speed corresponds to a Reynolds number of 150,000 based on chord length.

enable effective control for more more cases. For such cases, closed loop control can be utilized to conserve energy by turning the actuators off when control is ineffective.

5.5 Summary

Closed loop control of separated flows has been demonstrated using the Adaptive SBMPC control system. Quantitative results using a pressure-based lift approximation and PIV flow imaging indicate the effectiveness of the control system to control flow behavior based on a nonlinear neural network model constructed from data. This model is adjusted in real time to represent changes in flow conditions while the controller is in operation. The closed loop experiments demonstrated successful tracking of desired values of Z_{lift} by mitigating flow separation. The control system is able to increase or decrease lift in response to an external command, subject to the limitations of the actuator. Both the nonlinear input to output behavior of the system and the nonlinear control law are learned adaptively, so even when flow conditions were modified during a control experiment, the control system was successful in adjusting the inputs to meet the desired Z_{lift} value. To date, only a few selected cases have been visualized. Future tests will cover a wide range of flow conditions and will also incorporate multiple input-multiple output control by enabling both rows of microjets, M1 and M2. Further analysis and flow visualization tests will quantify the achieved lift gains and provide insight into the control authority of the microjet actuators and cost-benefit balance of the overall

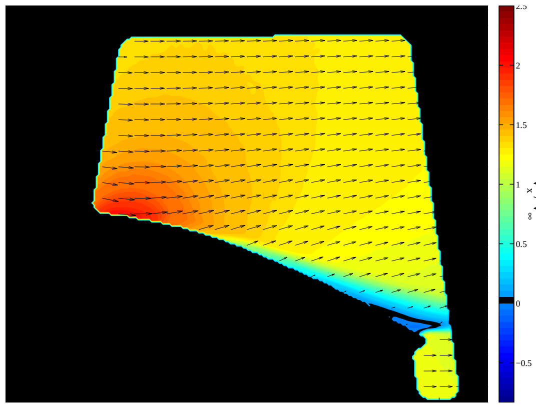

(a)

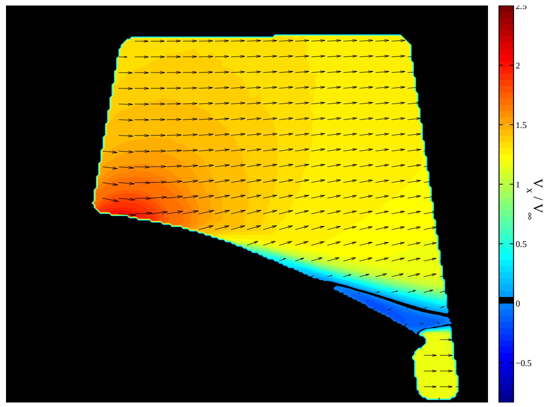

(b)

Figure 5.29: Baseline (a) and Controlled (b) V_x for 16°, 12 m/s. The baseline PIV data was collected with the control system off. In the controlled case, data was collected with the control system set to maximize Z_{lift}, and the tunnel speed corresponds to a Reynolds number of 125,000 based on chord length.

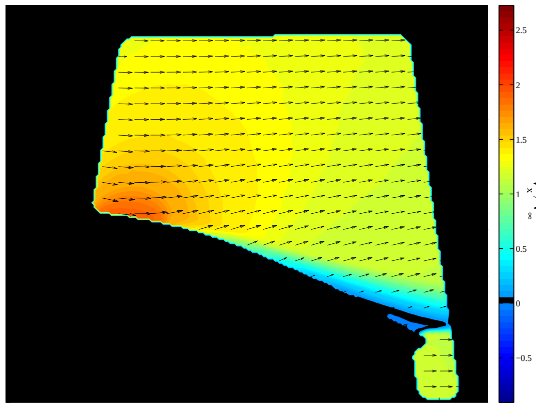

(a)

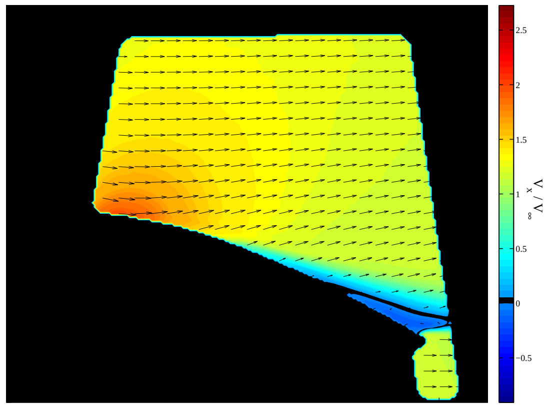

(b)

Figure 5.30: Baseline (a) and Controlled (b) V_x for 16°, 15 m/s. The baseline PIV data was collected with the control system off. In the controlled case, data was collected with the control system set to maximize Z_{lift}, and the tunnel speed corresponds to a Reynolds number of 90,000 based on chord length.

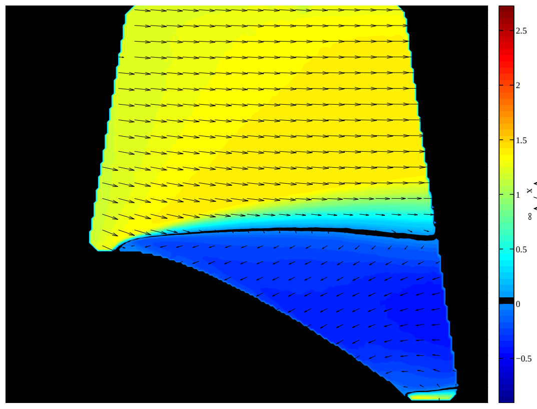

(a)

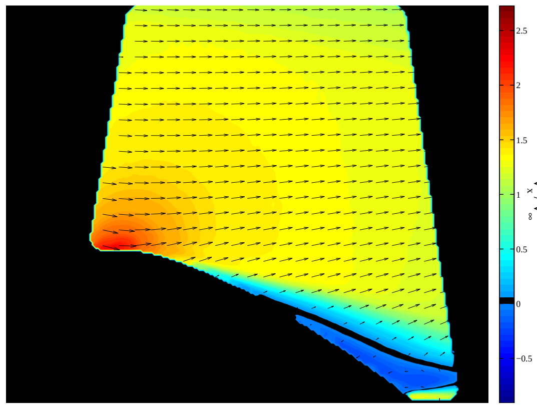

(b)

Figure 5.31: Baseline (a) and Controlled (b) V_x for 22°, 11 m/s. The baseline PIV data was collected with the control system off. In the controlled case, data was collected with the control system set to maximize Z_{lift}, and the tunnel speed corresponds to a Reynolds number of 90,000 based on chord length.

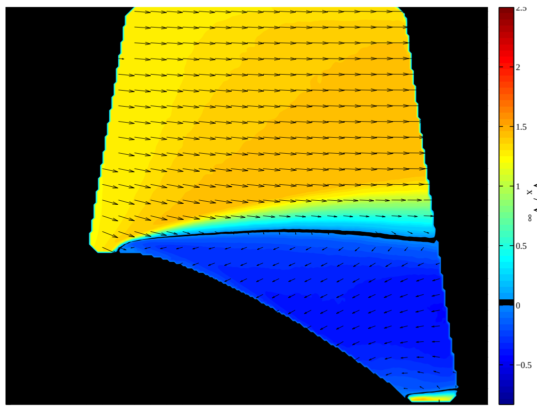

(a)

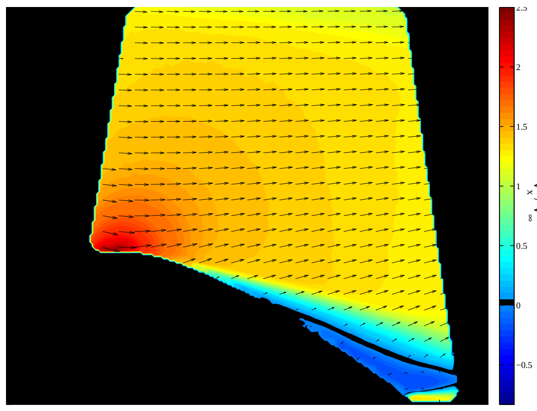

(b)

Figure 5.32: Baseline (a) and Controlled (b) V_x for 22°, 12 m/s. The baseline PIV data was collected with the control system off. In the controlled case, data was collected with the control system set to maximize Z_{lift}, and the tunnel speed corresponds to a Reynolds number of 125,000 based on chord length.

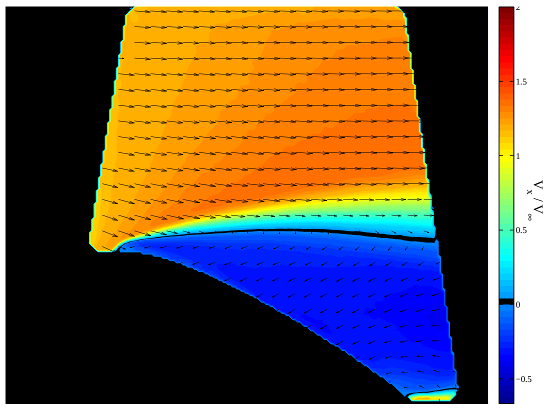

(a)

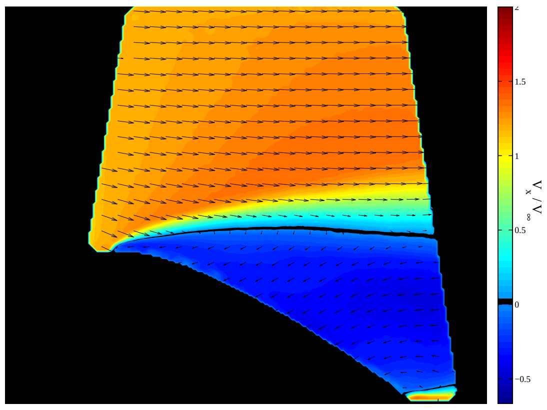

(b)

Figure 5.33: Baseline (a) and Controlled (b) V_x for 22°, 15 m/s. The baseline PIV data was collected with the control system off. In the controlled case, data was collected with the control system set to maximize Z_{lift}, and the tunnel speed corresponds to a Reynolds number of 150,000 based on chord length.

control system. The mounting of this experiment on a force balance will allow further quantitative analysis such as the capability of these actuators to control drag and moments on the wing. This will ultimately indicate whether a microjet and SBMPC control system is a feasible way to achieve pitch and roll control on a wing.

CHAPTER 6

CONCLUDING REMARKS

6.1 Summary of Completed Research

The completed dissertation research includes development of simulation and experimental software, testing in simulation of model-based adaptive control algorithms for simulated nonlinear systems, implementation in simulation and experiments of neural network identification approaches, and implementation in simulation and experiments of SBMPC. The simulated study of coal power plant combustion served as a proof of concept for the control system and also demonstrated MIMO results. The flow separation control application demonstrated the real time implementation of the algorthms. Intermediate work, including the characterization of the relationship between sensor signals and aerodynamic performance from experimental data and the development and validation of a lift-based performance function, are the types of enginering tasks that would need to be performed when applyiing the general Adaptive SBMPC algorithm to various real world applications. The software modules for MRAN and SBMPC algorithms have been compiled and executed on dSPACE hardware (Solaris operating system) for real time execution. SBMPC controller code has been implemented in C and adapted to the real-time framework to compile on dSPACE. Neural network identification code has been implemented in MATLAB, translated to C, and implemented for real time execution in dSPACE.

A dynamic simulation with multiple inputs and outputs was implemented to demonstrate the adaptive, nonlinear, and constraint-handling capabilities of the Adaptive SBMPC method. This work investigated a problem from process control literature and extends the problem to address MIMO and time-varying systems. A custom implementation of Neural GPC was prepared in order to compare the performance of Adaptive SBMPC with an existing method. The performance exceeds that of Neural GPC and requires less computation time for each simulated example.

For the application to flow control, hardware construction was completed for incremental designs of the NACA 0025 airfoil fitted with pressure transducers and microjet channels as well as a motor-pulley system for repeatable angle of attack actuation in 0.3° increments. Two iterations of a pressure regulation system have been constructed and used for all open loop SISO and MIMO tests, and successful feedback control has been demonstrated on the wind tunnel experimental model. Efficacy of the control system was verified with PIV imaging for selected feedback control cases. The same control system has been applied to multiple flow condition configurations without altering the tuning parameters and has performed effectively across a range of angles of attack and Reynolds Numbers, which demonstrates the robustness of the method achieved through adaptation. The diversity of studied applications, including both flow control and power plant control, demonstrates that the Adaptive SBMPC technique is suitable for diverse applications.

6.2 Future Work

Several areas for continued research that would bring this technology closer to implementation on real industrial systems. These areas include computational speedups and additional applications. For the flow control application, future work includes exploration of other sensors and actuators, and further experimentation to demonstrate robustness.

6.2.1 Learning of Heuristics

One potential improvement to Adaptive SBMPC, the learning of A* search heuristics for general nonlinear systems, which would enable further computational improvements, are planned as future work. This improved implementation will make use of past optimization cost information to speed up subsequent optimizations for the same plant.

6.2.2 Parallel Implementation

Further computational improvement is possible using parallel computation. During SBMPO execution, the majority of the the computational effort is spent on expansion of nodes. These expansions may be computed in parallel in order to leverage the capabilities of multi-core CPU or GPU hardware. These computation improvements will allow the application of Adaptive SBMPC to larger systems as well as systems with fast real-time computation requirements.

6.2.3 Additional Applications

The techniques developed in this dissertation are applicable across several industries, and commercial partnership and licensing opportunities are being explored in the power plant control and automotive engine tuning. Discussions with Siemens Energy, Inc., have indicated that there is interest in the Adaptive SBMPC technology for emissions control. Preliminary research results for Adaptive SBMPC have demonstrated that the technique is applicable to power generation and emissions regulations. The application is control of combustion in a coal-fired or gas-fired boiler, which has been demonstrated in simulation. Although smaller plants are more numerous, large plants (200 MW and above) produce the majority of the nation's energy demands, and these are the most heavily regulated by the EPA.

The automotive engine industry, another target market, is also changing dramatically due to environmental concerns, yet the industry has sustained growth over the past decade. Efficiency has long been a driver for this industry, and with the rising price of fuel, this will remain a priority. Adaptive SBMPC is a fast method that can be applied to carry out optimization of engine parameters, which leads to increased efficiency and longevity of engine operations. With numerous parameters and a large search space, time-consuming manual tuning, the current approach, results in suboptimal solutions. As a result, existing engines are not achieving the best possible efficiency. As in the electric power industry, EPA regulation is a major factor in the US automotive engine market. Cummins, for example, was the only company in the market to meet the 2010 EPA standards for NOx emissions with their release of a 6.7-liter turbo diesel for the Dodge Ram Heavy Duty pickup. Better efficiency and control of emissions will continue to be in high demand, as environmental legislation and rising fuel prices continue to make innovation a necessity.

6.2.4 Future Flow Control Research

Because of the variety of new experimental actuators as well as new sensor concepts, future flow control applications for Adaptive SBMPC are numerous. Some directions for future flow control research using Adaptive SBMPC are given below.

High Frequency Actuation. The flow control actuation using solenoid valves produced actuator signals up to approximately 80 Hz, which allows for actuation relevant to large vortex shedding in the wake of the airfoil. The frequencies produced by these actuators are not high enough, however, to interact with the smaller-scale Kelvin Helmholtz vortex structures that form along the boundary layer, which occur on the order of kilohertz at low Reynolds Numbers [45].

Performance Function Testing for Alternate Geometries. Studies using the NACA 0025 airfoil geometry have produced favorable results in both simulation and experiment. In order to produce evidence of the performance function's wide applicability to airborne systems and turbomachinery, tests should be performed with flat plate, NACA 0012, and asymmetric airfoil geometries. It is also possible to mount pressure sensors across the airfoil surface in a spanwise array and use a performance function to measure rolling moments on the airfoil.

Performance Function Testing in Challenging Environments. It is critical to know the capabilities and limitations of a control system, especially of technologies that may be deployed in the future. We propose a series of tests that will demonstrate performance function effectiveness over a series of emulated environmental effects. One such effect is loud broadband noise from an external source. It is hypothesized that the lift based performance function will handle this disturbance better than an RMS performance function because the lift based performance function uses the mean pressure, not its fluctuations, to detect separation. Other environmental factors would include decreased microjet supply pressures or variable humidity and fog.

APPENDIX A

SBMPO ALGORITHM PSEUDOCODE

The SBMPO Algorithm is listed here. Beginning with the root node that represents the system's current state, a graph is built by iteratively expanding the most promising node to generate *B* child nodes. Each child node is assigned an input sample, which is propagated forward through the model to predict a state for that node. The potential cost of reaching that state is used to prioritize the nodes and select the most promising candidate for the next iteration of expansion.

Algorithm 1 Calculate input sequence U via SBMPO graph search

```
Insert root node into the queue with
$i \leftarrow 0$
$C_{E,i} \leftarrow 0$
$N_{D,i} \leftarrow 0$
$parent_i \leftarrow NULL$
$x_i \leftarrow x_0$
Evaluate heuristic cost
$C_{H,i} \leftarrow$ HEUR_COST_EVAL
Pop the top node from the queue
while $(N_{D,top} < N) \wedge (i < MAX\_NODES)$ do
    while $C_{E,top} = NULL$ do
        Evaluate edge cost
        $C_{E,top} \leftarrow C_{E,parent}+$EDGE_COST_EVAL
        Re-insert node into queue, sorted by $C_E + C_H$
        Pop the top node from the queue
    end while
    Expand by Generating $B$ child nodes
    for $j \in [i+1, i+B)$ do
        Generate input space sample
        $u_j \leftarrow$HALTON_SEQUENCE_LOOKUP
        Integrate the model
        $x_j \leftarrow$MODEL_EVAL($u_j, x_{top}$)
        Evaluate heuristic cost
        $C_{H,j} \leftarrow$ HEUR_COST_EVAL
        $C_{E,j} \leftarrow NULL$
        $N_{D,j} \leftarrow N_{D,top} + 1$
        $parent_j \leftarrow i$
        Insert node j into queue, sorted by $C_H$
    end for
    $i \leftarrow i + B$
    Pop the top node from the queue
end while
Construct the optimal input trajectory
$j \leftarrow top$
while $N_{D,j} > 0$ do
    $U(N_{D,j} - 1) = u_j$
    $j \leftarrow parent_j$
end while
```

APPENDIX B

SBMPO SOUNDNESS AND COMPLETENESS PROOF

This proof of soundness and completeness for the algorithm listed in Appendix A is loosely based on the procedure in [35], in which soundness and completeness is derived for a different graph search algorithm. Its culmination, Theorem B.0.6, guarantees that, subject to sufficient depth and breadth of sampling, SBMPO will find a globally optimal solution.

Assumption B.0.1. *The heuristic function is optimistic.*

Assumption B.0.2. *All reachable states have finite edge costs.*

Assumption B.0.3. *All edge costs are non-negative.*

Lemma B.0.4. *The Algorithm will terminate in a finite number of steps, returning a path of length N.*

Proof.

The root node is inserted only once before the main algorithm loop begins. Each node, once expanded, is not re-inserted into the queue, and new nodes (other than the root node) are only inserted by expansion of a parent node. Therefore, each node in the graph is introduced no more than once. In the case in which every parent node of depth N_D is expanded, there are at most B^{N_D} nodes of depth $N_D + 1$ placed in the queue.

No node of greater depth than the prediction horizon N can be generated, since the algorithm termination clause would have been reached first. Including node depths 0 through N, there are at most $L = \sum_{N_D=0}^{N} B^{N_D} = \frac{1-B^{N+1}}{1-B}$ nodes in the entire graph. Each time through the loop, either a node edge cost is computed, a node is expanded, or the algorithm terminates.

If a node edge cost is computed, the queue size is unchanged after that loop iteration (i.e., the node is re-inserted). The number of items in the queue without a computed edge cost, however, decreases by 1. Since each node is introduced no more than once and each edge cost is computed no more than once, the algorithm must terminate before exceeding $2L$ loop iterations. The returned path is of length N because the algorithm can only terminate upon selecting a path of length N.

□

Lemma B.0.5. *The returned path's total cost is less than or equal to that of any path in the graph of length N.*

Proof. (By Contradiction.)

Assume that for the selected path, there exists a path P^- of length N in the graph with a lower cost than the path returned by the algorithm. Therefore P^- must not be represented from the queue. Otherwise, it would have been selected instead of the returned path. The node representing selected path N^+ must have been at the top of the sorted queue (having the lowest total cost in the queue). Because all edge costs are positive, and a node's heuristic value is optimistic, every partial path contained in a path of length N will have a cost less than or equal to the length-N path that contains it.

Let node N^- represent the terminal node of the longest partial path of P^- that was added to the queue. This node must exist because all paths in the graph begin with the same root node, which represents the initial state. Then N^- must have lower total cost than the node N^+ that was selected by the algorithm. Therefore, N^- must have been placed higher in the sorted queue and would have been expanded prior to the selection of N^+, but this yields a contradiction, because the children of node N^- would include a node representing a partial path of P^- that is one edge longer that the path represented by N^-. This is not possible because we chose N^- to be the longest partial path of P^- that was added to the queue.

□

Theorem B.0.6 (Soundness and Completeness)**.** *Upon termination, the SBMPO algorithm will produce a path of nodes representing a minimal cost trajectory among those represented by the graph.*

Proof. This theorem follows from Lemmas B.0.4 and B.0.5. □

APPENDIX C

LISTS OF SIMULATION AND EXPERIMENT PARAMETERS

Table C.1 gives the baseline parameters used in the simulated steam boiler. Table C.2 gives the parameters describing the wind tunnel experiment configuration.

Table C.1: Simulation Parameters: Combustion

Symbol	Parameter	Value(s)
V_d	Gas Production Constant	2.399×10^{-3} m^3/kg
V_O	O_2 Consumption Constant	1.543×10^{-3} m^3/kg
x_C^f	Fuel Carbon Fraction	0.8087
V	Volume of Chamber	0.01 m^3
$\Phi_{\max}$	Max Air Flow	1.833e-2 m^3/s
T	Control Period	10 s
τ	Simulation Integration Step	1×10^{-4} s

Table C.2: Experiment Parameters: Flow Control

Symbol	Parameter	Value(s)
w_1	p_1 Weight	-1.000
w_2	p_2 Weight	-0.9781
w_3	p_3 Weight	-0.9348
w_4	p_4 Weight	-0.9126
c	Chord Length	6 inches
b	Span Length	11.5 inches
T	Control Period	100 ms
P_0	Microjet Source Pressure	0.5 to 10 PSI,
V_{jet}	Microjet Velocity ($P_0 = 2$ PSI)	5 m/s

APPENDIX D

LIST OF TUNING PARAMETER CHOICES

Tables D.1, D.2, D.3, and D.4 give the tuning parameters used in the simulation for each identification and control method. Unless otherwise noted the same tuning parameters were used for all three cases. Tables D.5 and D.6 give the tuning parameters used in the flow control experiment for the identification and control methods.

Table D.1: MRAN Parameter Choices: Combustion Control

Symbol	Parameter	Value(s)
$E1$	Instantaneous Error Threshold	0.00209
$E2$	RMS Error Threshold	0.005
$E3$	Basis Vector Spacing Threshold	0.16
$E3_{\text{DEC}}$	E3 Geometric Decay Rate	0.9985
$E3_{\text{MIN}}$	E3 Decay Floor	0.03
M	RMS Averaging Window	48
N^*	Max Hidden Units	480
κ	Overlap Factor	10.0
q	Kalman Step Parameter	0.5
p_0	New Parameter Variance	5.0
R	Assumed Sensor Noise Variance	0.0
$M_{p,1}$	Pruning Window 1	800
$M_{p,2}$	Pruning Window 2	2000
$\delta_{p,1}$	Pruning Threshold 1	2×10^{-8}
$\delta_{p,2}$	Pruning Threshold 2	1×10^{-4}

Table D.2: BPN Parameter Choices

Symbol	Parameter	Value(s)
N_H	Hidden Units	19, 39, 39*
α	Learning Rate	5.7
η	Momentum Coefficient	5000, 2778.7, 2778.7*
L	Network Gain	0.007
M_1	y_1 Scaling Multiplier	6.0
B_1	y_1 Scaling Bias	0.0
M_2	y_2 Scaling Multiplier	10^{5}†
B_2	y_2 Scaling Bias	0.5†
M_3	y_3 Scaling Multiplier	2.0†
B_3	y_3 Scaling Bias	0.0†

* Case 1, Case 2, and Case 3, respectively.

† Only applicable to Cases 2 and 3.

Table D.3: SBMPC Parameter Choices: Combustion Control

Symbol	Parameter	Value(s)
B	Branchout Factor	60
N	Prediction Horizon	4
N_c	Control Horizon	2

Table D.4: GPC Parameter Choices: Combustion Control

Symbol	Parameter	Value(s)
N	Prediction Horizon	4
N_c	Control Horizon	2
ε	Solver Tolerance	10^{-6}
$I_{\max}$	Max Newton Iterations	1500
s	Constraint Sharpness	10^{-15}
λ	Damping Factor	4×10^{-3}, 9×10^{9}, 9×10^{9}*

*Case 1, Case 2, and Case 3, respectively.

Table D.5: MRAN Parameter Choices: Flow Control

Symbol	Parameter	Value(s)
$E1$	Instantaneous Error Threshold	0.5
$E2$	RMS Error Threshold	2.0
$E3$	Basis Vector Spacing Threshold	2.0
$E3_{\text{DEC}}$	E3 Geometric Decay Rate	1.0
$E3_{\text{MIN}}$	E3 Decay Floor	2.0
M	RMS Averaging Window	48
N^*	Max Hidden Units	120
κ	Overlap Factor	1.0
q	Kalman Step Parameter	0.5
p_0	New Parameter Variance	5.0
R	Assumed Sensor Noise Variance	0.0
$M_{p,1}$	Pruning Window 1	800
$M_{p,2}$	Pruning Window 2	2000
$\delta_{p,1}$	Pruning Threshold 1	2×10^{-8}
$\delta_{p,2}$	Pruning Threshold 2	1×10^{-4}

Table D.6: SBMPC Parameter Choices: Flow Control

Symbol	Parameter	Value(s)
B	Branchout Factor	60
N	Prediction Horizon	2
N_c	Control Horizon	2
T	Control Sample Period	100 ms

APPENDIX E

LIFT BASED PERFORMANCE FUNCTION PLOTS

These data points are from XFOIL viscous simulations. The lift approximating function Z_{lift} as well as C_L and C_L/C_D are dimensionless and normalized here for plotting purposes. Ideally, the maximum of each function should occur at the same angle of attack.

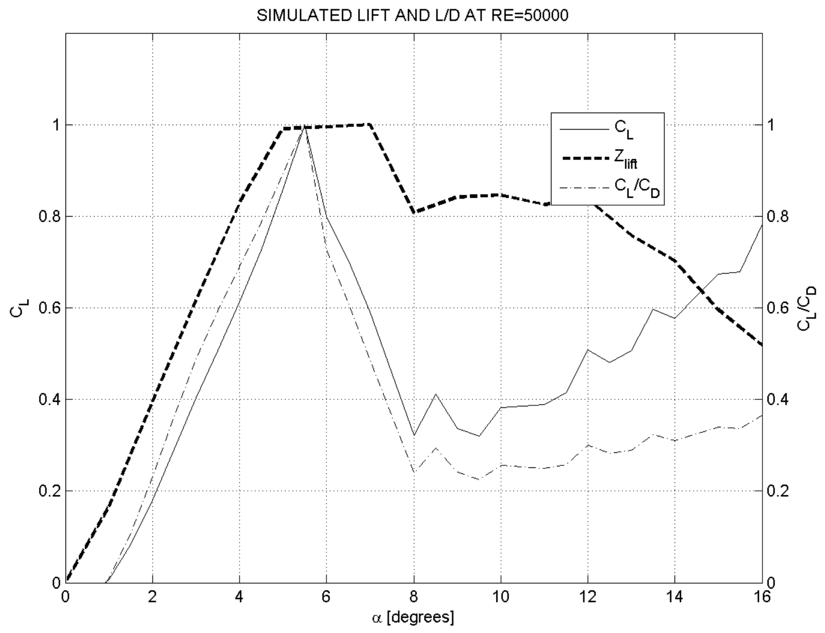

Figure E.1: Lift Coefficient and L/D for $Re = 50000$.

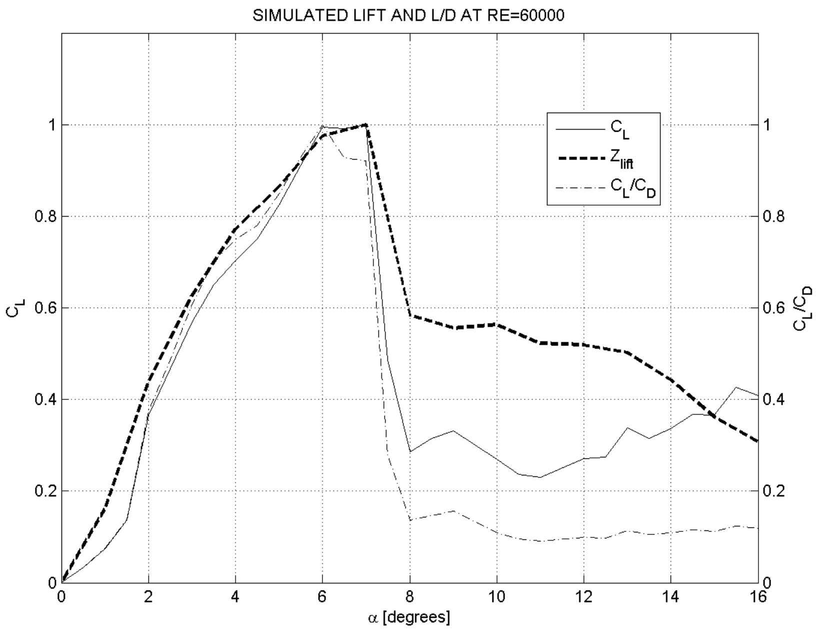

Figure E.2: Lift Coefficient and L/D for $Re = 60000$.

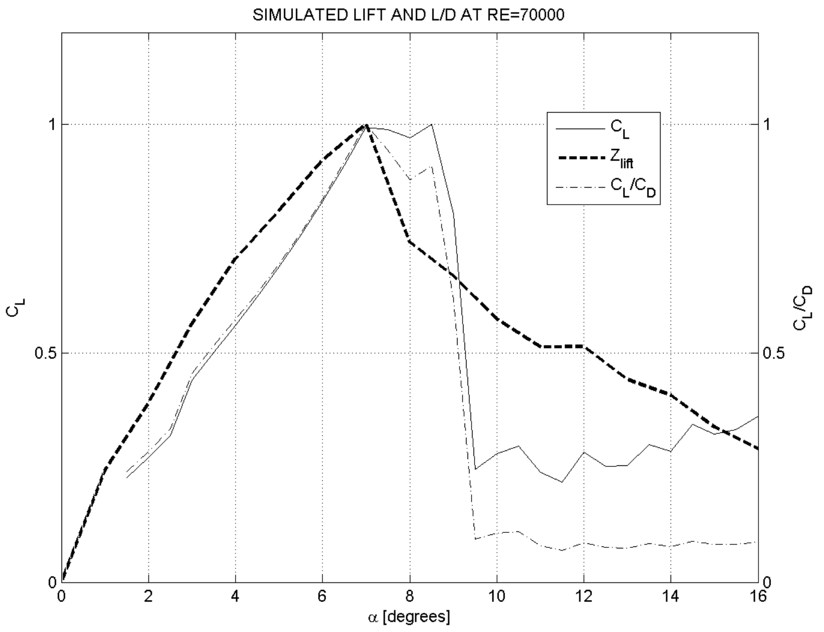

Figure E.3: Lift Coefficient and L/D for $Re = 70000$.

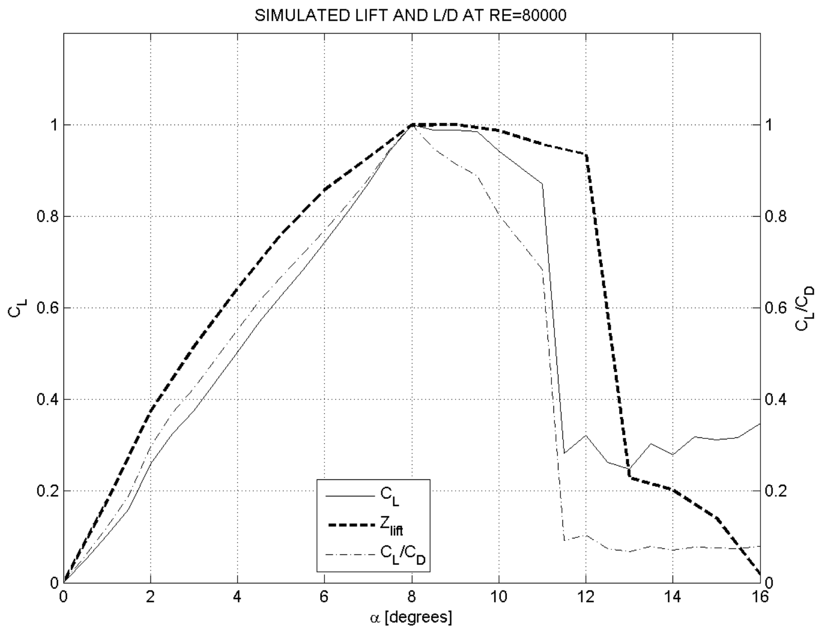

Figure E.4: Lift Coefficient and L/D for $Re = 80000$.

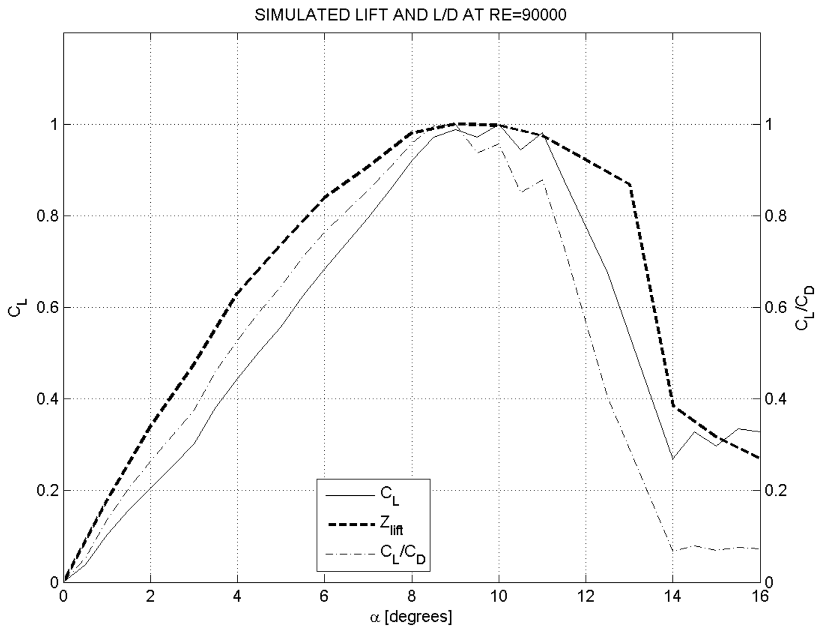

Figure E.5: Lift Coefficient and L/D for $Re = 90000$.

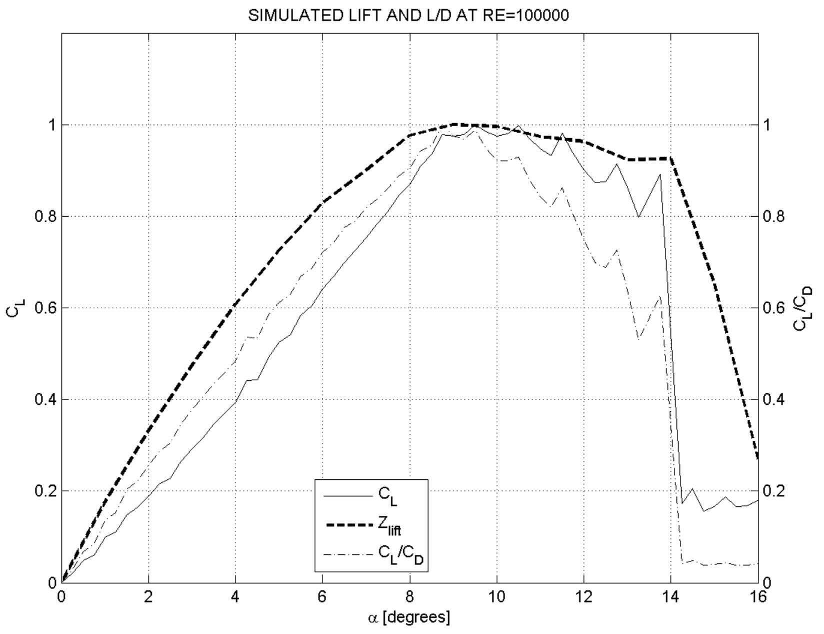

Figure E.6: Lift Coefficient and L/D for $Re = 100000$.

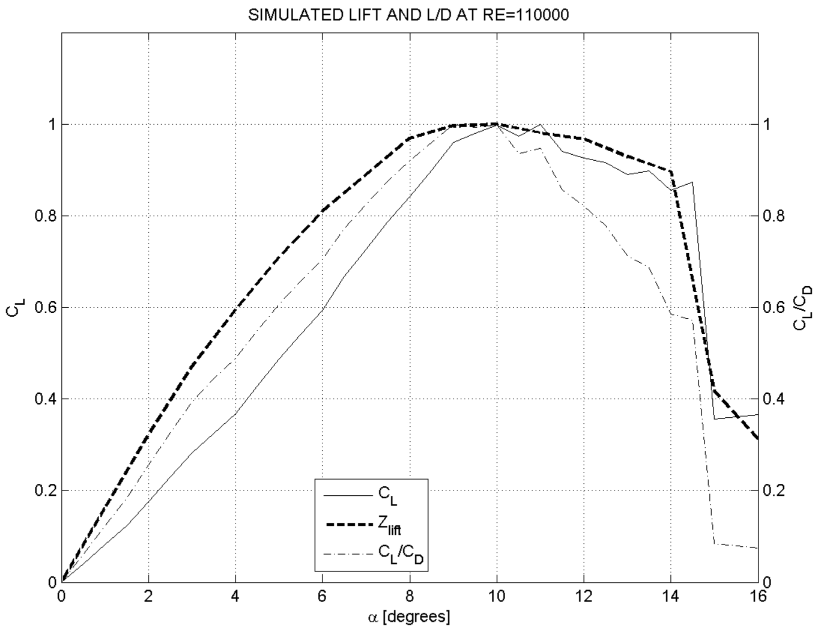

Figure E.7: Lift Coefficient and L/D for $Re = 110000$.

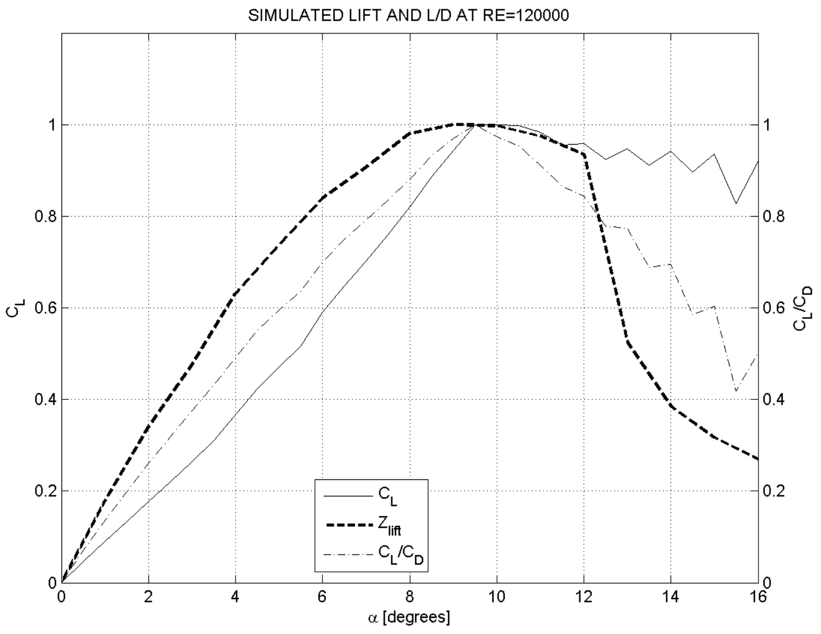

Figure E.8: Lift Coefficient and L/D for $Re = 120000$.

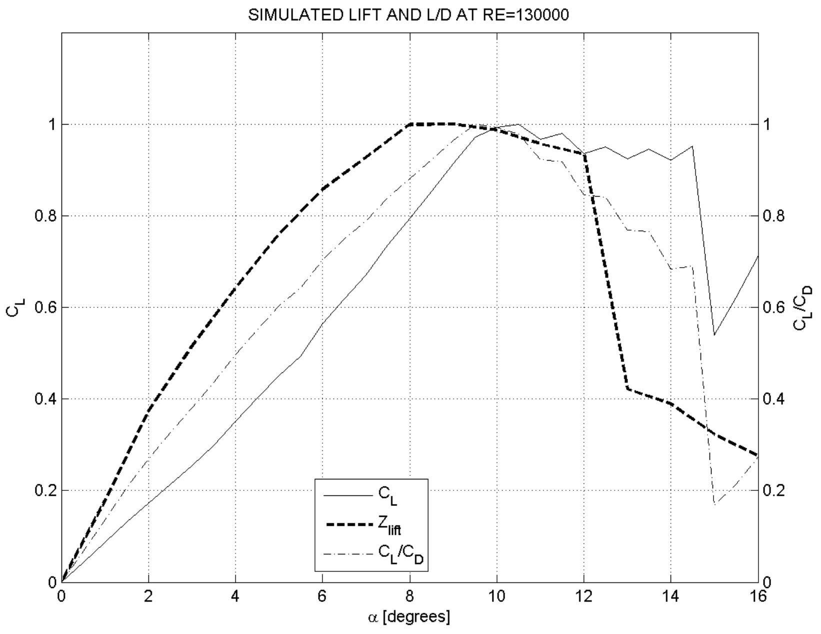

Figure E.9: Lift Coefficient and L/D for $Re = 130000$.

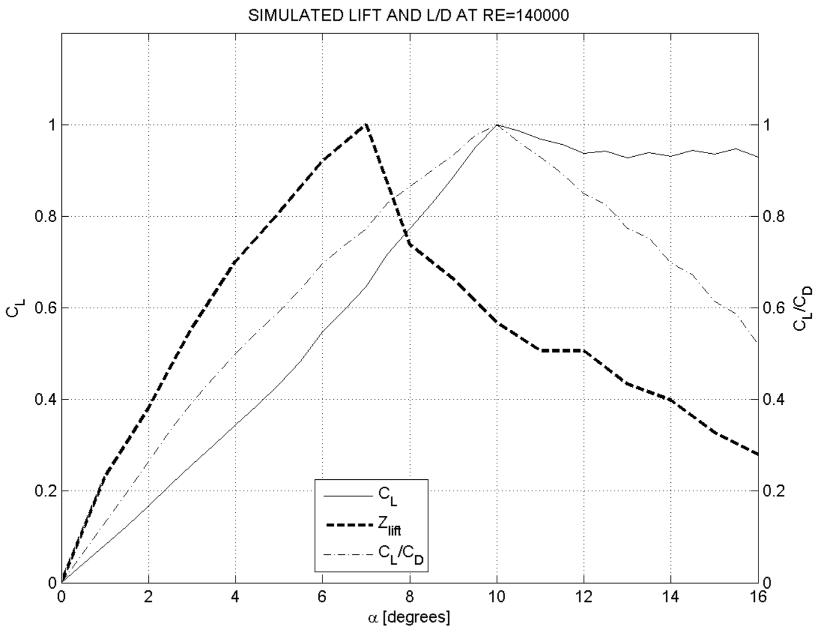

Figure E.10: Lift Coefficient and L/D for $Re = 140000$.

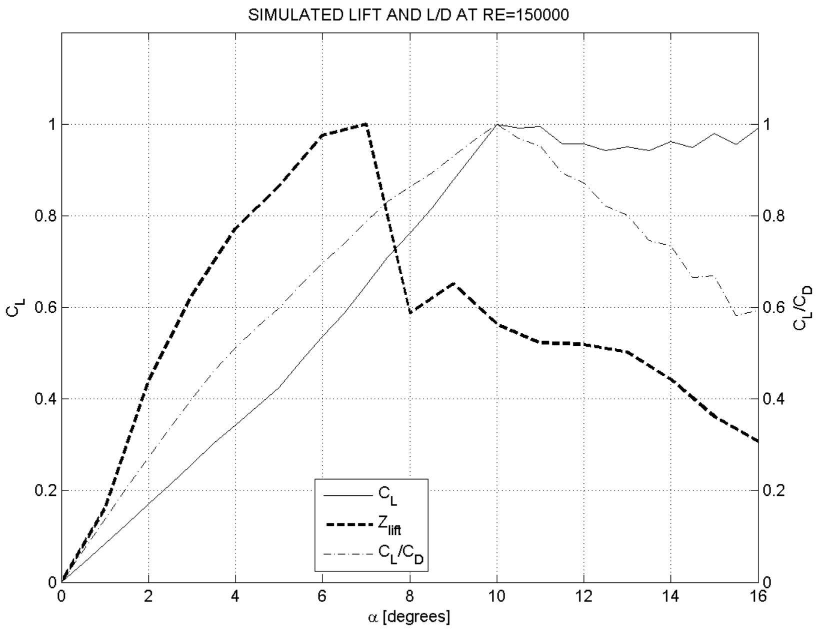

Figure E.11: Lift Coefficient and L/D for $Re = 150000$.

BIBLIOGRAPHY

[1] Motion planning for mobile robots via sampling-based model predictive optimization.

[2] A sequential learning scheme for function approximation using minimal radial basis function neural networks. *Neural computation*, 9(2):461–478, 1997.

[3] Q&a: Epa regulation of greenhouse gas emissions from existing power plants. Center for Climate and Energy Solutions, June 2014.

[4] Farrukh S. Alvi. Adaptive control of inlet separation using supersonic microjets. Technical report, NASA Langley Research Center, Hampton, VA.

[5] Alberto Bemporad and Manfred Morari. Robust model predictive control: A survey. In *Robustness in identification and control*, pages 207–226. Springer, 1999.

[6] Rıdvan Berber and Costas Kravaris. *Nonlinear model based process control*, volume 353. Springer, 1998.

[7] Lorenz T Biegler. A survey on sensitivity-based nonlinear model predictive control. In *10th IFAC International Symposium on Dynamics and Control of Process Systems*, pages 499–510, 2013.

[8] A Bitenc, J Cretnik, J Petrovcic, and S Strmcnik. Design and application of an industrial controller. *Computing Control Engineering Journal*, 3(1):29–34, 1992.

[9] EF Camacho, M Berenguel, and FR Rubio. Application of a gain scheduling generalized predictive controller to a solar power plant. *Control Engineering Practice*, 2(2):227–238, 1994.

[10] Louis Cattafesta, Ye Tian, and R. Mittal. Adaptive control of post-stall separated flow application to heavy vehicles. *Springer Berlin Heidelberg Lecture Notes in Applied and Computational Mechanics*, 41(5):151–160, 2009.

[11] H Chi, M Mascagni, and T T Warnock. On the optimal halton sequence. *Mathematics and Computers in Simulation*, 70(1):9–21, 2005.

[12] Oscar Y. Chuy, Vikas Kumar, Frederick V. Holt III, Emmanuel G. Collins Jr., and Farrukh S. Alvi. Microjet-based separation control using a virtual sensor for degree of separation. In *Florida Center for Advanced Aero-Propulsion Annual Technical Symposium*, Tallahassee, Fl, August 2009. FCAAP.

[13] D W Clarke. Generalized predictive control. *Automatica*, 23(2):149–160, 1987.

[14] J Cretnik. *Modern Automatic Combustion Control*. Phd dissertation, Ljubljana School of Electrical and Computer Engineering, 1992.

[15] Jurij Čretnik. *Modern automatic combustion control*. 1993.

[16] I Culjak, A Sikanic, and V Koroman. Renewable energy sources in compliance of kyoto protocol targets: Case study of 42 mw wind field. *Energy and the Environment 2008 Vol 2*, pages 89–99 464, 2008.

[17] Daniel Delling, Peter Sanders, Dominik Schultes, and Dorothea Wagner. Engineering route planning algorithms. In *Algorithmics of large and complex networks*, pages 117–139. Springer, 2009.

[18] Damion Dunlap, Wei Yu, Emmanuel G Collins, and Charmane V Caldwell. Motion planning for steep hill climbing. In *2011 IEEE International Conference on Robotics and Automation*, pages 707–714. IEEE, 2011.

[19] Damion D Dunlap, Charmane V Caldwell, and Emmanuel G Collins Jr. Nonlinear model predictive control using sampling and goal-directed optimization. *Mechanical Engineering*, 16:1349–1356, 2010.

[20] M. Debiasi M. Samimy E. Caraballo, J. Little. Development and implementation of an experimental based reduced-order model for feedback control of subsonic cavity flows. *Journal of Fluids Engineering*, 129(7):813–824, 2007.

[21] Christer Ericson. *Real-time collision detection*, volume 14. Elsevier Amsterdam/Boston, 2005.

[22] Julien Favier, Azeddine Kourta, and Gillian Leplat. Control of flow separation of a wing profile using piv measurements and pod analysis. In *IUTAM Symposium on Flow Control with MEMS*. IMFT - French National Institute of Mechanics of Toulouse, IUTAM, September 2006.

[23] Eduardo Gallestey, Alec Stothert, Marc Antoine, and Steve Morton. Model predictive control and the optimization of power plant load while considering lifetime consumption. *Power Systems, IEEE Transactions on*, 17(1):186–191, 2002.

[24] Alexandra Grancharova and Tor Arne Johansen. *Explicit nonlinear model predictive control: theory and applications*, volume 429. Springer, 2012.

[25] Alexandra Grancharova, Ju Kocijan, and Tor A Johansen. Explicit stochastic predictive control of combustion plants based on gaussian process models. *Automatica*, 44(6):1621–1631, 2008.

[26] Alexandra Grancharova, Ju Kocijan, and Tor A Johansen. Explicit output-feedback nonlinear predictive control based on black-box models. *Engineering Applications of Artificial Intelligence*, 24(2):388–397, 2011.

[27] P. Haley, D. Soloway, and B. Gold. Real-time adaptive control using neural generalized predictive control. In *American Control Conference, 1999. Proceedings of the 1999*, volume 6, pages 4278–4282, 1999.

[28] P E Hart, N J Nilsson, and B Raphael. A formal basis for the heuristic determination of minimum cost paths. *Ieee Transactions On Systems Science And Cybernetics*, 4(2):100–107, 1968.

[29] Simon Haykin. *Kalman Filtering and Neural Networks*, volume 5. John Wiley And Sons, Inc., 2001.

[30] Robert Hecht-Nielsen. Theory of the backpropagation neural network. In *Neural Networks, 1989. IJCNN., International Joint Conference on*, pages 593–605. IEEE, 1989.

[31] Michael A Henson. Nonlinear model predictive control: current status and future directions. *Computers and Chemical Engineering*, 23(2):187–202, 1998.

[32] SC Hill and L Douglas Smoot. Modeling of nitrogen oxides formation and destruction in combustion systems. *Progress in energy and combustion science*, 26(4):417–458, 2000.

[33] Kurt Hornik. Some new results on neural network approximation. *Neural Networks*, 6(8):1069–1072, 1993.

[34] E. Caraballo M. Samimy J. Little, M. Debiasi. Effects of open-loop and closed-loop control on subsonic cavity flows. *Physics of Fuids*, 19(065104), 2007.

[35] Sertac Karaman. Soundness and completeness of state space search. Massachusetts Institute of Technology: MIT OpenCourseWare, Sept. 2010.

[36] Kihwan Kim, A. Beskok, and S. Jayasuriya. Nonlinear system identification for the interaction of synthetic jets with a boundary layer. In *American Control Conference, 2005. Proceedings of the 2005*, pages 1313 – 1318 vol. 2, june 2005.

[37] Sven Koenig, Maxim Likhachev, and David Furcy. Lifelong planning a. *Artificial Intelligence*, 155(1):93–146, 2004.

[38] Mayuresh V Kothare, Bernard Mettler, Manfred Morari, Pascale Bendotti, and C-M Falinower. Level control in the steam generator of a nuclear power plant. *Control Systems Technology, IEEE Transactions on*, 8(1):55–69, 2000.

[39] J J Kuffner and S M LaValle. Rrt-connect: An efficient approach to single-query path planning. *Proceedings 2000 ICRA Millennium Conference IEEE International Conference on Robotics and Automation Symposia Proceedings Cat No00CH37065*, 2(Icra):995–1001, 2000.

[40] Vikas Kumar. *Separation Control in Adverse Pressure Gradient using High-Speed Microjets*. Phd dissertation, Mechanical Engineering, Florida State Universtiy, Tallahassee, Fl, 2008.

[41] Vikas Kumar and Farrukh S. Alvi. Efficient control of separation using microjets. June 2005.

[42] Vikas Kumar and Farrukh S. Alvi. Towards understanding and optimizing separation control using microjets. *AIAA*, 47(11):2544–2557, November 2009.

[43] Mikel Larrea, Eloy Irigoyen, Vicente Gmez, and Fernando Artaza. Nonlinear system control based on neural networks with adaptive predictive strategy. In *Emerging Technologies and Factory Automation ETFA 2010 IEEE Conference on*, pages 1–7, 2010.

[44] S M LaValle and J J Kuffner. Randomized kinodynamic planning. *The International Journal of Robotics Research*, 20(5):378–400, 2001.

[45] JC Muti Lin and Laura L Pauley. Low-reynolds-number separation on an airfoil. *AIAA journal*, 34(8):1570–1577, 1996.

[46] Joshua Linn, Erin Mastrangelo, and Dallas Burtraw. Regulating greenhouse gases from coal power plants under the clean air act. *Journal of the Association of Environmental and Resource Economists*, 1(1):97–134, 2014.

[47] Xiangjie Liu, Ping Guan, and CW Chan. Nonlinear multivariable power plant coordinate control by constrained predictive scheme. *Control Systems Technology, IEEE Transactions on*, 18(5):1116–1125, 2010.

[48] Emmanuel Lochin and Bruno Talavera. Managing internet routers congested links with a kohonen-red queue. *Engineering Applications of Artificial Intelligence*, 24(1):77–86, 2011.

[49] M. Samimy M. Debiasi, J. Little. Analysis of the spectral relationships of cavity tones in susonic resonant cavity flows. *Physics of Fluids*, 21(055103), 2009.

[50] E. Caraballo A Serrani X. Yuan J. Little J.H. Myatt M. Samimy, M. Debiasi. Feedback control of subsonic cavity flows using reduced-order models. *Journal of Fluid Mechanics*, 579:315–346, 2007.

[51] D Q Mayne, J B Rawlings, C V Rao, and P O M Scokaert. Constrained model predictive control: Stability and optimality. *Automatica*, 36(6):789–814, 2000.

[52] David Q Mayne. Model predictive control: Recent developments and future promise. *Automatica*, 50(12):2967–2986, 2014.

[53] Eric Moreau. Airflow control by non-thermal plasma actuators. *Journal of Physics D: Applied Physics*, 40(3):605, 2007.

[54] Bernd R Noack, Marek Morzynski, and Gilead Tadmor. *Reduced-Order modelling for flow control*, volume 528. Springer, 2011.

[55] X. Yuan J. Little H. Ozbay M. Samimy P. Yan, M. Debiasi. Experimental study of linear closed-loop control of subsonic cavity flow. *AIAA*, 44(5):929–938, 2006.

[56] T Pengo, A Muoz-Barrutia, and C Ortiz-De-Solrzano. Halton sampling for autofocus. *Journal of Microscopy*, 235(1):50–58, 2009.

[57] Fernando J Pineda. Generalization of back-propagation to recurrent neural networks. *Physical review letters*, 59(19):2229, 1987.

[58] J Platt. A resource-allocating network for function interpolation. *Neural Computation*, 3(2):213–225, 1991.

[59] S Joe Qin and Thomas A Badgwell. An overview of industrial model predictive control technology. *Automatica*, 93(316):232–256, 1997.

[60] S Joe Qin and Thomas A Badgwell. A survey of industrial model predictive control technology. *Control engineering practice*, 11(7):733–764, 2003.

[61] Anand B Rao and Edward S Rubin. A technical, economic, and environmental assessment of amine-based co2 capture technology for power plant greenhouse gas control. *Environmental Science & Technology*, 36(20):4467–4475, 2002.

[62] Brandon Reese, Farrukh Alvi, and Emmanuel Collins. Development of an improved performance function for the control of flow separation. In *51st AIAA Aerospace Sciences Meeting including the New Horizons Forum and Aerospace Exposition*, 2013.

[63] Brandon Reese, Farrukh S. Alvi, and Emmanuel G. Collins. A nonlinear adaptive method for microjet-based flow separation control. In *7th AIAA Flow Control Conference*, volume AIAA Aviation. AIAA, 2014.

[64] Brandon Reese and Emmanuel G. Collins. Sampling based control of a combustion process using a neural network model. *Systems, Man, and Cybernetics, Part B: Cybernetics, IEEE Transactions on*, To Appear, 2014.

[65] C.W. Rowley, T. Colonius, and R.M. Murray. Model reduction for compressible flows using pod and galerkin projection. *Physica D: Nonlinear Phenomena*, 189(1):115–129, 2004.

[66] Mark Sheplak, Louis Cattafesta, and Ye Tian. Micromachined shear stress sensors for flow control applications. In J.F. Morrison et al., editor, *IUTAM Symposium on Flow Control and MEMS*, pages 67–73. IUTAM, Springer, January 2008.

[67] D Soloway and P J Haley. Neural generalized predictive control. In *Proceedings of the IEEE International Symposium on Intelligent Control*, number 13, pages 133–152, 1996.

[68] Qi Song, Ye Tian, and Louis Cattafesta. Mimo feedback control of flow separation. In *45th AIAA Aerospace Sciences Meeting and Exhibit*, Reston, VA, January 2007. AIAA.

[69] Donald F Specht. A general regression neural network. *Neural Networks, IEEE Transactions on*, 2(6):568–576, 1991.

[70] Ye Tian and Louis Cattafesta. Adaptive control of flow separation. In *44th Aerospace Sciences Meeting and Exhibit*, Reston, Va, January 2006. Interdisciplinary Microsystems Group, AIAA.

[71] Ye Tian, Qi Song, and Louis Cattafesta. Adaptive feedback control of flow separation. In *3rd AIAA Flow Control Conference*, Reston, VA, June 2006. Interdisciplinary Microsystems Group, AIAA.

[72] Ravinder Venugopal and Dennis S. Bernstein. Adaptive disturbance rejection using armarkov/toeplitz models. In *IEEE Transactions on Control Systems Technology*, volume 8, pages 257–269. IEEE, March 2000.

[73] Lu Yingwei Lu Yingwei, N Sundararajan, and P Saratchandran. Performance evaluation of a sequential minimal radial basis function (rbf) neural network learning algorithm. *IEEE Transactions on Neural Networks*, 9(2):308–318, 1998.

[74] Jing-Ru Zhang, Jun Zhang, Tat-Ming Lok, and Michael R Lyu. A hybrid particle swarm optimization–back-propagation algorithm for feedforward neural network training. *Applied Mathematics and Computation*, 185(2):1026–1037, 2007.

[75] Hong Zhao, John Guiver, Ramesh Neelakantan, and Lorenz T Biegler. A nonlinear industrial model predictive controller using integrated pls and neural net state-space model. *Control Engineering Practice*, 9(2):125–133, 2001.

[76] David Zipser and Richard A Andersen. A back-propagation programmed network that simulates response properties of a subset of posterior parietal neurons. *Nature*, 331(6158):679–684, 1988.

BIOGRAPHICAL SKETCH

Brandon Reese completed primary and secondary education in Alpharetta, GA before attending Massachusetts Institute of Technology, where he earned a Bachelor's of Science degree in aerospace engineering (2009). While at MIT, he participated in undergraduate research and tutoring programs for MIT peers and high school students. He was awarded the Robert E. McNair Scholar Award, an MIT Institute award, for outstanding academic performance and contribution to the minority community. He also won the Richard Nordlof award for MIT Music and Theater Arts. He attended Florida State University for graduate school and completed a Ph.D. in mechanical engineering (2015) and was awarded a McKnight Doctoral Fellowship. He has held technical positions as an intern at the Aerospace Corporation, earning two corporate SPOT awards in Summer 2009. He has also been honored as a Modern Day Technology Leader by the Black Engineer of the Year Awards STEM Conference and Magazine in 2010.

Conference Publications

- Reese, Brandon, Farrukh Alvi, and Emmanuel G. Collins. "Development of an Improved Performance Function for the Control of Flow Separation." 51st AIAA Aerospace Sciences. January 2013.
- Reese, Brandon M., Farrukh S. Alvi, and Emmanuel G. Collins. "A Nonlinear Adaptive Method for Microjet-Based Flow Separation Control." AIAA Aviation Conference. June 2014.
- Reese, Brandon M., and Emmanuel G. Collins. "Sampling Based Control of a Combustion Process Using a Neural Network Model." Systems, Man and Cybernetics (SMC), 2014 IEEE International Conference on. October 2014.

Journal Publications

- Reese, Brandon and Emmanuel G. Collins. "Adaptive Sampling Based Model Predictive Control Part 1: The Algorithm." Control Systems Technology, IEEE Transactions on. Submitted manuscript, 2015.
- Reese, Brandon and Emmanuel G. Collins. "Adaptive Sampling Based Model Predictive Control Part 2: Application to a Combustion Process." Control Systems Technology, IEEE Transactions on. Submitted manuscript, 2015.
- Reese, Brandon, Emmanuel G. Collins, Erik Fernandez, and Farrukh Alvi. "A Nonlinear Adaptive Approach to Microjet-Based Flow Separation Control." AIAA Journal. Submitted manuscript, 2015.
- Kreth, Phil A., Farrukh Alvi, Brandon Reese, and William Oates. "Control of High Frequency Microactuators Using Active Structures." Smart Materials and Structures 24.2 (2015): 025030.